

Dissertation

submitted to the
Combined Faculties for the Natural Sciences and for Mathematics
of the Ruperto-Carola University of Heidelberg, Germany
for the degree of
Doctor of Natural Sciences

presented by

Diplom-Physicist Konrad R. W. Tristram
born in Freiburg im Breisgau, Germany

Oral examination: July 25th, 2007

Mid-infrared interferometry of nearby Active Galactic Nuclei

Referees: Prof. Dr. Klaus Meisenheimer
Prof. Dr. Immo Appenzeller

Abstract: Active galactic nuclei are powered by the accretion of matter onto supermassive black holes in the centre of galaxies. In unified schemes, warm, obscuring dust and gas in a torus play a major role for the different manifestations of such nuclei. The differences are thought to depend on the viewing angles with respect to the dust distribution, which absorbs the nuclear light and re-emits it in the infrared.

The scientific goal of this thesis is to reveal the nature of the nuclear mid-infrared source in a few nearby active galaxies in order to explore the innermost dust distribution on parsec scales. As this requires angular resolutions of < 20 mas, interferometric observations with the MIDI instrument at the Very Large Telescope Interferometer were performed.

The primary target is the Circinus galaxy, a prototype Seyfert 2 galaxy. The modelling of the interferometric data revealed that warm dust ($T \sim 300$ K) is located in two components: in a disk with a radius of 0.2 pc and in a larger, geometrically thick and clumpy torus extending out to 1 pc. The size, orientation and temperature of this configuration are in agreement with the long sought dusty torus of Seyfert galaxies.

The mid-infrared emission in the radio galaxy Centaurus A is of a totally different nature. The bulk of its emission comes from an unresolved synchrotron core, most likely the foot of the jet. Only about 30 % of the mid-infrared flux originates in an extended distribution of warm dust. Three further targets observed by MIDI (Mrk 1239, MCG-05-23-016 and 3C 273) are basically unresolved, only allowing upper limits on the size of their dust distributions.

Although the completely new observations in general confirm the concept of unification, significant discrepancies between the observations and very simple models occur which need to be quantified by further (interferometric) observations. This may lead to a revision of the most simple unified schemes.

Zusammenfassung: Aktive galaktische Kerne werden durch die Akkretion von Materie auf ein supermassereiches Schwarzes Loch angetrieben. In vereinheitlichenden Modellen werden die unterschiedlichen Erscheinungsformen solcher Kerne durch verschiedene Blickwinkel bezüglich von warmem Staub und Gas, die den Kern in einem Torus umgeben, erklärt.

Das Ziel dieser Arbeit ist die Untersuchung der Emission aktiver Kerne im mittleren Infrarot, um die Eigenschaften der zentralen Staubverteilung auf Größenordnungen von einem Parsec zu erforschen. Um die notwendige Winkelauflösung im Bereich von weniger als 20 Milli-Bogensekunden zu erreichen, wurden interferometrische Beobachtungen mit dem Instrument MIDI am Very Large Telescope Interferometer durchgeführt.

Hauptstudienobjekt dieser Arbeit ist die Circinus Galaxie, eine typische Seyfert 2 Galaxie. Die Modellierung der interferometrischen Daten ergibt, daß sich der warme ($T \sim 300$ K) Staub in zwei Komponenten befindet: in einer Scheibe mit einem Radius von 0.2 pc und in einem größeren, dicken und klumpigen Torus mit 2 pc Durchmesser. Die Größe, die Orientierung und die Temperatur dieser Anordnung bestätigen die Präsenz des lange vermuteten Staubtorus der Seyfert Galaxien.

Von ganz anderer Natur ist die Quelle in der Galaxie Centaurus A. Der Hauptteil der Emission im mittleren Infrarot stammt von einer unaufgelösten Synchrotronquelle, vermutlich dem Fußpunkt des Radiojets. Nur etwa 30 % des Flusses stammen von einer ausgedehnten Staubverteilung. Drei weitere Objekte sind im Wesentlichen unaufgelöst und ermöglichen so nur die Bestimmung oberer Grenzen für die Größe ihrer Staubverteilungen.

Obwohl die neuen Beobachtungen das Konzept der Vereinheitlichung von aktiven galaktischen Kernen bestätigen, treten signifikante Unterschiede zu einfachen Modellen auf. Diese Diskrepanzen müssen durch weitere (interferometrische) Beobachtungen untersucht werden und können Verbesserungen an den einfachsten vereinheitlichenden Modellen erfordern.

Contents

1	Introduction	1
1.1	AGN and their manifestations	1
1.2	The physical picture of AGN	3
1.3	The spectral energy distribution of AGN	6
1.4	The dusty torus	7
1.5	The mid-infrared	9
1.6	High resolution observational methods	10
2	Interferometry	13
2.1	Basics of interferometry	13
2.1.1	Monochromatic point source	13
2.1.2	Polychromatic sources	16
2.1.3	Extended sources	18
2.1.4	Source morphologies	19
2.1.4.1	Point source	19
2.1.4.2	Binary	19
2.1.4.3	Gaussian distribution	21
2.1.4.4	Uniform disk	21
2.1.5	Importance of the phase	21
2.1.6	The uv plane	23
2.2	The VLTI	23
2.2.1	The site	24
2.2.2	The VLTI infrastructure	24
2.2.3	Path of the light	25
2.2.4	Interferometric instruments at the VLTI	26
2.3	The MIDI instrument	27
3	Observations and data reduction	31
3.1	Observations	31
3.1.1	Preset	31
3.1.2	Acquisition	32
3.1.3	Fringe search	32
3.1.4	Fringe track	34
3.1.5	Photometry	34
3.2	Data reduction	35
3.2.1	Properties of the MIDI data	35
3.2.2	Data reduction packages	37
3.2.3	Compression	37

3.2.4	Coherent reduction	39
3.2.5	Incoherent reduction	41
3.2.6	Photometry	41
3.2.7	Masks	43
3.3	Calibration	44
3.4	Error estimates	47
4	The dusty torus in the Circinus galaxy	49
4.1	Introduction	49
4.2	Observations and data reduction	50
4.2.1	Observations	50
4.2.2	Data reduction	52
4.3	Results	53
4.3.1	uv coverage	53
4.3.2	Total flux	54
4.3.3	Interferometric data	55
4.4	Modelling	57
4.4.1	Image reconstruction attempt	57
4.4.2	1D model	58
4.4.3	2D geometrical model	60
4.4.4	2D physical model	63
4.4.5	Other models	69
4.5	Discussion	71
4.5.1	Extinction	71
4.5.2	Energy budget	73
4.5.3	Temperature dependency and clumpiness	74
4.5.4	Orientation and geometry of the dust distribution	76
4.5.5	Collimation of the ionisation cone and outflow	77
4.5.6	Dust properties	78
4.6	Conclusions	78
5	MIDI Interferometry of Centaurus A	81
5.1	Introduction	81
5.2	Observations	82
5.2.1	Interferometric observations and data reduction	82
5.2.2	Additional single-telescope observations	83
5.3	MIDI Results	84
5.4	Overall core spectrum of Centaurus A	87
5.5	Discussion	91
5.5.1	The synchrotron core	91
5.5.2	Nuclear dust emission from the parsec-sized disk	92
5.5.3	Comparison with other radio sources	93
5.6	Conclusions	94
6	Fainter sources observed with MIDI	95
6.1	Introduction	95
6.2	Target list and observational challenges	95
6.3	Observations and data reduction	98
6.3.1	Mrk 1239 and MCG-05-23-016	98

6.3.2	3C 273	98
6.4	Results	100
6.4.1	MCG-05-23-016 and Mrk 1239	100
6.4.2	3C 273	103
7	Outlook and conclusions	105
7.1	Outlook	105
7.1.1	Further interferometric investigations	105
7.1.2	The nuclear SED of AGN	108
7.1.3	VISIR spectroscopy	108
7.2	Conclusions	109

Chapter 1

Introduction

Active galactic nuclei (AGN¹) are among the most fascinating objects in the universe. In their hearts, large amounts of energy are released and they are impressive manifestations of *supermassive black holes*, which in turn are probably the most intriguing objects of astrophysics. Apart from the supermassive black hole and an accretion disk surrounding it, warm dust and gas are important constituents of AGN. The nuclei are thought to play an important role in the formation of galaxies, that is, in the formation of cosmological structures. Despite almost a century of research on their nature, our understanding of AGN remains limited.

In this thesis, several AGN will be studied in detail. The goal is to better understand the physical processes in a number of example objects. The prime interest lies in ascertaining the distribution of the nuclear dust. The main observational tool for this research is interferometry in the mid-infrared.

Chapter 1 starts with an introduction to the field of AGN. It is meant to provide background information on these objects and to convey the motivation for the research presented in this thesis. More detailed disquisitions on AGN can be found in the books by Robson (1996), Peterson (1997) and Krolik (1999), as well as in Osterbrock and Ferland (2006). In the discussion presented here, an emphasis will be put on the importance of dust in our understanding of the AGN phenomenon. From there, the need for high resolution observations in the mid-infrared will be explained.

Chapter 2 focusses on the basics of interferometry, the observational method providing the required high angular resolutions. The chapter also includes a presentation of the Very Large Telescope Interferometer and its mid-infrared instrument MIDI. A description of the observation procedures with MIDI and the data reduction is given in chapter 3. In chapter 4 and 5, the interferometric observations of the Circinus galaxy and Centaurus A will be discussed, while chapter 6 covers other sources, which are studied in less detail. An outlook and the conclusions are given in chapter 7.

1.1 AGN and their manifestations

The term “active galactic nucleus” derives from the observational fact that a number of galaxies possess a very high concentration of luminosity in their nucleus. The luminosities of active nuclei lie in the range of 10^5 to $10^{15} L_{\odot}$. An AGN can contribute more to the total luminosity of its host galaxy than the entire stellar component ($\sim 10^{11} L_{\odot}$). Often, the

¹Throughout this work, the abbreviation “AGN” will be used both for “active galactic nucleus”, that is, a single object, as well as for “active galactic nuclei”, that is, several objects of this kind.

emission of an AGN covers the entire electromagnetic spectrum, ranging from radio emission to γ -rays.

Edward A. Fath discovered the first galaxy hosting an AGN in 1908 while obtaining a spectrum of the “spiral nebula” NGC 1068. The spectrum of this galaxy showed strong emission lines in addition to the continuum flux and to the absorption lines also seen in other nebulae (Fath, 1908). After this first spectrum, more such “emission line galaxies” were discovered. In 1943, when already 12 galaxies of this “unusual class of objects” had been found, Carl K. Seyfert published his fundamental paper on emission line galaxies (Seyfert, 1943). In this paper, he described the main features of the emission lines. He was also the first to recognise that these galaxies form a special class of objects. He further noted that the emission lines are emitted from a point-like source at the centre of the galaxies and that this point-like source contributes a large fraction of the total light emitted by the entire system. From the large width of the emission lines, he deduced a high velocity dispersion in the emitting medium. His work has been rewarded by the fact that we now call these objects *Seyfert galaxies*.

Seyfert galaxies are essentially normal spiral galaxies, with strong nuclear emission. About 3% to 5% of all galaxies are Seyfert galaxies (Maiolino and Rieke, 1995; Maia *et al.*, 2003). Khachikian and Weedman (1974) divided the Seyfert galaxies into two subclasses. *Seyfert 2 nuclei* (Sy 2) show forbidden and permitted emission lines which are broadened by Doppler shifts corresponding to velocities of $< 1000 \text{ km s}^{-1}$. Prominent examples are NGC 1068 and the Circinus galaxy. The spectra of *Seyfert 1 nuclei* (Sy 1) additionally possess permitted lines which are Doppler broadened by velocities of $1000 - 5000 \text{ km s}^{-1}$. Well-known examples are NGC 4151 and NGC 3783. There are about three times more Seyfert 2 than Seyfert 1 galaxies (Maiolino and Rieke, 1995; Maia *et al.*, 2003). Today, a continuous notation between Sy 1 and Sy 2, such as for example “Sy 1.8” or “Sy 1.9”, is common (Osterbrock, 1981).

A class of galaxies similar to Seyfert galaxies was introduced by Heckman (1980): these so-called **LINERs** (low-ionisation nuclear emission line region galaxies) only show emission lines of less ionised atoms than in Seyfert galaxies. They are most likely low luminosity Seyfert galaxies and are therefore often referred to as *low-luminosity active galactic nuclei* (LLAGN). LINERs are very common, being detectable in at least a third of all nearby galaxies (Ho *et al.*, 1997).

Some galaxies with active nuclei are also strong radio emitters. Almost all of these **radio galaxies** are elliptical galaxies. The radio emission is not constrained to the nucleus alone but also appears in extended jets which emanate from the nucleus. The jets, which are often – but not necessarily – symmetric, consist of a collimated outflow of relativistic particles spiralling in a magnetic field. This leads to the emission of synchrotron radiation, mainly at radio frequencies. The jets span enormous sizes: coming from the very nucleus on sub-parsec scales, they reach out to several 100 kpc or even Mpc. Large dumbbell-shaped radio lobes appear where the jets impinge on the intergalactic medium. Radio galaxies are classified after Fanaroff and Riley (1974): Fanaroff-Riley type I (**FR I**) galaxies harbour lower luminosity radio sources which are brightest in the centre and whose radio spectra are steepest at the edges of the radio lobes. An example is the elliptical galaxy M 87. Fanaroff-Riley type II (**FR II**) galaxies are more luminous in the radio regime; they exhibit edge-brightened radio lobes (also called “hot spots”) and have the steepest radio spectrum in the inner regions. A prominent FR II galaxy is Cygnus A. In analogy to Seyfert galaxies, radio galaxies can be divided into **narrow line radio galaxies** (NLRG) and **broad line radio galaxies** (BLRG), depending on the widths of their optical emission lines.

AGN with strong radio emission are also called **radio-loud AGN**. Only 10 – 20 % of all AGN are radio-loud (Kellermann *et al.*, 1989). Whether there is a clear bimodality between the population of radio-loud and **radio-quiet AGN**, or whether there is only a very broad distribution of radio-loudness, is still a matter of debate (see Sikora *et al.*, 2007 and White *et al.*, 2007 and references therein). As a working definition, radio-loud AGN have a flux density at radio wavelengths (*e.g.* at 6 cm) that is significantly higher than the optical flux density (*e.g.* at 440 nm): $F_{\text{radio}} \gtrsim 10 \cdot F_{\text{optical}}$ (Kellermann *et al.*, 1989). The ratio $R_{\text{rl}} = F_{\text{radio}}/F_{\text{optical}}$ is referred to as the *radio loudness parameter*.

The most powerful radio-loud AGN are **quasars**. At the same time, they are the most energetic sources in the universe. Initially, the radio sources identified as quasars looked like stars in the optical, which lead to their designation as “**quasi stellar radio sources**”. A breakthrough in the understanding of quasars was achieved in 1963 by Maarten Schmidt: He identified the emission lines in the spectrum of the quasar 3C 273 and recognised its high redshift of $z = 0.158$ (Schmidt, 1963). It was immediately clear that these objects could not be stars but must be objects at very large distances. This implied extremely high luminosities, and a new physical context was required to explain the enormous release of energy. That such a large energy release must have implications on galaxy formation and evolution was also immediately recognised. Similar to quasars, radio-quiet high luminosity AGN were labeled “quasi-stellar objects” (**QSOs**), although the term “quasar” is often used for both classes of objects². The optical spectra of quasars and QSOs are similar to those of Seyfert galaxies, although the broad emission lines are, in general, stronger with respect to the narrow lines than in Seyfert galaxies. Due to the high luminosity of the nucleus and the large distance, the underlying galaxy, the *host galaxy*, is normally not seen; hence their stellar appearance. Quasars are more frequently found in the past. The maximum of their number density is located at $z \sim 2.5$ (Richards *et al.*, 2006; Hopkins *et al.*, 2007), coinciding roughly with the peak in star formation (Hopkins and Beacom, 2006).

The final class of AGN to be listed here, namely **blazars**, are objects that exhibit a high variability in the visible. Blazars are often subdivided into **BL Lacertae objects** (BL Lac; named after the first object of this class, BL Lacertae, which was initially thought to be a highly variable star) and **optically violent variables** (OVVs). Blazars show variations of their luminosity on timescales as short as hours, and their radiation is highly polarised (on the order of a few percent). In contrast to OVVs, which have strong broad emission lines, the spectra of BL Lac objects show almost no emission or absorption lines. The scientific consensus is that in these objects the jet axis is roughly aligned with our line of sight, so that the relativistically outflowing component is directed towards us. This gives rise to beamed synchrotron radiation dominating the spectrum from the radio to the infrared.

1.2 The physical picture of AGN

The entire “zoo of AGN” presented in the previous section has one property in common: a very large amount of energy is released within a very small volume. In the brightest quasars, the bolometric energy output of the nucleus is on the order of 10^{41} W, that is, $L_{\text{bol}} \sim 10^{15} L_{\odot}$. From the size of the radio lobes, one can derive that the sources must have been in an active state for more than 10^7 years. By consequence, the total energy output of the most luminous AGN is on the order of $E = 10^{56}$ J. Variability on scales of hours indicates that the region where the energy is set free has a size of only a few light hours or days, which corresponds to approximately 10 AU or 10^{12} m. Nuclear fusion is not able to set free the required amounts

²One then speaks of *radio-loud quasars* (RLQs) and *radio-quiet quasars* (RQQs).

of energy in such a small volume. Its efficiency factor for the conversion of matter to energy is too low: $\epsilon \sim 0.8\%$.

It became clear very early that the energy must come from the release of gravitational energy from accretion onto a very compact and massive object, most likely a black hole (Hoyle and Fowler, 1963; Salpeter, 1964; Rees, 1984). The accretion luminosity is given by

$$L_{\text{acc}} = \epsilon \dot{M} c^2, \quad (1.1)$$

where ϵ is the radiative efficiency, \dot{M} the accretion rate and c the speed of light.

The nature of the massive compact object was the reason for some speculation. Apart from black holes, other objects such as massive compact star clusters or supermassive stars were proposed. However, due to the deepening of the potential well by the accretion process, such precursor objects are all expected to collapse to a black hole sooner or later (Rees, 1984). Today the scientific consensus is that most galaxies harbour a massive black hole at their centre, which is surrounded by an *accretion disk*. The radiative efficiency ϵ for accretion of matter onto a black hole is much higher than for nuclear fusion and ranges from 6% for a non-rotating black hole to 42% for a rapidly rotating black hole (Krolik, 1999). The masses of the black holes located at the centres of galaxies span a range from $10^6 - 10^{10} M_{\odot}$ (e.g. Shankar *et al.*, 2004). They are normally referred to as *supermassive black holes* (SMBHs).

Because of the common source of energy, similar processes must be occurring in all types of AGN. It is therefore expected that all observational differences in their appearance can be explained by only a few free “parameters”. The most important of these “parameters” are the orientation, the luminosity of the accretion disk and the presence of radio jets. This is the idea behind unifying models, also referred to as *unified schemes* of AGN.

The **luminosity** of an AGN primarily depends on its accretion rate, which in turn depends on the mass of the central black hole and on the amount of fuel available. Assuming a spherical symmetry, an upper limit for the luminosity from accretion is given by the *Eddington luminosity* L_E (Eddington, 1925). This luminosity is reached when the radiation pressure balances the gravitational pull of the black hole:

$$L_{\text{acc}} \leq L_E = 3.3 \cdot 10^{11} L_{\odot} \frac{M_{\text{BH}}}{10^7 M_{\odot}}, \quad (1.2)$$

where M_{BH} is the mass of the black hole. In reality, the geometry is rather axially than spherically symmetric. Luminosities and accretion rates higher than the Eddington limit in so-called *super-Eddington accretion* are then possible. The fuelling of the AGN is connected to the structure of its host galaxy at larger scales. Although the fuelling mechanism is not yet entirely understood, both merger events and instabilities in the galaxy disk, such as spirals and bars, are suspected to trigger the inflow of matter to the nucleus (Combes, 2001).

The details of the processes that lead to the production of **jets** are still unknown. The presence or absence of jets is possibly connected to the spin as well as to the fuelling efficiency of the black hole. It most likely involves the presence of magnetic fields and depends on the details of the accretion process, which is still not well understood (Meier, 2002, 2004).

Orientation effects are thought to be responsible for the Seyfert type 1 and type 2 dichotomy (Antonucci, 1993; Urry and Padovani, 1995). Because of the accretion disk, the jets and a toroidal distribution of obscuring dust surrounding the innermost region of the AGN, the symmetry of the system is expected to be axial (see figure 1.1). Face-on systems, with a jet that points directly towards us, produce blazar-type objects. Systems at high

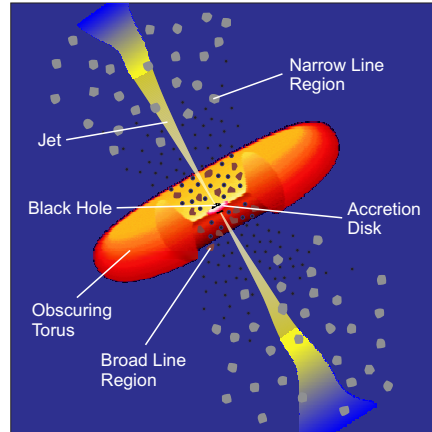


Figure 1.1: Picture of an active galactic nucleus (AGN) in the unified scheme after Urry and Padovani (1995). The main components of an AGN are shown: a supermassive black hole is surrounded by an accretion disk and, at larger scales, by a dusty torus. The latter may obscure the innermost region for an edge-on observer. Near the centre, high velocity clouds ionised by the radiation from the accretion disk emit broad emission lines (BLR). At larger distances, low velocity clouds emit narrow emission lines (NLR). A jet or outflow may emanate from the innermost regions and spread out over large scales. In the currently accepted paradigm, the torus is expected to be thicker than depicted in this sketch (*c.f.* also figure 4.17).

inclination³, where we can directly see the inner regions of the nucleus, are classified as Seyfert 1 nuclei. In this case, we have a free line of sight towards the high velocity gas near the nucleus. Because this gas is responsible for the broad emission lines characteristic for type 1 nuclei, the region where the gas resides is called the *broad line region*. From an edge-on viewing position (the Seyfert 2 case), the view towards the centre is obscured by the dusty torus. We only see the low-density, low-velocity gas at larger distances from the heating source. This gas produces the narrow emission lines and thus defines the *narrow line region*. Assuming a random orientation of the sources on the sky, it is possible to estimate the opening angle of the obscuring torus from the ratio of Seyfert 1 to Seyfert 2 galaxies, which is about 1 : 3 (see section 1.1). This yields a value of approximately 70° , which is in rough agreement with the observed opening angles of ionisation cones or outflows.

With increasing X-ray luminosity, the number of type 2 objects decreases (Ueda *et al.*, 2003). This cannot be explained in terms of the simple unified scheme, where the dust distribution does not depend on the luminosity of the central engine. It seems that the properties of the dust torus are also governed by the mass of the black hole and the accretion state of the nucleus.

The unified picture of Seyfert galaxies was strongly supported by the first observation of broad emission lines in polarised light in the Seyfert 2 galaxy NGC 1068 (Antonucci and Miller, 1985). This light is interpreted to come from the high velocity clouds near the nucleus, the *broad emission line region* (BLR), and to be scattered into our line of sight by clouds above the torus. Today, many more such hidden BLR are known and they seem to be present in at least 30% of all Seyfert 2 galaxies (Tran, 2001).

The main components in the standard paradigm of AGN can be summarised as follows:

³Throughout this thesis, the inclination i is defined as the angle between the symmetry axis of the system, *e.g.* the axis of the torus or the jet axis, and the plane of the sky. In this sense, face-on objects are fully inclined ($i = 90^\circ$) and edge-on objects are not inclined ($i = 0^\circ$).

- A **supermassive black hole** with a mass $M_{\text{BH}} = 10^6 - 10^{10} M_{\odot}$ and a size of $R_{\text{S}} \ll 10^{-3}$ pc resides at the centre of the nucleus.
- The black hole is surrounded by an **accretion disk** with $r_{\text{disk}} \ll 0.1$ pc, consisting of a hot ($10^4 - 10^6$ K) and normally optically thick plasma. This disk is the actual energy source of the AGN.
- In the **broad line region** (BLR, $0.01 - 0.1$ pc), dense gas clouds orbit the black hole with high velocities. The gas is ionised by the radiation from the accretion disk and emits allowed, broad emission lines.
- The central region is embedded in a **dusty molecular torus** with a size of $1 - 10$ pc. The inner border of this torus is set by the dust sublimation temperature, $T_{\text{sub}} = 1500$ K.
- At larger distances ($10 - 1000$ pc), in the **narrow line region** (NLR), less dense gas clouds are located above and below the torus. The gas is photoionised by the strong nuclear radiation field and emits allowed and forbidden narrow emission lines.
- Emanating from the region above and below the accretion disk, collimated **jets** extend from $0.01 - 10^6$ pc.

1.3 The spectral energy distribution of AGN

The continuum emission of AGN covers the entire electromagnetic spectrum from radio emission to γ -rays. In total, the spectrum (in νF_{ν}) of AGN is relatively flat. As an example for the *spectral energy distribution* (SED) of AGN, the mean SED for quasars is shown in figure 1.2.

The X-ray spectrum, which contributes approximately 10% to the bolometric luminosity of AGN, consists of several components. These include a power law continuum, a “soft excess” below X-ray energies of 1 keV (Arnaud *et al.*, 1985), and a “reflection hump” between 10 and 30 keV (George and Fabian, 1991). Photon energies extend to several GeV and, in some objects, even higher to γ -rays with energies in the TeV region (Horan and Weekes, 2004). For photon energies from 1 to 10 keV, the continuum can be represented by a power law $F_{\nu} \propto \nu^{\alpha}$, with $\alpha \sim -0.8$ (Nandra and Pounds, 1994; Tozzi *et al.*, 2006). The spectrum is by consequence not that of thermal emission, *i.e.* not that of blackbody spectra. It results from inverse Compton scattering in the hot corona above the accretion disk (Liang, 1979; Torricelli-Ciamponi *et al.*, 2005). Due to the generation of the emission close to the nucleus, it often shows variations on timescales of weeks or days.

Between 10 and 400 nm, the spectrum shows another local maximum, the *blue bump*. This bump is of thermal nature. Generally, it is attributed to thermal radiation at temperatures of 10^4 to 10^5 K, albeit that its origin is not entirely clear. The emission might be caused either by optically thick, hot gas, *i.e.* blackbody radiation, or by free-free emission of optically thin gas (Barvainis, 1993). The most favoured understanding is that the emission originates from the supposed accretion disk (Shields, 1978; Malkan and Sargent, 1982; Shang *et al.*, 2005).

In the infrared, the continuum radiation of active galactic nuclei shows a thermal peak at wavelengths between 2 and 300 μm . This smooth bump, separated from the blue bump by a local minimum at $\sim 1 \mu\text{m}$, is frequently referred to as the *infrared bump*. Because of its thermal spectrum, the infrared bump is mainly ascribed to the emission from dust with $T \lesssim 1500$ K (Rees *et al.*, 1969; Lebofsky and Rieke, 1980; Barvainis, 1987). This dust is associated with the dusty torus.

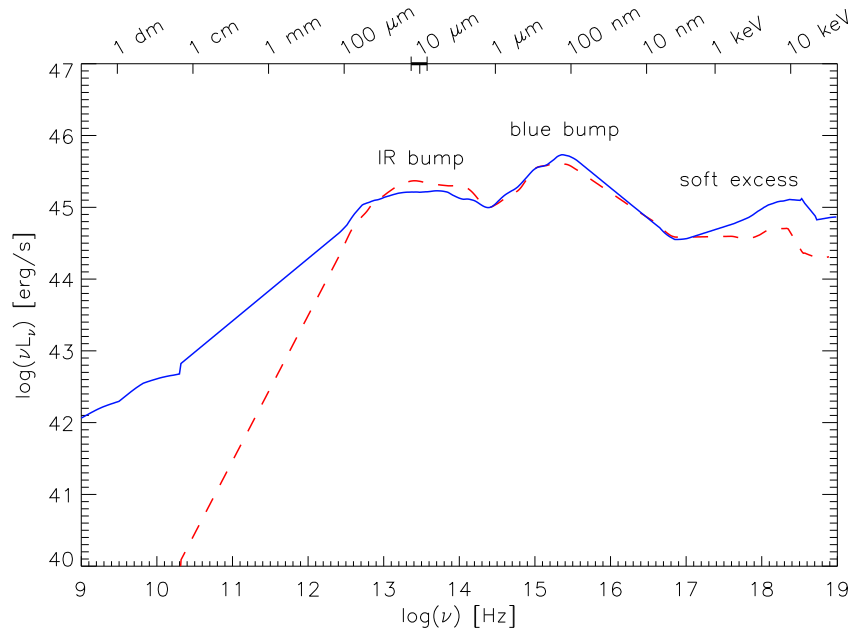


Figure 1.2: Mean quasar spectral energy distribution for radio-loud (blue line) and radio-quiet (red dashed line) quasars. The energy distribution was adapted from Elvis *et al.* (1994). In the spectral regions around the wavelengths of 1 mm and 10 nm, no data is available and the curve is interpolated.

Depending on whether the AGN is radio-loud or radio-quiet, the emission in the radio regime is more or less pronounced. The radio spectrum is non-thermal and the spectral intensity follows a power law $F(\nu) \propto \nu^\alpha$. The radiation is due to synchrotron emission of relativistic electrons in the jets.

1.4 The dusty torus

The dusty molecular torus surrounding the central engine of an AGN is expected to consist of molecular gas as well as of warm and hot ($T \sim 100 - 1500$ K) dust. It is thought to be heated by the nuclear radiation it absorbs in the optical and ultraviolet. The dust is supposed to be a mixture of silicate and graphite grains of various sizes, ranging from a few nm to several μm . The extreme physical conditions found in AGN make it likely that the dust has a different composition different from the interstellar dust observed in the *Milky Way*. Indeed, an indication that the dust in active nuclei has “anomalous” properties, was presented in Maiolino *et al.* (2001b,a). However, only very little research has been performed on the characteristics of the dust in AGN, so that its properties remain essentially unknown.

The difference in the shape of the infrared bump in Seyfert 1 and Seyfert 2 galaxies can be used to probe the distribution of the dust. Of particular importance for such studies are the absorption characteristics of silicate grains. Grains of amorphous silicate show two prominent absorption or emission features at 9.7 and 18.5 μm . The features appear in **emission** in two cases: (i) for an optically thin and warm dust distribution or (ii) for an optically thick dust distribution where the temperature decreases along the observers line of sight. The features appear in **absorption** for an optically thick dust distribution with increasing dust temperature along the line of sight. As was realised by Pier and Krolik (1992), the feature

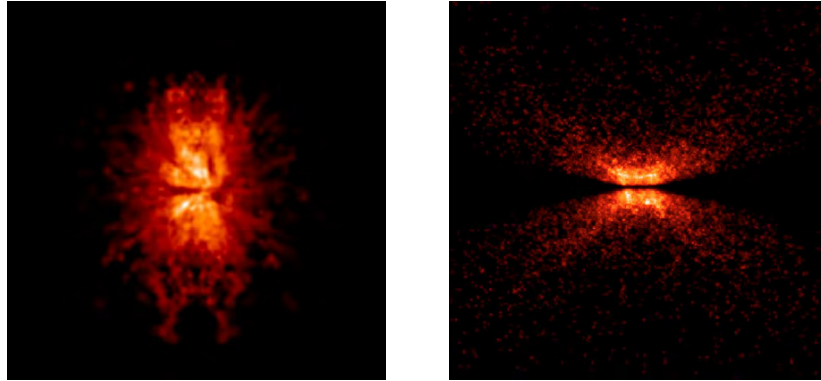


Figure 1.3: Brightness distributions of contemporary torus models for an edge-on viewing position. Left: Hydrodynamic and radiative transfer modelling from Schartmann (2007). Right: Radiative transfer calculations for a torus model from Hönic *et al.* (2006). In both models, a dark lane is visible in the midplane due to the anisotropic radiation characteristic of the accretion disk.

should appear in absorption for a torus seen edge-on (the Seyfert 2 case) and in emission for a face-on torus (the Seyfert 1 case). This is indeed the case: the silicate feature is found in deeper absorption in type 2 objects than in type 1 objects (Roche *et al.*, 1991; Shi *et al.*, 2006; Hao *et al.*, 2007). The feature was also found in emission in several type 1 quasars (Siebenmorgen *et al.*, 2005; Sturm *et al.*, 2005).

Most of the argumentation in favour of the dusty torus involves radiative transfer modelling. The aim of these models is to reproduce the observed SED of type 1 and type 2 objects by simply changing the inclination angle of the torus and adjusting the luminosity of the central energy source. The first simulation of this kind was that of Pier and Krolik (1992), which used a homogeneous cylindrical distribution of dust. This was followed by models of wedge-shaped dust distributions with different types of dust grains by Granato and Danese (1994). The discussion primarily focused on the strength of the silicate feature, as the models produced a deeper absorption feature for edge-on objects and a larger emission feature for face-on objects than actually observed. The primary goal of all following simulations was to reduce the feature strength in the models by modifying the dust distribution or composition (van Bemmelen and Dullemond, 2003; Schartmann *et al.*, 2005; Fritz *et al.*, 2006). Although it was realised early that the dust distribution would most probably be clumpy (Krolik and Begelman, 1988), the first simulation taking clumpiness into account was carried out by Nenkova *et al.* (2002). Subsequent clumpy models to be mentioned are those by Dullemond and van Bemmelen (2005), Hönic *et al.* (2006) and Schartmann *et al.* (2007). A further problem, especially in models with a continuous dust distribution, is the question of how the dust is prevented from collapsing to a disk. A large step forward are the first fully hydrodynamical and therefore truly physical models of AGN tori presented in Schartmann (2007). To illustrate the current status of the simulations, brightness distributions from the clumpy models by Hönic *et al.* (2006) and the hydrodynamical simulations by Schartmann (2007) are compared in figure 1.3.

Despite all the indirect evidence for the existence of a dusty torus and the success of the models, direct evidence is scarce: there are almost no direct observations of the nuclear distribution of molecular gas and dust in AGN. The only exceptions are those presented in Jaffe *et al.* (2004); Poncelet *et al.* (2006). Thus, there is an urgent need for more direct observations of the nuclear dust distribution, for mapping its morphology and for determining

the properties of the dust. To probe the dust distribution, observations have to be carried out in the mid-infrared, as the emission of the warm dust with $100\text{ K} \lesssim T_{\text{dust}} \lesssim 600\text{ K}$ peaks in this wavelength range (see figure 1.2). On the other hand, the sizes expected for the torus from the simulations above are on the order of a few parsec. For the nearest AGN, which are at distances of $d > 4\text{ Mpc}$, the torus will thus have angular sizes of less than 50 mas. The largest contemporary optical telescopes, however, only reach an angular resolution of 250 mas in the mid-infrared (see section 1.6). It is easy to see that, with current telescopes, the nuclear MIR sources of active galaxies remain unresolved. Indeed, unresolved point sources are seen in most AGN in the mid-infrared (Gorjian *et al.*, 2004; Raban *et al.*, 2007). The strategy for overcoming this limitation will form the subject of chapter 2.

1.5 The mid-infrared

The mid-infrared (MIR) is the wavelength range from 5 to $\sim 30\ \mu\text{m}$. It is also called thermal infrared, because the peak of the radiation of a black body with a temperature of $\sim 300\text{ K}$ is located at about $10\ \mu\text{m}$. Most of the astronomical radiation in the MIR is of thermal origin, opposed to *e.g.* synchrotron radiation, which dominates in the radio regime. The total temperature range for emission in the MIR is 100 – 1000 K. These temperatures are characteristic for planets (*e.g.* the earth and all life on it), comets, asteroids and protoplanetary disks, as well as warm dust. The temperatures are lower than those of cool stars, where $T > 1500\text{ K}$. While stellar light dominates in the visual and near-infrared, stars are only seen in the Rayleigh-Jeans regime of their spectra in the MIR. The mid-infrared mainly traces photons reprocessed by dusty environments, that is, the dust absorbs ultraviolet and optical radiation and re-emits it in the infrared.

Our view towards astronomical objects is often obscured by dust. Examples for such objects are embedded stars or the nuclei of galaxies which are obscured by the dust in the disk of their host galaxy. The infrared enables us to penetrate this obscuration, as the mass extinction coefficient decreases towards longer wavelengths (Draine and Lee, 1984). Thus, observing in the MIR not only makes it possible to probe the warm dust itself but also to look into or through it.

In the mid-infrared, the atmosphere is not transparent due to molecular absorption bands, mainly by water vapour but also by carbon dioxide, ozone, oxygen, nitric oxid and methane. For this reason, most mid- and far-infrared observations are carried out by observatories above the atmosphere, that is, by space observatories such as IRAS, ISO and the Spitzer Space Telescope (Neugebauer *et al.*, 1984; Kessler *et al.*, 1996; Werner *et al.*, 2004). These observatories have mirror sizes of less than 1 m and, by consequence, a limited spatial resolution (*e.g.* less than 2.5 arcsec at $10\ \mu\text{m}$). Fortunately, there are two atmospheric transmission bands in the MIR, which enable observations from the earth: the N and the Q band. The atmospheric transmission in the mid-infrared is shown in figure 1.4. The N band atmospheric window ranges from 8 to $13\ \mu\text{m}$. It is interrupted by an ozone absorption feature between 9.3 and $10.0\ \mu\text{m}$. At longer wavelengths, from 17 to $26\ \mu\text{m}$, the Q band follows. It is interrupted by many absorption features, mainly by water vapour. A low water vapour content in the atmosphere above the telescope leads to a higher transmission for both the N and the Q band. This can be achieved by a high altitude of the observatory, a low humidity of the atmosphere (*i.e.* a dry location) and pointings of the telescope with a small zenith angle, *i.e.* a low *airmass*⁴. As an additional coincidence, the N band almost perfectly covers the silicate

⁴The airmass is the optical path length through the earth's atmosphere normalised to the path length at zenith.

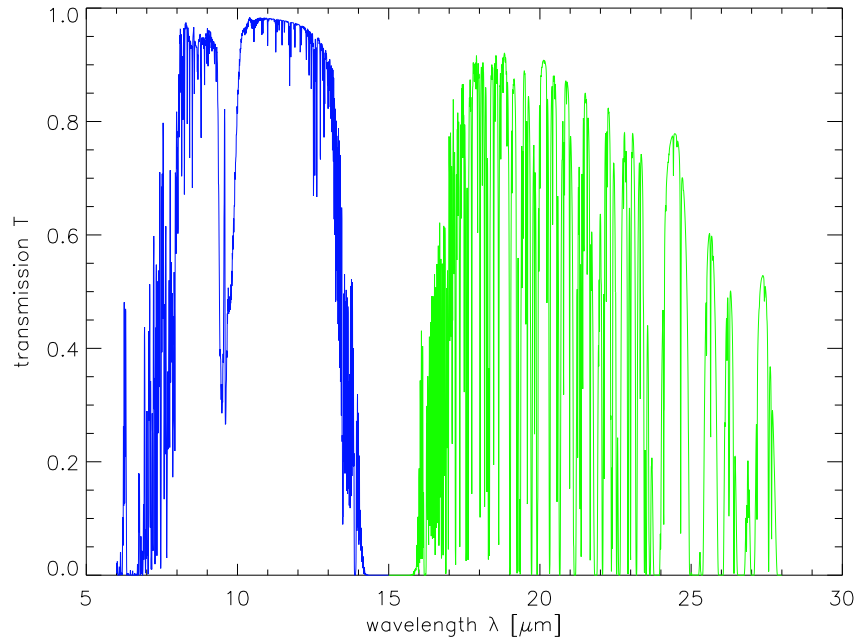


Figure 1.4: Atmospheric transmission in the N (blue) and Q (green) band. The transmission curve was calculated using the ATRAN modelling software for an airmass of 1.5 (corresponding to a zenith angle of 48°) and 1.0 mm of water vapour (Lord, 1992).

absorption feature at $9.7 \mu\text{m}$, which can be used as a diagnostic tool to probe the properties of the dust and its distribution (see section 1.4).

Observations in the MIR require the use of special detectors and optical components. The detectors are *blocked impurity band (BIB) conduction devices* made of special silicon doped with arsenic (Si:As) (Beletic, 2005). The sizes of such detectors (1024×1024 pixels at most) are currently much smaller than those for optical wavelengths (Rieke, 2007). All optical parts, such as mirrors, lenses, filter wheels or dispersive elements, have to be made of special materials in order to transmit or reflect the MIR light. For example, mirrors are coated with gold instead of aluminium. The detectors and optical components have to be cooled to very low temperatures, often only a few degrees above the absolute zero point. Another drawback of (especially terrestrial) observations in the MIR is the high level of background radiation, which is normally several magnitudes stronger than that of the astronomical object. Contributions to the background come from every warm optical component (atmosphere, lenses, mirrors, etc.) which is not perfectly transparent or reflecting. Special observing and data reduction methods have to be implemented in order to obtain scientifically useful data (see chapter 3).

1.6 High resolution observational methods

The angular resolution of a telescope is limited by the size of its primary mirror. This can be explained by the interference of the light coming through the approximately circular aperture with itself. According to the Rayleigh criterion for a circular aperture, the angular resolution is given by

$$\sin \alpha = 1.22 \frac{\lambda}{D}, \quad (1.3)$$

where D is the diameter of the telescope and λ the wavelength of observation. The largest contemporary optical telescopes have diameters of the primary mirror of up to $D = 10$ m, which leads to an angular resolution of $\alpha = 250$ mas in the MIR at $10 \mu\text{m}$. Apart from this physical limitation, there is an additional limitation imposed by the atmosphere for terrestrial observations: “The twinkling of the stars is the astronomer’s nightmare” is a nice way of describing this problem. Inhomogeneities in the refractive index of the air, which are due to turbulence in the earth’s atmosphere, distort the plane wavefronts on the last few kilometers of their journey from distant astronomical objects to us. This effect, the so-called *seeing*, limits the angular resolution to values of about 1 arcsec. The exact value depends on the details of the seeing condition, that is, the strength of the atmospheric turbulence.

There are three possible solutions to the problem of the limited resolution imposed by the atmosphere for single telescopes in the infrared:

1. Circumvention of the problem by positioning the observatory outside the disturbing effects of the atmosphere, that is, by building a satellite. This is very costly, but has the advantage that the limitations by atmospheric absorption are removed, at the same time.
2. In *lucky imaging*, many short (on the order of a few milliseconds) exposures of the targeted object are taken. Only those images are selected for the further processing where the wavefront is more or less flat by “luck”. The image then has a higher resolution than in the seeing limited case. This is, however, only possible for bright targets which are seen in a single short exposure.
3. Finally, it is possible to “undo” the deformation of the wavefront caused by the atmosphere by a specially devised system using a deformable mirror. Such a system is called an *adaptive optics* (AO) system.

The idea to correct the turbulences in the atmosphere with a deformable mirror was first put forth by H. Babcock (Babcock, 1953). The two principle elements of such an adaptive optics system were recognised by Babcock to be a *wavefront sensor* (WFS) to determine the deformation of the wavefront and a *deformable mirror* (DM) to undo the distortions in the wavefront. Because of the high technical demands on such a system and thus its high costs, it took several decades, until a working system was implemented. In the meantime, many observatories have equipped their telescopes with adaptive optics systems and almost all 8 to 10 m class telescopes world wide use adaptive optics in order to reach their diffraction limit.

In the mid-infrared, the angular resolutions of even the largest AO assisted telescopes are not sufficient to resolve the nuclear dust emission in AGN, because the limitations are imposed by the diffraction. Unrealistically large single-dish telescopes ($D > 50$ m) would be required to reach the necessary angular resolution of less than 50 mas. With the current technology, the only way to overcome the limitation by diffraction is by using interferometry.

Based on these considerations, the task is now well defined: **in order to directly investigate the dust distribution in AGN, high resolution interferometric observations in the mid-infrared are necessary.** For the observations presented in this thesis, the diffraction limited light from two 8 m telescopes, after correction by an adaptive optics system, was used for the interferometric measurements.

Chapter 2

Interferometry

This chapter begins with an introduction to the basics of interferometry. In the second part of the chapter, the instrumental set-up of the VLTI and the MIDI instrument will be addressed. A complete introduction to optical interferometry is given in Lawson (2000b) and in the proceedings to the *Euro Summer School* on “Observation and Data reduction with the Very Large Telescope Interferometer” (to be published in *New A Rev.*). Much of the content of the following is adapted from these publications.

2.1 Basics of interferometry

2.1.1 Monochromatic point source

Optical interferometry in astronomy is essentially the same as Young’s double pinhole experiment (Young, 1804). However, instead of having two pinholes in a first screen and a second screen for the display of the interferometric pattern, the pinholes are replaced by two telescopes and an interferometric instrument takes the place of the second screen. The basic layout of such an interferometer is shown in figure 2.1. The two telescopes are located at the positions \vec{x}_A and \vec{x}_B . The separation vector between the two telescopes of the interferometer is the baseline \vec{B} :

$$\vec{B} = \vec{x}_B - \vec{x}_A. \quad (2.1)$$

The two telescopes are pointing at an astronomical source, which is located at the position \vec{S} with respect to the middle of the baseline. The pointing direction of the telescopes is given by the unit vector

$$\vec{s} = \frac{\vec{S}}{|\vec{S}|}. \quad (2.2)$$

For a monochromatic point source at a large distance, the electromagnetic field can be described as a plane wave with the angular frequency $\omega = 2\pi\nu$. At the positions \vec{x}_A and \vec{x}_B , the field is given by

$$\vec{E}_A = \vec{E}_{A,0} e^{i\vec{k}\vec{x}_A - i\omega t} \quad (2.3)$$

$$\begin{aligned} \vec{E}_B &= \vec{E}_{B,0} e^{i\vec{k}\vec{x}_B - i\omega t} \\ &= \vec{E}_{B,0} e^{i\vec{k}\vec{x}_A + i\vec{k}\vec{B} - i\omega t} \end{aligned} \quad (2.4)$$

where $\vec{k} = -k\vec{s} = -2\pi/\lambda \cdot \vec{s} = -\omega/c \cdot \vec{s}$ is the wave vector. Without loss of generality, the common phase $\phi_{\text{common}} = i\vec{k}\vec{x}_A$ can be omitted, so that

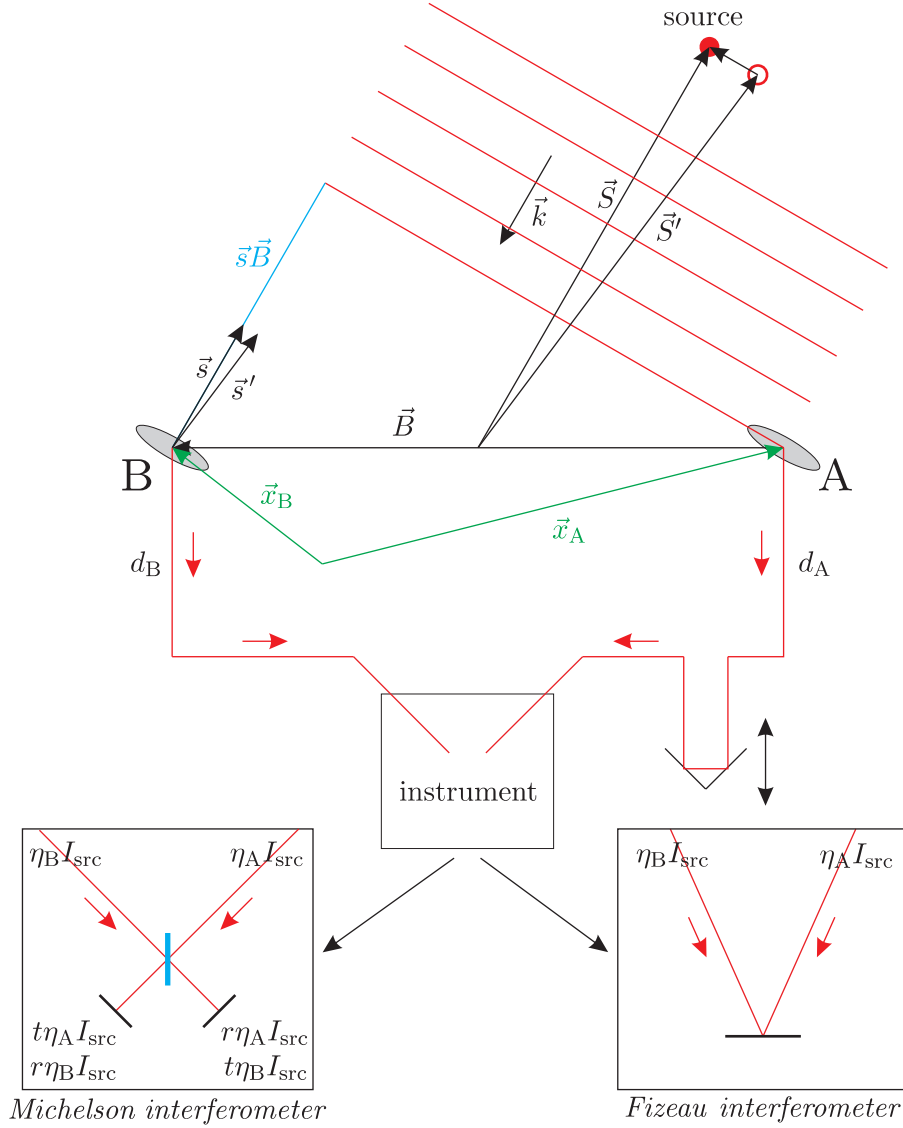


Figure 2.1: Basic layout of an astronomical interferometer. Two possible ways to interfere the light are sketched: the Michelson interferometer and the Fizeau interferometer. See text for details.

$$\vec{E}_A = \vec{E}_{A,0} e^{-i\omega t} \quad (2.5)$$

$$\vec{E}_B = \vec{E}_{B,0} e^{-ik\vec{s}\vec{B}} e^{-i\omega t}. \quad (2.6)$$

This essentially means that the relative phase shift between the signal in the two apertures is determined by the difference in the optical path: $\vec{s}\vec{B}$. The light is then propagated along two paths with the lengths d_A and d_B towards the detector, where the electromagnetic fields take the form:

$$\vec{E}_A = \vec{E}_{A,0} e^{ikd_A} e^{-i\omega t} \quad (2.7)$$

$$\vec{E}_B = \vec{E}_{B,0} e^{ikd_B} e^{-ik\vec{s}\vec{B}} e^{-i\omega t}. \quad (2.8)$$

An optical or infrared detector only measures the time-averaged intensity $I_{\text{det}} = \left| \vec{E} \right|^2 = \vec{E} \cdot \vec{E}^*$ of the total electrical field $\vec{E} = \vec{E}_A + \vec{E}_B$:

$$\begin{aligned} I_{\text{det}} &= \left(\vec{E}_A + \vec{E}_B \right) \cdot \left(\vec{E}_A^* + \vec{E}_B^* \right) \\ &= \vec{E}_{A,0}^2 + \vec{E}_{A,0} \vec{E}_{B,0} e^{ik(d_A - d_B + \vec{s}\vec{B})} + \vec{E}_{A,0} \vec{E}_{B,0} e^{-ik(d_A - d_B + \vec{s}\vec{B})} + \vec{E}_{B,0}^2 \\ &= I_A + I_B + \sqrt{I_A I_B} \cdot 2 \cos \left[k \left(d_A - d_B + \vec{s}\vec{B} \right) \right] \end{aligned} \quad (2.9)$$

$$= I_{\text{src}} (\eta_A + \eta_B + 2\sqrt{\eta_A \eta_B} \cdot \cos k\delta), \quad (2.10)$$

where $\delta = d_A - d_B + \vec{s}\vec{B}$ and the identity $2 \cos \alpha = e^{i\alpha} + e^{-i\alpha}$ was used. Additionally, the factors η_A and η_B were introduced to take into account the different intensities $I_A = \eta_A I_{\text{src}} = \left| \vec{E}_A \right|^2$ and $I_B = \eta_B I_{\text{src}} = \left| \vec{E}_B \right|^2$ of the beams from the two telescopes, *e.g.* due to a different size of the telescopes or the different transmission characteristics of the optical elements. δ is called the *optical path difference* (OPD). Changing d_B in a so-called *optical delay line* will lead to an oscillation of the intensity I_{det} .

The optical path cannot only be changed by varying the internal delay $d = d_A - d_B$, but also depends on $\vec{s}\vec{B}$, that is, on the pointing of the telescopes or the position of the source. Applying the Rayleigh criterion to interferometry, a second source at \vec{S}' is resolved, when the peak of the fringe pattern for the first source falls into at least the first minimum of the fringe pattern of the second source. This means that the two fringe patterns are shifted by half a wavelength with respect to each other:

$$k \left(d + \vec{s}\vec{B} \right) = k \left(d + \vec{s}'\vec{B} \right) + \pi. \quad (2.11)$$

This can be simplified to

$$\left(\vec{s} - \vec{s}' \right) \vec{B} = \frac{\lambda}{2}, \quad (2.12)$$

where the definition of the wave number, $k = 2\pi/\lambda$, was used. Projecting the baseline \vec{B} on the separation vector $\vec{\zeta} = \vec{s} - \vec{s}'$, that is $\left(\vec{s} - \vec{s}' \right) \vec{B} = \zeta B_{\text{proj}}$, we obtain

$$\zeta_{\text{Rayleigh}} = \frac{\lambda}{2B_{\text{proj}}} \quad (2.13)$$

for the resolution of the interferometer. Alternatively, the resolution can be defined as the inverse of the spatial frequency (see section 2.1.3) of the fringe pattern, that is,

$$\zeta_{\text{fringe}} = \frac{\lambda}{B_{\text{proj}}}. \quad (2.14)$$

The latter definition is directly comparable to that of a single telescope as given in section 1.6: B_{proj} corresponds to the diameter D of a single dish telescope and the two telescopes of an interferometer can be seen as two subapertures of a virtual larger telescope with the diameter B_{proj} . Of course, the collecting area of an interferometer is still limited to that of the two individual telescopes, with a corresponding sensitivity. In the following, B_{proj} will be referred to as the *projected baseline* (*length*), BL .

In the case described above, beam combination in the image plane was assumed. In an *image plane* or *Fizeau interferometer*, the two incident light beams are directly focussed to produce an image of the source on the detector, very similar to what takes place in Young's

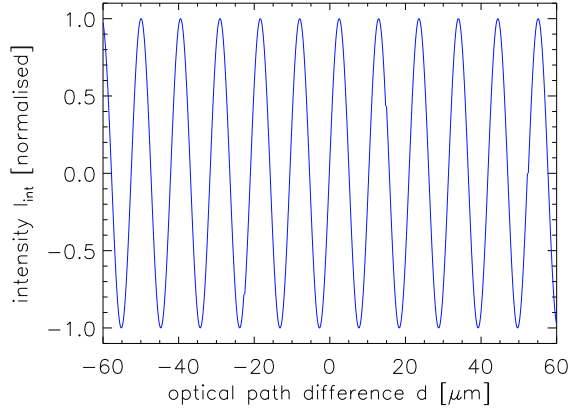


Figure 2.2: Intensity variation of the interferometric signal I_{int} with change of optical path difference d for a monochromatic source with a wavelength of $\lambda = 10.5 \mu\text{m}$. For $d = 0.5\lambda, 1.5\lambda, \dots$ positive interference occurs, while for $d = 0, \lambda, 2\lambda, \dots$ there is negative interference.

experiment. In our case, the beam combination in the pupil plane is relevant. In these *pupil plane* or *Michelson interferometers*, the two beams are superposed coplanar by a half-silvered mirror, the *beam combiner*. The name of such a type of interferometer comes from the fact that the set-up to measure the speed of light by Michelson was a pupil plane interferometer (Michelson and Morley, 1887).

After passing the beam combiner, the two electrical fields take the form

$$\vec{E}_1 = \sqrt{t}\vec{E}_A + \sqrt{r}\vec{E}_B e^{i\frac{\pi}{2}} \quad (2.15)$$

$$\vec{E}_2 = \sqrt{r}\vec{E}_A e^{i\frac{\pi}{2}} + \sqrt{t}\vec{E}_B \quad (2.16)$$

The phase shift $e^{i\frac{\pi}{2}}$ is introduced by the reflection on the half-silvered mirror and the factors r and t are the coefficients for reflection and for transmission of the intensities I_A and I_B respectively (see figure 2.1). The intensities measured by the detector then are

$$I_1 = tI_A + rI_B + 2\sqrt{tI_A rI_B} \cdot \sin k\delta \quad (2.17)$$

$$I_2 = rI_A + tI_B - 2\sqrt{rI_A tI_B} \cdot \sin k\delta \quad (2.18)$$

Because the two output beams are complementary (they have the opposite phase), they can be subtracted from one another:

$$\begin{aligned} I = I_1 - I_2 &= (r - t)(I_A - I_B) + 4\sqrt{rtI_A I_B} \cdot \sin k\delta \\ &= I_{\text{src}} [(r - t)(\eta_A - \eta_B) + 4\sqrt{rt\eta_A \eta_B} \cdot \sin k\delta] \end{aligned} \quad (2.19)$$

For an ideal interferometer, $\eta_A = \eta_B = 1$ and for a perfect beam splitter, $r = t = 0.5$, so that the background $I_{\text{back}} = I_{\text{src}}(r - t)(\eta_A - \eta_B)$ vanishes and only the interferometric component remains:

$$I_{\text{int}} = 4 I_{\text{src}} \sqrt{rt\eta_A \eta_B} \cdot \sin k\delta \quad (2.20)$$

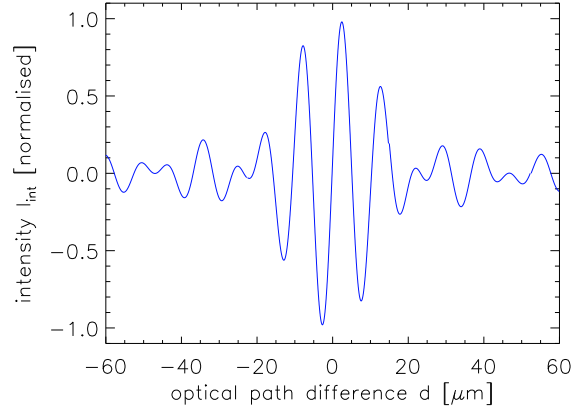
$$= 2 I_{\text{src}} \sin k\delta. \quad (2.21)$$

This signal is shown in figure 2.2. To simplify the calculations, only this interferometric contribution to the total intensity I will be considered in the following.

2.1.2 Polychromatic sources

So far it was assumed that the source is monochromatic. In reality, however, astronomical sources emit light in a large wavelength range with a spectral intensity $I_{\text{src}}(k)$ and the optical set-up has finite passbands $\eta_A(k)$ and $\eta_B(k)$. The electromagnetic waves at different

Figure 2.3: Intensity variation of the interferometric signal I_{int} with change of optical path difference d for a light source emitting polychromatic light with a bandpass of $\Delta\lambda = 5.0\ \mu\text{m}$ centred on a wavelength of $\lambda = 10.5\ \mu\text{m}$. This pattern is the same as in figure 2.2, except for the additional modulation by a sinc function.



wavelengths are mutually uncorrelated. By consequence, the interferometric component of the intensity is simply the integral over all wave numbers:

$$I_{\text{int}} = \int 4 I_{\text{src}}(k) \sqrt{r(k)t(k)\eta_A(k)\eta_B(k)} \cdot \sin k\delta \, dk. \quad (2.22)$$

As an example, a constant source intensity $I_{\text{src}}(k) = I_0$, a perfect beam splitter as well as an ideal interferometer with a bandpass in the form of a top hat function centred at k_0 and with a width Δk shall be considered. The factors $\eta_A(k)$ and $\eta_B(k)$ then take the form

$$\eta_A(k) = \eta_B(k) = \eta(k) = \begin{cases} \eta_0 & \text{for } k_0 - \Delta k/2 < k < k_0 + \Delta k/2 \\ 0 & \text{else.} \end{cases} \quad (2.23)$$

A top hat function can be seen as a first order approximation of the N band (see figure 1.4). With these assumptions, (2.22) reads

$$I_{\text{int}} = 2 I_0 \eta_0 \int_{k_0 - \Delta k/2}^{k_0 + \Delta k/2} \sin k\delta \, dk. \quad (2.24)$$

The integration gives

$$I_{\text{int}} = 2 I_0 \eta_0 \Delta k \sin k_0 \delta \frac{\sin(\Delta k/2 \cdot \delta)}{\Delta k/2 \cdot \delta} \quad (2.25)$$

$$= 2 I_{\text{bp}} \sin k_0 \delta \operatorname{sinc}(\Delta k/2 \cdot \delta) \quad (2.26)$$

with the total collected power in the bandpass $I_{\text{bp}} = I_0 \eta_0 \Delta k$. The behaviour of the intensity with optical path difference is shown in figure 2.3. The result is similar to (2.21) except for the additional modulation by the sinc function. This function becomes small for $|\Delta k/2 \cdot \delta| > 1$. Fringes are hence only observed if the optical delay δ is smaller than the coherence length Λ_{coh} which is defined by

$$\Lambda_{\text{coh}} = \frac{\lambda_0^2 - \Delta\lambda^2/4}{\Delta\lambda} \approx \frac{\lambda_0^2}{\Delta\lambda}, \quad (2.27)$$

where the approximation is valid for $\Delta\lambda \ll \lambda$. For the full N band ($8\ \mu\text{m} < \lambda < 13\ \mu\text{m}$), $\Lambda_{\text{coh}} \sim 21\ \mu\text{m}$. This can nicely be seen in figure 2.3.

If the interferometric signal is dispersed with a spectral resolution of $R = \lambda_0/\Delta\lambda$, then $\Lambda_{\text{coh}} = R\lambda_0 - \lambda_0/4R$. For $R = 30$, $\Lambda_{\text{coh}} \sim 315\ \mu\text{m}$ in the N band ($\lambda_0 = 10.5\ \mu\text{m}$).

It is important to note that the sinc function is the Fourier transform $\mathcal{F}[\eta(k)]$ of the spectral filter function $\eta(k)$. It can be shown more generally that this is true for all shapes of bandpasses and source intensities, *i.e.*

$$I_{\text{int}} = 2 I_{\text{bp}} \sin k_0 \delta \mathcal{F}[\eta(k)](\Lambda_{\text{coh}}, \delta). \quad (2.28)$$

2.1.3 Extended sources

In addition to emitting light at different wavelengths, most astronomical sources are not pure point sources. Similar to the polychromatic case, an extended source can be described as a superposition of coherent point sources which are mutually incoherent:

$$I_{\text{int}} = \int 4 I(\vec{s}) \sqrt{rt\eta_A\eta_B} \sin\left(k\left(d - \vec{s}\vec{B}\right)\right) d\vec{s} \quad (2.29)$$

$$= \frac{2\sqrt{rt\eta_A\eta_B}}{i} \left[e^{ikd} \int I(\vec{s}) e^{-ik\vec{s}\vec{B}} d\vec{s} - e^{-ikd} \int I(\vec{s}) e^{ik\vec{s}\vec{B}} d\vec{s} \right]. \quad (2.30)$$

The two integrals are two-dimensional Fourier transforms of the intensity distribution $I(\vec{s})$:

$$\mathcal{I}(\vec{B}_{\text{proj}}/\lambda) = \int I(\vec{s}) e^{ik\vec{s}\vec{B}} d\vec{s} = \int I(\vec{s}) e^{2\pi i \frac{\vec{s}\vec{B}}{\lambda}} d\vec{s} = \mathcal{F}[I(\vec{s})](\vec{B}_{\text{proj}}/\lambda) \quad (2.31)$$

$$= \tilde{I}(\vec{B}_{\text{proj}}/\lambda) e^{i\phi(\vec{B}_{\text{proj}}/\lambda)}. \quad (2.32)$$

In the last step, the complex number of the Fourier transform was written as the absolute value \tilde{I} and the phase ϕ , which are both functions of the *spatial frequency* $\vec{u} = \vec{B}_{\text{proj}}/\lambda$. The Fourier transform of a real function like $I(\vec{s})$ is Hermitian, that is

$$\mathcal{I}(-\vec{u}) = \tilde{I}(-\vec{u}) e^{i\phi(-\vec{u})} = \tilde{I}(\vec{u}) e^{-i\phi(\vec{u})} = \mathcal{I}^*(\vec{u}). \quad (2.33)$$

This means that, if the two telescopes are exchanged, only the phase changes its sign. $\mathcal{V}(\vec{u}) = \mathcal{I}(\vec{u})$ is called the *complex visibility*, while the *normalised visibility*, which is a real number, is given by

$$V(\vec{u}) = \frac{|\mathcal{V}(\vec{u})|}{|\mathcal{V}(\vec{0})|} = \frac{\tilde{I}(\vec{u})}{\tilde{I}(\vec{0})}. \quad (2.34)$$

Note that $\tilde{I}(\vec{0}) = \int I(\vec{s}) e^{2\pi i \vec{s}\vec{0}} d\vec{s} = I_{\text{src}}$ is the total flux of the source. By definition $V(\vec{0}) = 1$. (2.30) can then be written as

$$I_{\text{int}} = 2\sqrt{rt\eta_A\eta_B} \cdot \left[\frac{e^{ikd}}{i} \cdot \tilde{I}(\vec{u}) \cdot e^{-i\phi(\vec{u})} - \frac{e^{-ikd}}{i} \cdot \tilde{I}(\vec{u}) \cdot e^{i\phi(\vec{u})} \right] \quad (2.35)$$

$$= 4\sqrt{rt\eta_A\eta_B} \cdot \tilde{I}(\vec{u}) \cdot \sin(kd - \phi(\vec{u})) \quad (2.36)$$

$$= 4\sqrt{rt\eta_A\eta_B} \cdot I_{\text{src}} \cdot V(\vec{B}_{\text{proj}}/\lambda) \cdot \sin\left(kd - \phi(\vec{B}_{\text{proj}}/\lambda)\right). \quad (2.37)$$

For unknown delay d and phase ϕ , the visibility can be determined from the interferometric flux I_{int} by

$$V(\vec{B}_{\text{proj}}/\lambda) = \frac{|I_{\text{int}}|}{4\sqrt{rt\eta_A\eta_B} \cdot I_{\text{src}}}. \quad (2.38)$$

2.1.4 Source morphologies

As has been shown in the previous section, the normalised visibility $V(\vec{u})$ is the normalised Fourier transform of the brightness distribution of the source $I(\vec{s})$. This relation is called the *van Cittert-Zernike theorem*. It is hence easy to calculate the expected visibility for an arbitrary baseline and an arbitrary morphology of the source. It is very instructive to look at a few example distributions and to trace the visibility with increasing baseline length for a certain baseline orientation. In this one-dimensional problem, the interferometer is sensitive only to the source brightness distribution projected onto the plane spanned by \vec{B} and \vec{s} , *i.e.* the plane containing the two telescopes and the source. Let r and q be orthogonal coordinates on the sky with r parallel to \vec{B}_{proj} . Then

$$I_{\text{proj}}(r) = \int I(r, q) dq. \quad (2.39)$$

In the following, four examples will be discussed: a point source, a binary, a Gaussian distribution and a uniform disk. These brightness distributions are all used as models for astronomical sources. Both the projected intensities and the visibilities for the example functions are shown in figure 2.4.

2.1.4.1 Point source

A point source can be described mathematically by a Dirac δ -function (figure 2.4 a):

$$I_{\text{proj}}(r) = I_0 \delta(r - r_0). \quad (2.40)$$

The Fourier transform of the δ -function is a constant and so is the visibility (figure 2.4 b):

$$V(B_\lambda) = 1. \quad (2.41)$$

$B_\lambda = B_{\text{proj}}/\lambda = BL/\lambda$ is the projected baseline length expressed in λ (see also section 2.1.1). Not surprisingly, the source remains unresolved independent of the length of the baseline, that is, independent of the spatial frequency.

2.1.4.2 Binary

A binary is composed of two point sources separated by the distance d (figure 2.4 c):

$$I_{\text{proj}}(r) = I_1 \delta\left(r - \frac{d}{2}\right) + I_2 \delta\left(r + \frac{d}{2}\right). \quad (2.42)$$

The separation d is the distance of the sources after projection on the plane parallel to the baseline. It is not the distance of the point sources on the sky. If, for example, the sources are oriented perpendicular to the baseline, the interferometer only sees a single point source: $d = 0$.

The visibility for the binary is given by

$$V(B_\lambda) = \sqrt{\frac{1 + f^2 + 2f \cos(2\pi d B_\lambda)}{(1 + f)^2}}, \quad (2.43)$$

where $f = I_1/I_2$ is the ratio of the flux of the two components (figure 2.4 d). The result is an oscillation with a spatial frequency determined by the distance of the two sources. The amplitude of the oscillation depends on the ratio of the intensities.

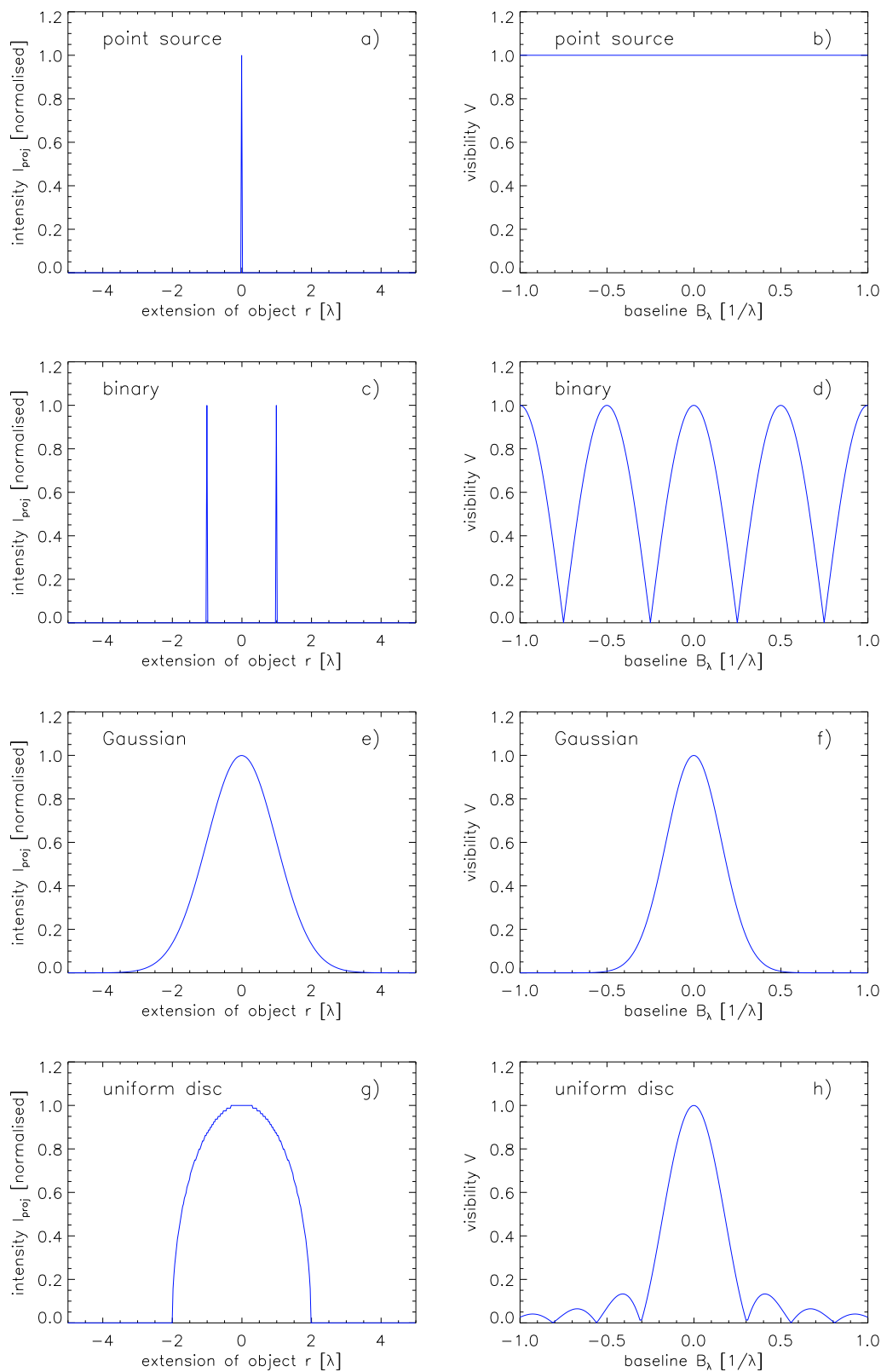


Figure 2.4: Example visibility functions for extended sources (from top to bottom): point source, binary, Gaussian and uniform disc. Left panels: one-dimensional projections for the different source brightness distributions $I_{\text{proj}}(r)$, normalised to 1. Right panels: Respective visibility function $V(B_\lambda)$, also normalised to 1.

2.1.4.3 Gaussian distribution

The projection of an elliptical, two-dimensional Gaussian distribution is again a Gaussian distribution which is given by

$$I_{\text{proj}}(r) = I_0 e^{-\frac{r^2}{2\sigma^2}}. \quad (2.44)$$

It is depicted in figure 2.4 e. The normalised Fourier transform of this function is

$$V(B_\lambda) = e^{-2(\pi\sigma B_\lambda)^2}, \quad (2.45)$$

that is, the Fourier transform of a Gaussian distribution is again a Gaussian distribution (figure 2.4 f). The property of the Gaussian function to remain a Gaussian after projection and performing a Fourier transform make it an ideal function for the analysis of interferometric data.

2.1.4.4 Uniform disk

The projection of a uniform disk of the diameter d onto the plane parallel to the baseline is a semi-ellipse (figure 2.4 g). It is determined by

$$I_{\text{proj}}(r) = \begin{cases} I_0 \sqrt{1 - (2r/d)^2} & \text{for } -d/2 < r < d/2 \\ 0 & \text{else.} \end{cases} \quad (2.46)$$

The corresponding visibility is given by

$$V(B_\lambda) = \left| \frac{2J_1(\pi d B_\lambda)}{\pi d B_\lambda} \right|, \quad (2.47)$$

where $J_1(x) = (2\pi)^{-1} \int_0^{2\pi} \cos(\tau - x \sin \tau) d\tau$ is the Bessel function of the first kind of the order 1 (figure 2.4 h). The function has several roots, where the phase jumps by 2π . A uniform disk is often used to model the visibility functions of resolved stars.

2.1.5 Importance of the phase

In equation (2.32), the complex visibility or *complex degree of coherence* (Traub, 2000) was introduced as

$$\mathcal{I}(\vec{B}) = \int I(\vec{s}) e^{ik\vec{s}\vec{B}} d\vec{s} \quad (2.48)$$

$$= \tilde{I}(\vec{B}) e^{i\phi(\vec{B})}. \quad (2.49)$$

The inverse relation,

$$I(\vec{s}) = \int \mathcal{I}(\vec{B}) e^{-ik\vec{s}\vec{B}} d\vec{B}, \quad (2.50)$$

reconstructs the intensity distribution of the source from the visibility measurements. For this to function, both the absolute value $\tilde{I}(\vec{B}) = V(\vec{B}) \cdot \int I(\vec{s}) d\vec{s}$ or the visibility $V(\vec{B})$ as well as the phase $\phi(\vec{B})$ have to be known for a sufficient number of baselines \vec{B} .

Figure 2.5 visualises the relative importance of the visibility and the phase for image reconstruction. The two images shown in the top row were Fourier transformed and reconstructed by using the amplitude of one image and the phase of the other. The result (shown in the bottom row) makes clear that most of the small scale (spatial) image information is



Figure 2.5: Visualisation of the information content in the phase and in the visibility. The phase and visibility information of the Fourier transforms of the two images in the top row were exchanged and then the inverse Fourier transforms were calculated. The resulting images (bottom row) are similar to those which provided the phase information.

contained in the phase and not in the visibility. Unfortunately, the phase cannot be directly measured in optical interferometry due to the unknown phase introduced by the atmosphere: differences in the refraction index of the atmosphere lead to phase shifts ϕ_{atm} . The atmosphere also leads to short coherence times, that is, the integrations have to be kept short if no corrections for the drift in the phase are applied. Only relative phases, that is, the difference in phase at different wavelengths, can be measured and normally no phase information is available at all (see also section 3.2). There are two ways to overcome these problems:

1. A phase reference is used, *i.e.* a second object nearby is observed simultaneously with the science target. If the phase of this reference object, ϕ_{obj} , is known (*e.g.* when using an unresolved star), the observed phase, ϕ_{obs} can be used to determine the atmospheric phase: $\phi_{\text{atm}} = \phi_{\text{obs}} - \phi_{\text{obj}}$. This method is called *phase referencing*.

2. So-called *closure phases* are observed. At least three telescopes are necessary in order for this to function. The phase differences between the three telescopes have to cancel out and this property can be used to obtain an estimate of ϕ_{atm} . At the VLTI, AMBER can be used to observe closure phases.

Although it might seem a disaster if no phase information is available, the problem is not so severe for most astronomical purposes. Most astronomical sources do not have morphologies as complex as in the pictures shown in figure 2.5. If certain properties of the brightness distribution are assumed (for example that the intensity only increases towards the centre or that the brightness distribution has certain symmetries), the visibility alone can be used to extract useful information on the source. This will be shown in the following chapters. One should, however, always bear in mind that, without any phase information, important information is lacking.

2.1.6 The uv plane

In order to be able to reconstruct any image of the source from the measured visibilities, a large number of baselines must be measured. In the terminology of radio interferometry, the Fourier plane containing the baselines is called the *uv plane*. By convenience, the u and v axes are oriented in direction of the *right ascension* $RA = \alpha$ and the *declination* $DEC = \delta$. The coordinates u and v of this plane are correctly given in spatial frequencies $B_\lambda = B_{\text{proj}}/\lambda$. It is also possible to express u and v in lengths, for example if only the baseline configuration, independent of the observed wavelength λ , is of interest. This representation will be used in the following chapters. Increasing the uv coverage, that is, by adding points in the uv plane by obtaining visibility measurements for different baselines, is called *aperture synthesis*. The idea is to completely fill a hypothetical larger aperture by measuring the visibility and phase at all of its positions. The inverse Fourier transform will then give an image of the sky as if observed with the hypothetical large telescope. In order to increase the coverage, the projected baseline has to be changed. This can be achieved by two methods: either by relocating the telescopes of the interferometer, that is, by physically moving them to different positions, or by making use of the rotation of the Earth. The latter method leads to uv tracks shaped as arcs, depending on the location of the source on the sky.

2.2 The VLTI

Currently there are only two interferometers which, in principle, permit the study of AGN in the infrared: the Very Large Telescope Interferometer (VLTI) and the Keck Interferometer (Glindemann *et al.*, 2000; Colavita and Wizinowich, 2003; Wizinowich *et al.*, 2006). All other existing optical interferometers have been solely conceived for the study of bright stars. Although the Seyfert 1 galaxy NGC 4151 was successfully observed with the Keck Interferometer in the near-infrared (Swain *et al.*, 2003), the possibilities to study the dust distribution in the cores of AGN with this interferometer are limited. No further observations of AGN are foreseen. This is why, in practice, the VLTI is currently the only facility detecting fringes on extragalactic sources. More precisely, only the mid-infrared instrument MIDI is able to perform such interferometric measurements, as attempts to detect fringes from an extragalactic source with the near-infrared instrument AMBER (see section 2.2.4) have been unsuccessful.

A comprehensive description of the VLTI and its subsystems can be found in the VLT White Book (European Southern Observatory, 1998) and in the 32 papers from Session 1



Figure 2.6: Photo from the VLTI platform. On the image, the four unit telescopes (UT1, UT2, UT3 and UT4 from left to right) and the four auxiliary telescopes can be seen. Between UT3 and UT4, the *VLT survey telescope* (VST) towers behind the interferometric laboratory. The rails in the foreground are used to move the auxiliary telescopes; the octagonal covers mark the position of the VLTI stations.

“VLTI: Its subsystems and its instruments” in Lena and Quirrenbach (2000). In the following, the most important facts are summarised.

2.2.1 The site

The VLTI forms part of the *Paranal Observatory* which is located on a 2635 m high mountain, the *Cerro Paranal*, at $24^{\circ}40' S$, $70^{\circ}25' W$ in the Atacama desert in the Republic of Chile. The mountain is located about 130 km south of the city of Antofagasta in the *coastal mountain range* and lies only 12 km from the sea. The special climatic conditions make the site one of the driest locations on Earth. The exceptional aridity makes the atmosphere very transparent at infrared wavelengths, at which there is usually a high amount of absorption due to water vapour (see section 1.5). The remote location also ensures minimal pollution by light and dust due to human civilisation. The observatory is owned and operated by the *European Organisation for Astronomical Research in the Southern Hemisphere* (short *European Southern Observatory*, ESO), an intergovernmental organisation for astronomical research, currently composed of 13 European countries.

2.2.2 The VLTI infrastructure

The entire VLTI infrastructure is located on the flattened top of Cerro Paranal on the *VLTI platform* (see figure 2.6). Four *unit telescopes* (UTs) are located at fixed positions with distances between 47 and 130 m. The unit telescopes have 8.2 m primary mirrors which are controlled by *active optics* (Noethe, 2002). The four telescopes are also referred to as the *Very Large Telescope* (VLT) and are used for single dish observations most of the time. Four movable *auxiliary telescopes* (ATs) are dedicated to interferometry with the VLTI alone. The ATs have primary mirrors with 1.8 m diameter, which means that their light collecting area is only 5% of that of the unit telescopes. The ATs can be relocated between 30 stations in order to allow different baseline configurations. The layout of the total VLTI grid composed of the positions of the UTs as well as the AT stations is shown in figure 2.7. The *delay lines* and the *interferometric laboratory* are further components of the VLTI. The delay lines are housed in a 168 m long tunnel underneath the platform, the *delay line tunnel*. The workshops

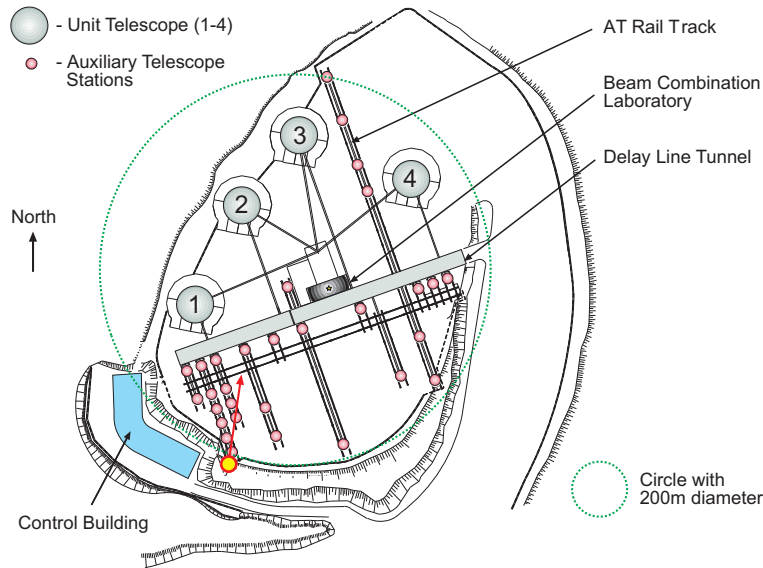


Figure 2.7: Layout of the VLTI and location of the individual telescope stations. The grey circles denote the locations of the four 8 m class unit telescopes (UTs). The auxiliary telescopes (ATs) can be located on any of the VLTI stations represented by the small red circles. The location, where the photo in figure 2.6 was taken, is marked by the yellow circle, its direction is indicated by the red arrow. (Image adapted from Glindemann *et al.*, 2000)

and the living facilities for personnel and astronomers are located at a few kilometers distance to the telescopes.

2.2.3 Path of the light

All current successful observations of AGN were carried out using the unit telescopes. In this case, the light is directed via the *Nasmyth focus* to the *Coudé room* which resides below the unit telescopes. Two adaptive optics correction units are located in this room in order to correct the aberrations of the incident wavefronts. A tip/tilt-system, the *System for Tip-tilt Removal with Avalanche Photodiodes* (STRAP, Bonaccini *et al.*, 2000), was installed at the start of VLTI operations. Since late 2004 also a higher order AO system called *Multi Application Curvature Adaptive Optics* (MACAO) is operational (Arsenault *et al.*, 2003). Both the MACAO and STRAP units use visible light extracted by a *dichroic beam splitter* and correct a field of view of 2 arcmin. MACAO and STRAP require an optical source less than 1 arcmin from the science target with $V < 17$ mag or $V < 16$ mag respectively. Although seeing effects are not as severe in the mid-infrared as in the near-infrared or optical, the AO systems guarantee diffraction limited images even for fair seeing conditions and ensure the stability of the source position in the beam. This is necessary for a good overlap of the images (see section 3.1.2).

From the Coudé room, the light is guided to the delay lines. The optical path difference is adjusted by retroreflector carriages on rails, the “Paranal metro”. The carriages are equipped with a reflector system, the so called *cat’s eye*, whose most important component is a *variable curvature mirror* (VCM) (Ferrari *et al.*, 2003). The curvature of these mirrors is adjusted depending on the length of the baseline in order to achieve an optimal reimaging of the pupil in

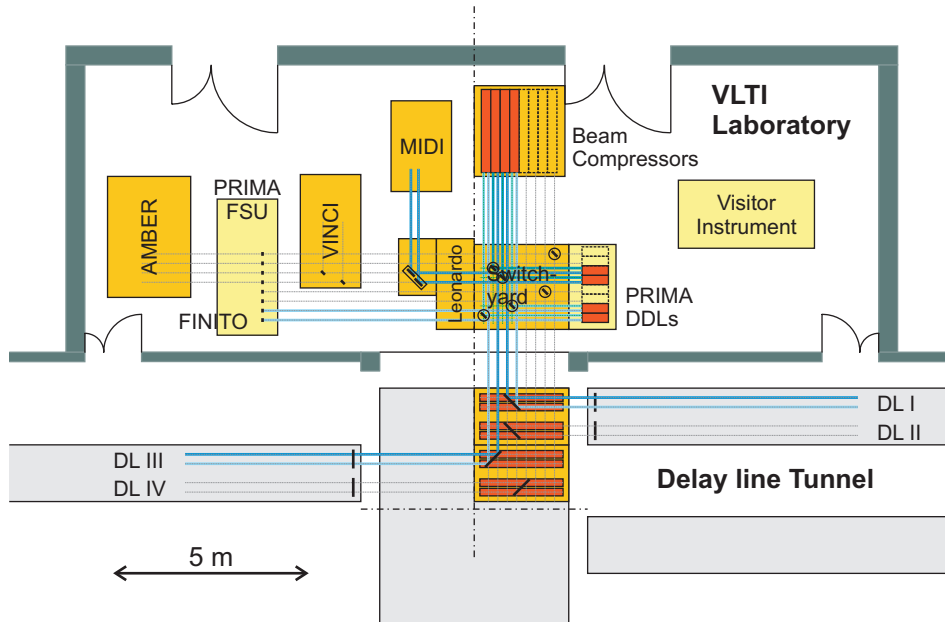


Figure 2.8: Layout of the interferometric laboratory. Coming from the delay lines, the light passes the switchyard where it is first redirected to the beam compressors (in the case of observations with the UTs) and then to the science instrument. The instruments shown are VINCI, MIDI and AMBER. (Image adapted from Glindemann *et al.*, 2003)

the interferometric lab. This allows to maximise the field of view available for interferometry and to minimise the thermal background coming from the VLTI optics. Currently, the VCMs are not adjusted for the UTs. After passing the delay lines, the light enters the interferometric laboratory where all interferometric instruments are located (figure 2.8). The light passes the so-called switchyard where it is first directed to the beam compressors. These compress the UT beams from a size of 80 mm to 18 mm in order to provide an equal beam diameter to the instruments for observations with the UTs (80 mm beams) and the ATs (18 mm beams). The light is finally directed to one of the interferometric instruments. The total number of mirrors the light has to pass before reaching the science instrument is 20. Due to the many reflexions, the throughput of the VLTI optics at $10\ \mu\text{m}$ is on the order of 15 % (Puech and Gitton, 2006)¹.

2.2.4 Interferometric instruments at the VLTI

A number of interferometric instruments are located in the VLTI laboratory. A list is given in table 2.1. VINCI, the *VLTI INterferometer Commissioning Instrument* (Kervella *et al.*, 2000, 2003), is intended for the commissioning of the VLTI infrastructure. Although it is not intended for scientific research, it has produced a number of scientific results, among them on the extragalactic source NGC 1068 (Wittkowski *et al.*, 2004). Since late 2005, VINCI has not been used any more. The *Astronomical Multi-BEam combineR* (AMBER) is the near-infrared instrument for the VLTI (Petrov *et al.*, 2007). So far, its sensitivity has not been sufficient to observe AGN: all attempts to record an interferometric signal of the brightest

¹It is interesting to note that in 2002 the transmission was $> 30\%$ (Koehler and Gitton, 2002). Since then, it has dropped due to aging of the optical elements and accumulation of dust on the optical surfaces.

Table 2.1: Table of (interferometric) instruments in the VLTI laboratory.

Name	Wavelength bands	R^a	Number of beams	First light	Purpose and characteristic
VINCI ^b	K band (2.0 – 2.4 μm)	none	2	03/2001	test instrument, fibres
MIDI	N band (8 – 13 μm)	230 and 30	2	12/2002	MIR instrument, ZnSe beam splitter
AMBER	J, H, and, K (1.0 – 2.4 μm)	12000, 1500, 30	2 or 3	04/2004	NIR instrument, single-mode fibres
FINITO	H band (1.5 – 1.8 μm)	none	3	07/2003	external fringe tracker, single-mode fibres
IRIS ^c	J or H or K	none	4	04/2005	delay line tip/tilt correction
PRIMA	J, H, K and N	none	2	planned	astrometry and phase reference

^aSpectral resolution.

^bCurrently not in use.

^cNo interferometric instrument. Low order adaptive optics system.

AGN, NGC 1068, have failed. This is due to vibrations in the VLTI infrastructure, which have a much greater impact in the near-infrared at $\lambda = 2 \mu\text{m}$ than in the mid-infrared at $\lambda = 10 \mu\text{m}$. The *Fringe-tracking Instrument of Nice and Torino* (FINITO) compensates for the atmospheric drifts in the OPD and hence increases the coherence time of the light sent to the science instruments MIDI and AMBER (Gai *et al.*, 2002, 2004). This leads to higher sensitivity due to longer integration times, especially in the near-infrared, that is, for AMBER. Due to technical problems, FINITO is still not fully operational. The *VLTI InfraRed Image Sensor* (IRIS) simultaneously measures the tilt of up to 4 beams in order to correct the image drift introduced inside the VLTI between the Coudé focus and the VLTI laboratory (Gitton *et al.*, 2004). It can be seen as a low order adaptive optics system. Finally, MIDI is the mid-infrared instrument for the VLTI.

2.3 The MIDI instrument

The *MID-infrared Interferometric instrument* (MIDI) is a two beam Michelson type interferometer producing dispersed fringes in the N band in a wavelength range from 8 to 13 μm (Leinert *et al.*, 2003). MIDI was built by a consortium of institutes from Germany, France and the Netherlands under the leadership of the *Max-Planck-Institut für Astronomie* (MPIA) in Heidelberg, Germany. The *principal investigator* (PI) of the instrument is Christoph Leinert. “First fringes” were obtained on 2002 Dec 15 and the instrument has been offered to the world wide community of astronomers since ESO’s Period 73², which started in April 2004. A picture of MIDI at its location in the VLTI laboratory is shown in figure 2.9; a sketch of the optical layout is given in figure 2.10.

MIDI is composed of two main parts, the *warm optical bench* and the *cold optical bench*.

The **warm optical bench** aligns the two incoming beams from the VLTI (designated *beam A* and *beam B* in the following) and adjusts the optical path difference using two small

²ESO divides its operations into semesters which consist of the months April to September and October to March. Period 73, for example, was from April to September 2004.

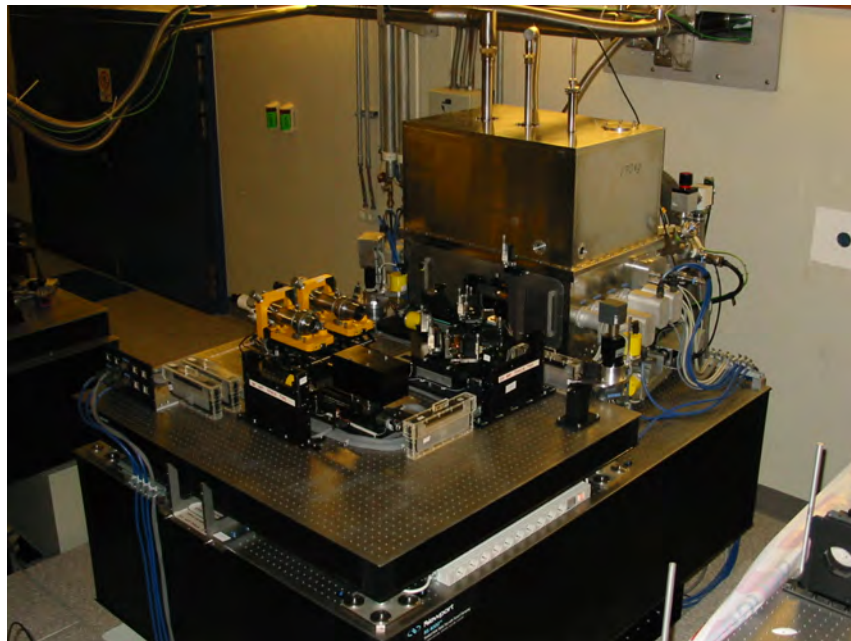


Figure 2.9: MIDI in the interferometric laboratory. Only the warm optical bench with the MIDI internal delay lines can be seen. The rest of the instrument is located inside the dewar at the far end of the optical table. (Image courtesy of ESO)

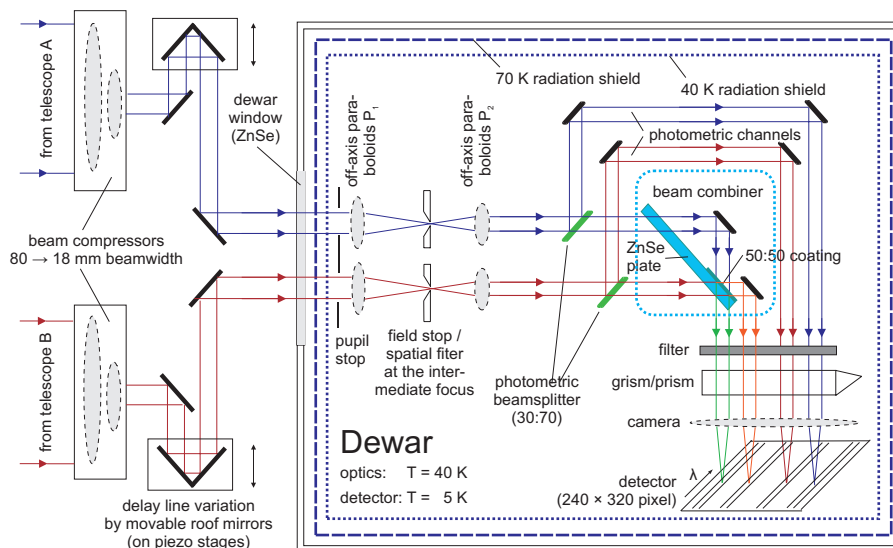


Figure 2.10: Sketch of the optical layout of MIDI. The light coming from the VLTI delay lines enters from the left. It passes the MIDI internal delay lines and enters the cold box. After reimaging, the light is combined in the beam combiner (turquoise) and then passes through a filter or a dispersive element in order to reach the detector. (Image courtesy of Uwe Graser, MPIA)

delay lines. These delay lines are realised by movable roof top mirrors. The mirrors of beam A are mounted on *piezo stages* which can be moved by $100\ \mu\text{m}$. Hence, the total possible change in optical delay is $200\ \mu\text{m}$. The optical delay of beam B can be changed by $100\ \text{mm}$ using an electric motor. In addition, the warm optical bench accommodates calibration and alignment equipment.

The **cold optical bench** is located in a *dewar*, in order to reduce the thermal background which is the major contributor of background at infrared wavelengths (see section 1.5). Inside the dewar, the optical components are cooled to $40\ \text{K}$ while the detector is cooled to an even lower temperature of $4\ \text{K}$. To allow the cooling, the dewar is evacuated to $10^{-7}\ \text{mbar}$. Although the cooling and the evacuation are indispensable, the associated equipment causes additional problems. The pumps and the closed cycle cooler introduce vibrations that can effect the measurement quality.

After entering the dewar through an entrance window made of ZnSe (zinc selenide), the two beams pass two stops, the *cold pupil* and the *field stop*. The two stops are designed to cut out the background and improve the image quality. Before sending the light to the beam combiner, it is possible to insert two beam splitters which divert 30% of the light of each beam. This diverted light is directly sent to the detector, where it produces the *photometric channels*. These channels can be used to calibrate the visibility and have the advantage that the total flux, that is, the photometry, of the source is measured simultaneously with the interferometric signal. This mode of observations is called *science-photometry* (SCI.PHOT) mode. The mode where the beam splitters are not inserted into the light path and the photometry has to be observed afterwards is called *high-sense* (HIGH.SENSE) mode, because more light is available for the interferometric signal.

The heart of the beam combiner is a ZnSe-plate, which is covered on the half of one side with a 50 : 50 coating. The two exiting light beams contain the interferometric signal. They have the opposite phase, that is, a phase shift of $\Delta\phi = \pi$ (*c.f.* equations 2.17 and 2.18). Each component of the exiting beams has travelled the same amount of times through the ZnSe-plate. In order to distinguish them from the incoming beams, from now on the two exiting beams will be called channels (*channel 1* and *channel 2*). After the beam combiner, filters or dispersive elements can be introduced into the light path. Two dispersive elements are available: a NaCl double prism, made of germanium and sodium chloride, provides a spectral resolution of $R = \lambda/\Delta\lambda = 30$, while a KRS5 grism made of thallium bromide provides a spectral resolution of $R = \lambda/\Delta\lambda = 230$. These elements allow to obtain the interferometric signal and the photometry dispersed, that is, as a spectrum. Finally, the light is focussed onto the detector by two different cameras. The *field camera* is used for imaging when no dispersive element is introduced into the light path, while the *spectral camera* is used for the dispersed signal. The detector is a Raytheon Si:As impurity band conduction device with 240×320 pixels and a quantum efficiency of 34% in the N band. The pixels have a physical size of $50\ \mu\text{m}$. The detector is read out in 16 channels leading to a pattern which can be seen in the raw data. The minimum integration time is $0.2\ \text{ms}$.

Chapter 3

Observations and data reduction

3.1 Observations

The entire interferometric set-up is a very complex system. It requires equally complex controlling to ensure that all components are working together in the optimal way. Fortunately, most of this complexity is hidden from the observer. Actually, it is surprisingly easy to perform observations with MIDI. The parameters for an observation are defined in a so-called *observation block* (OB). It contains all information an observer has to specify, for example the position of the target, the choice of filters, the instrument mode etc. The information in such an OB is substantiated by templates which contain all detailed information to control the various subsystems. The OB is then executed like a programme and using the templates it almost automatically initiates all necessary steps during the observation sequence. Changing settings of the instrument or telescopes apart from the ones allowed in the OB is normally not forseen.

In order to obtain a calibrated visibility point it is necessary, according to equation (2.38), to observe both the correlated flux I_{int} and the total photometry $I_{\text{tot}} = 4\sqrt{rt\eta_A\eta_B} \cdot I_{\text{src}}$ of the science target. In order to account for visibility losses in the instrument and to obtain absolute flux values (F_{cor} and F_{tot}), a calibrator star of known flux and size has to be observed in the same way as the science target. In the following, first the observational procedure with MIDI and then the data reduction will be discussed.

3.1.1 Preset

After pointing the two telescopes in the direction of the source, a star in the vicinity (within ~ 10 arcmin) of the target is automatically selected from a catalogue. The star is commonly referred to as the *guide star*. An arm in the Nasmyth focus of each telescope, the *guide probe*, picks up the light of this star, the *Nasmyth guide star*, and sends it to two technical detectors (TCCDs) via a dichroic beam splitter. One of the two sensors is used for the *acquisition, guiding and field stabilisation* (AGS), that is, it controls the tracking of the telescope. The second sensor is used for wavefront sensing, that is, for the *image analysis* needed for the active optics correction of the primary mirror. The light of the science target itself is fed into the Coudé and VLTI optical trains. In the Coudé room, the optical part of the light is diverted to the adaptive optics system, either to MACAO or to the STRAP unit (see section 2.2.3). The AO system uses the *Coudé guide star* for wavefront sensing. The Coudé guide star is different from the Nasmyth guide star and it has to be closer than 1 arcmin from the science source. During the preset, the delay lines are also set up by moving the retroreflector carriages to the expected position of 0 OPD. The entire preset procedure takes about 5 to 10

minutes, depending on the time the telescopes have to slew and on the quality of the source used for Coudé guiding.

3.1.2 Acquisition

The next step is to align the two images of the source so that they fall on top of each other on the beam combiner and on the detector inside MIDI. This is important, because otherwise the light cannot interfere and no interferometric fringes would be produced. The *field camera* is inserted into the light path and acquisition images are taken. To avoid saturation of the detector by the high background, exposures have a *detector integration time (DIT)* of typically 2 ms. To limit the amount of data, only two subarrays centred on the two beams, with a size of 62×69 pixels each, are read out. For the UTs, the subarrays have a pixel scale of 86 mas^1 and a field of view of 2 arcsec. All individual exposures are stored as frames of a data cube.

To suppress the background, the standard chopping technique is used: alternating, images of the object and of the sky are observed by tilting the secondary mirror. After subtracting the sky frames from the object frames, ideally, only the flux from the target remains. The default values for the *chopping frequency*, the *chopping angle* and *chopping throw* are $f_{\text{chop}} = 2 \text{ Hz}$, $\alpha_{\text{chop}} = 0^\circ$ and $\delta_{\text{chop}} = 15 \text{ arcsec}$ respectively. For AGN it is sensible to use the SiC filter ($\lambda_0 = 11.8 \mu\text{m}$) for the acquisition, because the spectra of these sources normally rise towards longer wavelengths. For the acquisition of calibrator stars, which are in the Rayleigh-Jeans part of their spectra, it is advisable to use the N8.7 filter at shorter wavelengths ($\lambda_0 = 8.6 \mu\text{m}$). The acquisition procedure is repeated until the overlap of the two beams is satisfactory, that is, until the beams are aligned with one pixel ($\lesssim 100 \text{ mas}$) accuracy. Examples of acquisition images after removal of the background by chopping are shown in figure 3.1. For weak targets, the number of individual exposures has to be increased significantly in order to make the source visible. Differential emission from the VLTI delay line tunnels (due to the lack of the variable curvature mirrors) leads to residuals after the background subtraction, which in turn make the detection of faint sources difficult (see also section 6.2). In figure 3.1, an unequal transmission of the light in beam A and B is visible: the source images in the left column appear fainter. This is caused by differences in the transmission of the light paths for the two telescopes as well as by the different efficiencies of the AO systems. Especially the AO system on UT2 (left column) falls behind the systems mounted on the other telescopes.

Since the advent of IRIS in late 2006, the acquisition procedure has changed. Now IRIS is used to align the two beams.

3.1.3 Fringe search

Once a good beam overlap is achieved, the beam combiner, a 0.52 arcsec wide slit and the prism or the grism are inserted into the light path. This leads to two spectrally dispersed interferograms of opposite phase, which are recorded by the detector. No chopping is needed during the interferometric measurements, as the background is uncorrelated and cancels out in the data reduction process (see section 3.2.3). Again only two subarrays on the detector with sizes of 171×41 pixels for the prism and 261×40 pixels for the grism are read out. The

¹This pixel scale was determined empirically by measuring the separation of the two components visible in the acquisition images of the source Mon R2 IRS 3. 14 different sets of acquisition images were used, which results in the value of $(86 \pm 5) \text{ mas pixel}^{-1}$.

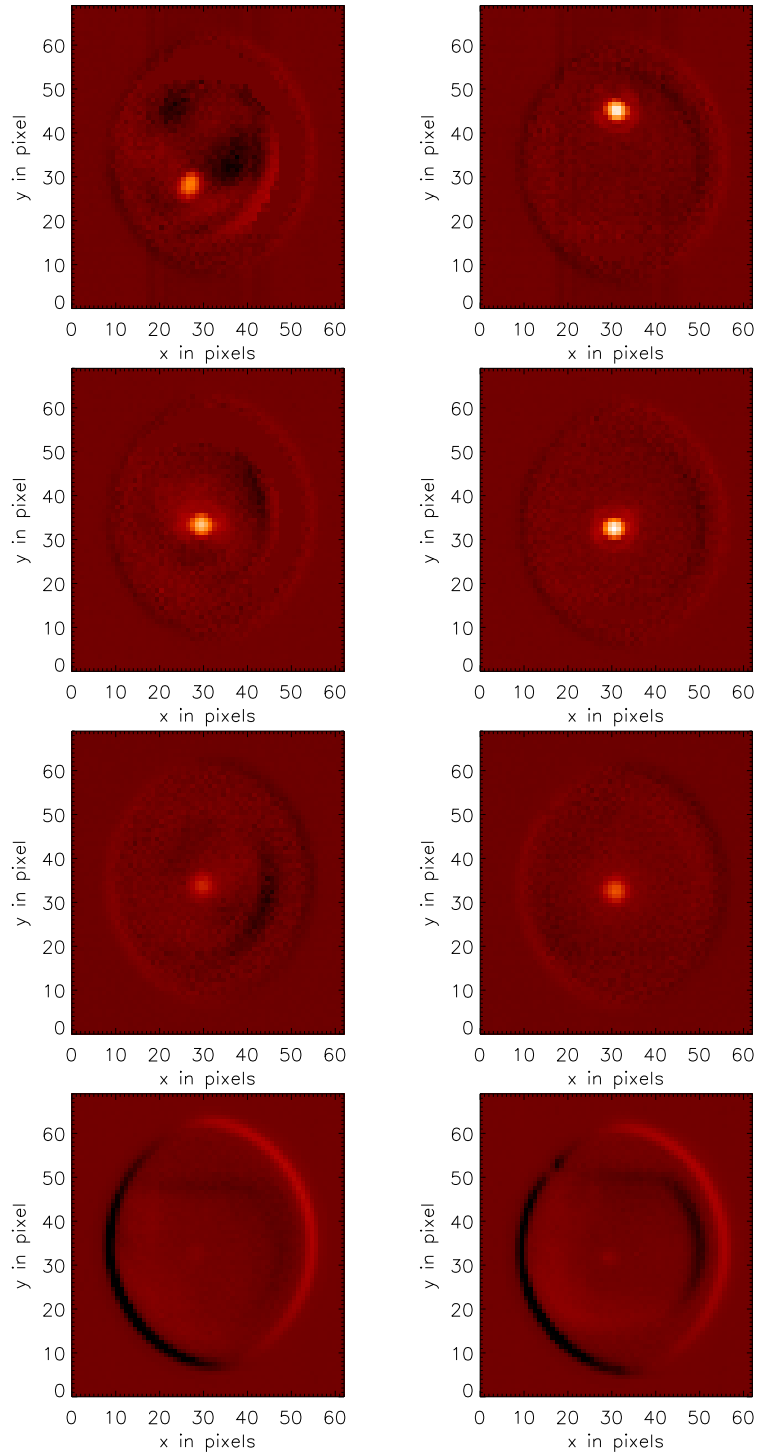


Figure 3.1: Acquisition images of MIDI. The images on the left are from beam A (in this case UT2) and the images on the right from beam B (UT3). Top row: first acquisition images for HD 120404 (flux $F \sim 10.0$ Jy, $NDIT = 1000$). Second row: final images for HD 120404 after recentering twice and before the start of the fringe search ($NDIT$ unchanged). Third row: final acquisition frames of Circinus ($F \sim 10.0$ Jy, $NDIT = 8000$). Bottom row: final acquisition of Mrk 1239 ($F \sim 0.6$ Jy, $NDIT = 12000$).

wavelength calibration takes the form

$$\lambda_{\text{prism}}(x) = -1.539 \times 10^{-4} \cdot (x + 120)^2 + 0.00949 \cdot (x + 120) + 15.4519, \quad (3.1)$$

$$\lambda_{\text{grism}}(x) = -1.211 \times 10^{-6} \cdot (x + 5)^2 - 0.023122 \cdot (x + 5) + 7.54423 \quad (3.2)$$

where x is the pixel position on the subarray and λ is in μm . Due to the dispersion of the light, the detector integration time can be higher than for the imaging: for prism normally $DIT = 18$ ms and for grism $DIT = 36$ ms. These values have, however, changed several times since MIDI became operational.

A fringe signal is searched by scanning the OPD over a few mm at the expected position. This position is determined from an empirical OPD model. The scan is achieved by moving the VLTI delay lines. At the same time, the piezo-driven mirrors of MIDI perform a sawtooth scanning pattern (with a scan length of normally $83.2 \mu\text{m}$ in 40 steps for the prism) to obtain a moving fringe pattern. In section 2.1.2 it was shown that for the prism ($R \sim 30$) the coherence length is ~ 0.3 mm. Depending on the strength of the source, fringes are indeed detected on such a range of OPD.

3.1.4 Fringe track

After the point of optical path equality is found, the so-called *fringe track* is started, during which the path difference is stabilised. Essentially, the correlated flux has already been measured during the fringe search, however, the signal-to-noise ratio is very low as only a few detector frames were recorded close to 0 OPD, where a strong fringe signal appears. To obtain a better signal, the measurement close to 0 OPD is repeated many times. By default 200 scans, each consisting of 40 frames, are performed. Using the scanning of the piezo driven mirrors, the *group delay* (see section 3.2.4) is constantly determined. The information is sent to the VLTI delay lines which compensate for siderial motion and atmospheric OPD shifts (Meisner, 2001). The behaviour of the instrumental OPD and the position of the zero delay are shown in figure 3.2 for a fringe track of the calibrator HD 120404. Figure 3.3 shows the individual detector frames during a single scan of the piezo stage. To make the fringes visible, the background had to be removed by subtracting the two channels from one another and by applying a temporal high pass filter (see section 3.2.3). Otherwise the detector signal would be totally dominated by the background.

There are two possibilities to track the fringes for MIDI: the scans can either pass over the white light fringe at 0 OPD (*white light tracking*) or they are performed next to it (*offset tracking*). At the beginning of a fringe track, the optical delay is changed by a large amount (typically 5 mm) for a few scans, so that no fringes are recorded. These scans are used to determine the background noise.

In the observing mode described here, MIDI is internally tracking the fringes (*internal fringe tracking*). So far, *external fringe tracking*, where another instrument, *e.g.* FINITO, determines the drift of the OPD, has not yet been offered by ESO.

3.1.5 Photometry

Finally, photometric data are recorded using only one telescope at a time for an otherwise identical optical set-up. This results into two photometric data sets, one for each telescope. Again, chopping has to be carried out to suppress the background in the mid-infrared. Similar problems as for the acquisition appear. By consequence, the photometry has large errors and it is the limiting factor for the accuracy of the visibility for faint targets.

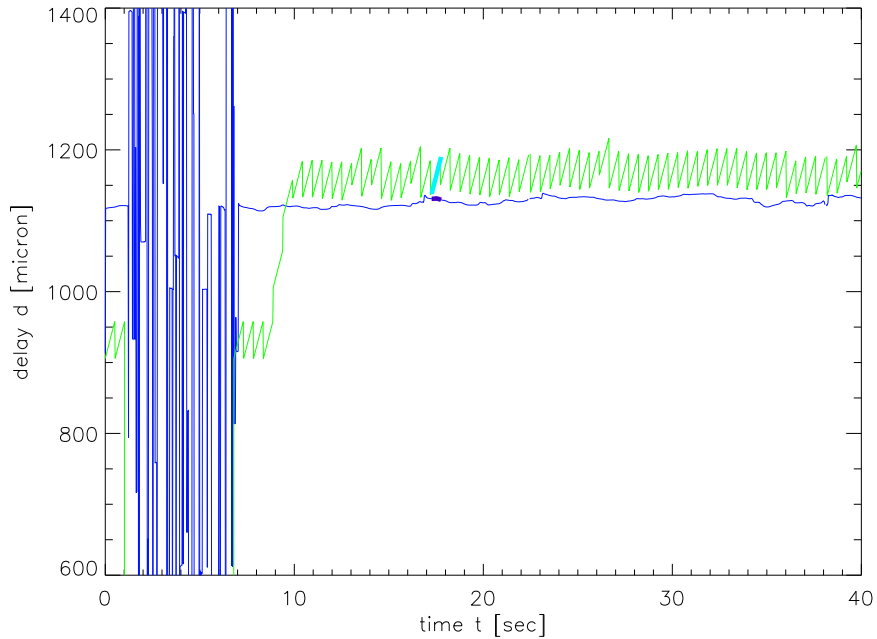


Figure 3.2: Instrumental delay (green) and group delay (blue) at the start of a fringe scan for offset fringe tracking of the calibrator HD 120404. Clearly the sawtooth pattern due to the scanning of the piezo mirrors is visible (stroke in this case $52\ \mu\text{m}$, sampled in 25 steps). At the beginning of the fringe track the instrumental delay is increased by a large amount to determine the background noise. During this time, the estimation of the group delay fails. The individual frames of the highlighted scan at $t = 17\text{ s}$ are shown in figure 3.3.

As a rule of thumb, the complete observation process from presetting the telescopes to the end of the photometric observations takes about half an hour. From this time, only 2 – 3 minutes are actually used for integrating on the fringe signal. Most of the time is used for the telescope set-up, for closing the loops of MACAO, for the alignment of the source images and for the fringe search. The archiving of the data can also consume a considerable amount of time. Additionally to the science target, the calibrator star has to be observed. The total time expenditure for one calibrated visibility point is hence on the order of one hour. For weak targets, the observations can take significantly longer, due to the difficulty to acquire the target and due to the necessary increase of the integration time (see also section 6.3).

Further details on the observational procedure can be found in the *MIDI User Manual* (Morel, 2007).

3.2 Data reduction

3.2.1 Properties of the MIDI data

All VLTI data is stored in the *OI Exchange Format*, better known under its moniker OIFITS (Ballester and Sabet, 2002; Pauls *et al.*, 2004, 2005). “OI” stands for “Optical Interferometry” and refers to interferometry in the visible and infrared (opposed to radio interferometry). The standard uses FITS binary tables to store the data. FITS, the *Flexible Image Transport System*, is the standard data format used in astronomy (Wells *et al.*, 1981; Hanisch *et al.*, 2001). Due to the many short exposures, the data amounts generated by MIDI are large.

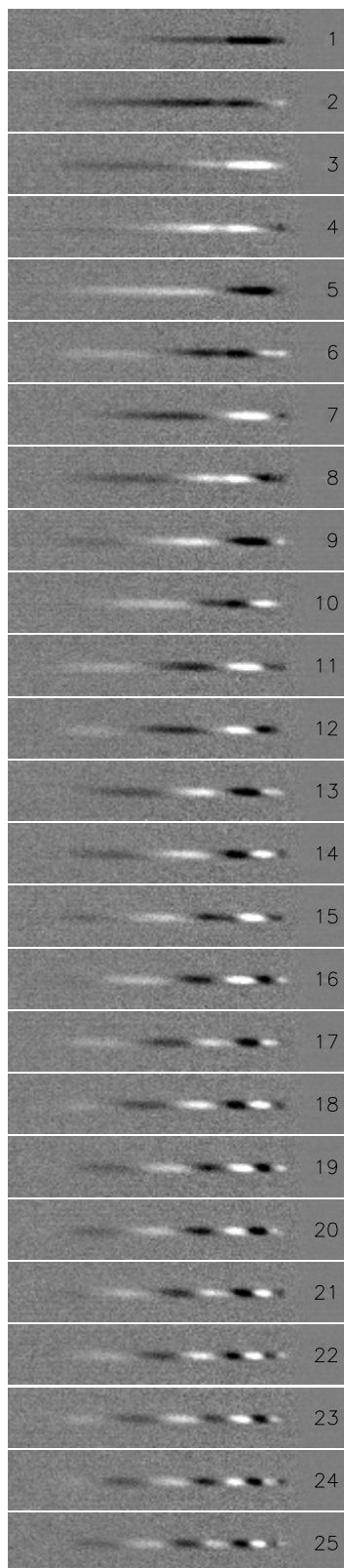


Figure 3.3: Fringe pattern on the detector during one fringe scan of HD 120404 at $t = 17$ s (see figure 3.2). The interferometric signal is dispersed in horizontal direction. The scan consists of 25 individual steps of the piezo, *i.e.* it is different from the normal scan length of 40 steps. For increasing optical delay (here in total by $52 \mu\text{m}$), more and more fringes appear in wavelength direction.

Depending on how efficiently the instrument works, as much as ~ 2 Gbyte of data are recorded in one hour. This leads to ramifications for data handling. For example, there is considerable dead time until the data is processed and archived after a longer exposure. Larger files are split into several 100 Mbyte files to ease data handling.

3.2.2 Data reduction packages

To reduce the data, two main programmes are available, the **Expert Work Station** (EWS) and the **MIDI Interactive Analysis** (MIA). Both programmes are distributed as a single programme package called “MIA+EWS”, which can be downloaded at <http://www.strw.leidenuniv.nl/~nevec/MIDI/> (Köhler, 2005). The package runs in the *Interactive Data Language* (IDL²), a commercial data visualisation and analysis platform. Most of the computationally intensive data processing is carried out by C routines.

MIA, which was written by Rainer Köhler, uses an incoherent method to determine the fringe amplitude, namely the *power spectrum analysis*. EWS on the other hand uses a coherent method (Jaffe, 2004). EWS was developed by Walter Jaffe and is derived from the software which is used by MIDI to find and track fringes (section 3.1.4). The reduction of the photometric data is almost identical in both pieces of software.

For completeness, other software packages capable of handling MIDI data are also listed here:

- The *Data Reduction Software* (DRS) or **Meudon package**³ was prepared at the Observatoire de Paris / LESIA by Quynh Nhu Nguyen.
- The **ESO pipeline**⁴ is used for ESO quality control and the generation of quick results during the observations (written by Jeffrey A. Meisner).
- Supposedly, there is also a “**Bonn package**” adapted from software developed at the MPIfR by Karl-Heinz Hofmann.

3.2.3 Compression

First, the two-dimensional signals $I_{i,\text{det}}(x, y)$ from every detector frame in the two channels $i = 1, 2$ are multiplied by two masks $M_i(x, y)$. The masks are centred on the spectrum of the source in the respective channel and act as spatial weighting functions. A more detailed discussion of the properties of the masks is deferred to section 3.2.7.

In the following step, the weighted detector signals are collapsed in the direction perpendicular to the dispersion direction:

$$I_i = \sum_{y=1}^{y_{\max}} I_{i,\text{det}}(x, y) \cdot M_i(x, y) \quad (3.3)$$

with $y_{\max} = 41$ for the prism and 40 for the grism. The one-dimensional signals I_i correspond to two opposite phased interferograms (*c.f.* equations 2.17, 2.18 and 2.37):

$$I_1 = S_1 + I_{\text{src}} \left[t\eta_A + r\eta_B + 2\sqrt{rt\eta_A\eta_B} \cdot V(B_\lambda) \cdot \sin(kd + \phi) \right] \quad (3.4)$$

$$I_2 = S_2 + I_{\text{src}} \left[r\eta_A + t\eta_B - 2\sqrt{rt\eta_A\eta_B} \cdot V(B_\lambda) \cdot \sin(kd + \phi) \right] \quad (3.5)$$

²ITT Visual Information Solutions formerly Research Systems Inc., Boulder CO

³http://www.mariotti.fr/data_processing_midi.htm

⁴http://www.eso.org/observing/dfo/quality/MIDI/pipeline/pipe_gen.html

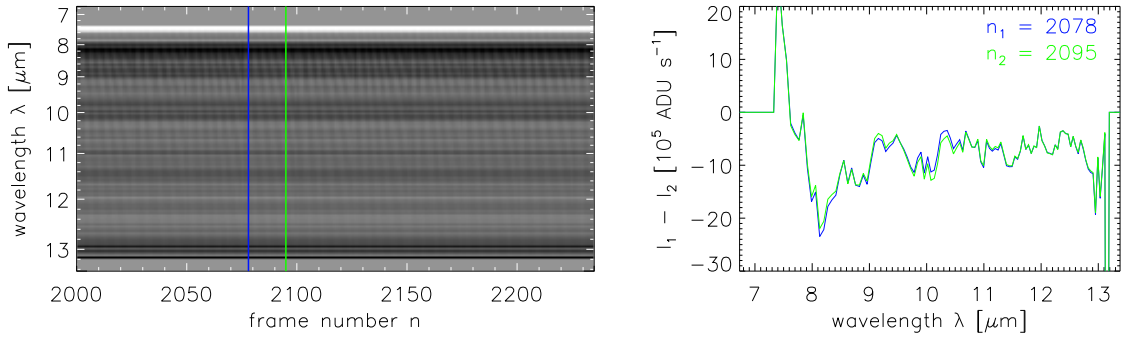


Figure 3.4: Interferometric data of HD 120404: Signal after compression and subtraction of the two channels from each other. Every column in the array on the left corresponds to the difference between the two compressed detector frames, that is, $I_1 - I_2$. The signal is still dominated by the residual background, which causes the horizontal stripes. The interferometric fringes appear as a faint, brush-like pattern. Cuts showing the signal for two different frames and hence OPDs are shown in the right panel of the figure. The corresponding frames are marked by vertical lines in the same colour in the left panel of the figure.

where $d = d_{\text{ins}} + d_{\text{atm}}$ is composed of the known instrumental delay $d_{\text{ins}} = d_A - d_B$ and the unknown atmospheric delay d_{atm} . S_1 and S_2 take into account the large background signal which is primarily due to the emission of the sky and of all warm optical elements. Note that $S_{1/2} \gg I_{\text{src}}$, so that the interferometric component normally is not visible in $I_{1/2}$.

As $S_1 \sim S_2$, $r \sim t$ and $\eta_A \sim \eta_B$, the two interferograms are subtracted from each other (*c.f.* equation 2.19) with the result of doubling the signal while removing a large part of the background:

$$\begin{aligned} I = I_1 - I_2 &= S_1 - S_2 + I_{\text{src}} \left[(t - r) (\eta_A - \eta_B) + 4\sqrt{rt\eta_A\eta_B} \cdot V(B_\lambda) \cdot \sin(kd + \phi) \right] \quad (3.6) \\ &= I_{\text{resid}} + 2f I_{\text{src}} \cdot V(B_\lambda) \cdot \sin(kd + \phi). \quad (3.7) \end{aligned}$$

where we have set $I_{\text{resid}} = S_1 - S_2 + I_{\text{src}} (t - r) (\eta_A - \eta_B)$, the residual background, and $f = 2\sqrt{rt\eta_A\eta_B}$, a factor correcting for inequalities in the beams. The one-dimensional fringes are arranged in an array with the frame number in one direction and the wavelength in the other. This is shown in figure 3.4 for the fringe track of the calibrator HD 120404 (same observation as in figure 3.2).

The fringes vary rapidly in time due to the modulation of the instrumental delay d_{inst} using the MIDI internal mirrors. For this reason, a boxcar smoothing in temporal direction, *i.e.* in direction of the frame number, is performed (in EWS only). This high pass filter removes the residual background which only changes slowly in time. The width of the boxcar is governed by the parameter `smooth`. The default value is `smooth = 50`, that is, the boxcar has a width of 50 frames or ~ 1 s for a detector integration time of 18 ms. This is acceptable for stable atmospheric conditions and strong sources, but a smaller value is advisable for a variable background and weak sources. To further suppress I_{resid} , the average of the entire spectrum can be subtracted from every frame using the keyword `dave`. This assumes a modulation of the fringe signal in frequency (or wavelength) space, which is indeed the case when the OPD is non-zero (*e.g.* for data obtained in offset tracking mode).

What remains after these operations is the interferometric signal (*c.f.* equation 2.37):

$$I_{\text{int}} = 2f I_{\text{src}} \cdot V(B_\lambda) \cdot \sin(kd + \phi). \quad (3.8)$$

The result is shown in figure 3.5.

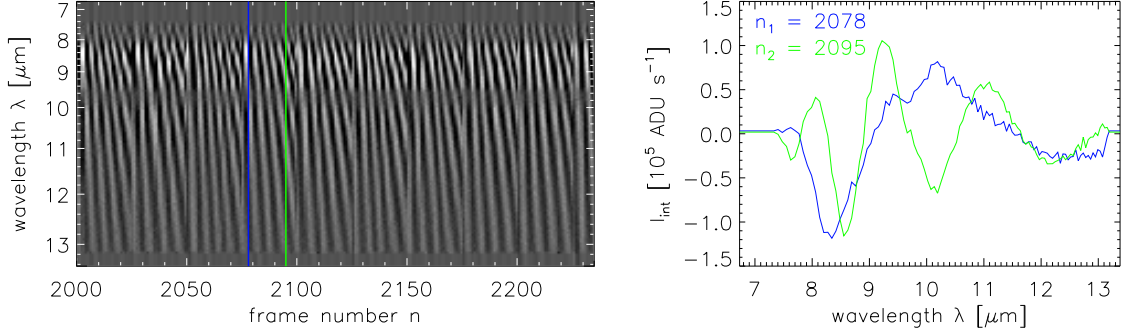


Figure 3.5: Fringes of HD 120404: Interferometric signal after compression, high pass filtering in direction of frame numbers and removal of the average in wavelength direction. The brush-like pattern comes from the modulation of the OPD with a sawtooth pattern repeating every 25 frames in offset fringe tracking mode. Two cuts showing the fringes for two different frames are shown in the right part of the figure.

3.2.4 Coherent reduction

Group delay analysis

In the following step, the known instrumental OPD, d_{ins} , is removed by multiplying each frame by $\exp(-ikd_{\text{ins}})$:

$$I_{\text{rot1}} = I_{\text{int}} \cdot e^{ikd_{\text{ins}}} \quad (3.9)$$

$$= f I_{\text{src}} \cdot V(B_\lambda) \cdot \frac{1}{i} \left(e^{ikd_{\text{atm}} + i\phi} - e^{-ik(d_{\text{atm}} + 2d_{\text{ins}}) - i\phi} \right). \quad (3.10)$$

I_{rot1} now is complex data. Each frame is then Fourier transformed from the frequency domain to the delay domain:

$$F(d') = \int I_{\text{rot1}} \cdot e^{-ikd'} dk. \quad (3.11)$$

$F(d')$ is called the *delay function*. For an infinitely broad band and constant visibility (that is, f , I_{src} , and V do not depend on k), it is easy to calculate the integral so that

$$F(d') = f I_{\text{src}} \cdot V(B_\lambda) \cdot \frac{1}{i} \left(\delta(d_{\text{atm}} - d') e^{i\phi} - \delta(d_{\text{atm}} + 2d_{\text{ins}} + d') e^{-i\phi} \right) \quad (3.12)$$

In reality, the peaks will be broader and the shape will depend on the form of $f(k)I_{\text{src}}(k)V(k)$:

$$F(d') = \frac{1}{i} \mathcal{F}[f(k) \cdot I_{\text{src}}(k) \cdot V(k)](d') \cdot \left((d_{\text{atm}} - d') e^{i\phi} - (d_{\text{atm}} + 2d_{\text{ins}} + d') e^{-i\phi} \right). \quad (3.13)$$

The absolute value of the delay function, $|F(d')|$, is shown in figure 3.6. The result are two peaks which correspond to the *group delay* (Lawson, 2000a; Meisner, 2001). One of them only moves very slowly due to changes in the optical delay d_{atm} . The other peak oscillates rapidly due to the modulation of the instrumental delay with the piezo mirrors. Smoothing in time direction will suppress the peak moving with $2d_{\text{ins}}$, while the other peak will remain. The smoothing is performed with a Gaussian kernel with a sigma set by the parameter `gsmooth`. The parameter has a default value of `gsmooth = 4`. For weak sources and stable atmospheric conditions, a higher value is advisable. The position of the remaining peak corresponds to the atmospheric delay d_{atm} .

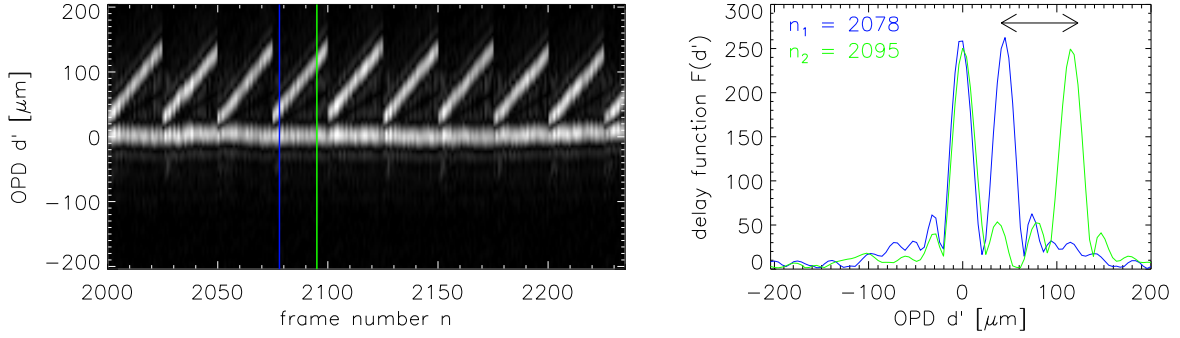


Figure 3.6: Delay function of the fringe packets. The movement of one of the peaks can be seen clearly, while the other peak remains more or less stationary. The form of the peaks is determined by the Fourier transform of the fringe amplitude. In this case, it resembles a sinc function due to the finite band width of the N band.

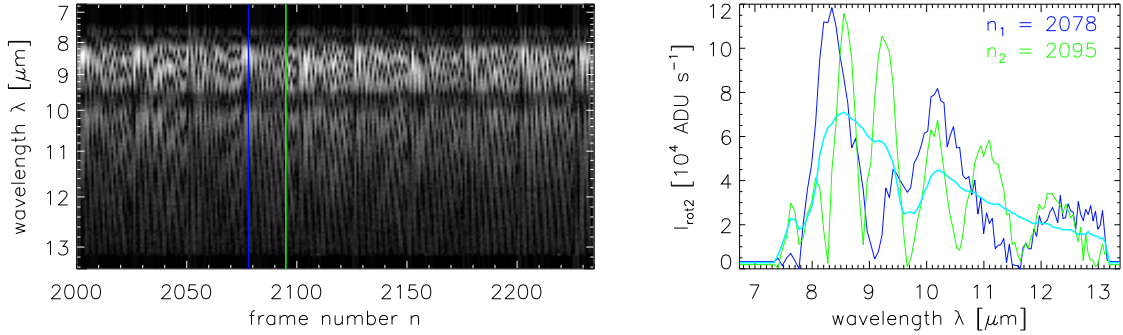


Figure 3.7: Absolute value of the fringe spectra after removal of instrumental and atmospheric delay as well as of the constant phase shift by refraction of water vapour. Averaging in time direction produces the final correlated flux (turquoise).

Alignment of fringes

With this information, both the instrumental and the atmospheric delay can be removed from (3.8):

$$I_{\text{rot2}} = I_{\text{int}} \cdot e^{ik(d_{\text{ins}}+d_{\text{atm}})} \quad (3.14)$$

$$= f I_{\text{src}} \cdot V(B_{\lambda}) \cdot \frac{1}{i} \left(e^{i\phi} - e^{-i2k(d_{\text{atm}}+d_{\text{ins}})-i\phi} \right). \quad (3.15)$$

Additionally, a linear phase shift induced by the varying index of refraction of water vapour, $\phi_{\text{H}_2\text{O}} = a \cdot \lambda + b$, is estimated and also removed. The result is shown in figure 3.7. After rejecting frames with too large optical path differences (*e.g.* $d > 150 \mu\text{m}$) or large jumps in the OPD, the remaining data is averaged coherently making use of the time dependency of $d_{\text{atm}}(t)$ and $d_{\text{ins}}(t)$:

$$I_{\text{coh}} = \int f I_{\text{src}} \cdot V(B_{\lambda}) \cdot \left(e^{i\phi_{\text{diff}}} - e^{-i2k(d_{\text{atm}}+d_{\text{ins}})-i2\phi_{\text{H}_2\text{O}}-i\phi_{\text{diff}}} \right) dt \quad (3.16)$$

$$= f I_{\text{src}} \cdot V(B_{\lambda}) \cdot e^{i\phi_{\text{diff}}} \quad (3.17)$$

$$= I_{\text{cor}}(B_{\lambda}) \cdot e^{i\phi_{\text{diff}}} \quad (3.18)$$

From this coherent signal, the raw correlated flux,

$$I_{\text{cor}} = f I_{\text{src}} \cdot V, \quad (3.19)$$

and the differential phase ϕ_{diff} can be extracted. To obtain the (normalised) visibility $V(B_\lambda)$, the total intensity of the source, $f I_{\text{src}}$, has to be determined (see section 3.2.6).

3.2.5 Incoherent reduction

The incoherent data reduction also starts from the interferometric signal given in (3.8). Each fringe scan is Fourier transformed from the delay space to the frequency space:

$$F(k') = \int I_{\text{int}}(d) e^{-ik'd} dd \quad (3.20)$$

$$= \frac{1}{i} f(k) I_{\text{src}} \cdot V(B_\lambda) \cdot [\delta(k - k') e^{i\phi} - \delta(k + k') e^{-i\phi}]. \quad (3.21)$$

The power spectrum is then defined as

$$P(k') = |F(k')|^2 = f(k) I_{\text{src}} \cdot V(B_\lambda) \cdot [\delta(k - k') - \delta(k + k')]. \quad (3.22)$$

It has two peaks at the frequencies $\pm k'$. The wavelengths present in the band and the rate at which the OPD changes define the form and the position of the peak. With this information, the power inside the correct frequency interval, taking into account possible drifts of the OPD due to the atmosphere, is integrated. This then corresponds to the raw correlated flux $I_{\text{cor}} = f(k) I_{\text{src}} \cdot V(B_\lambda)$. A correction for noise is applied. For this reason, the OPD was offset at the beginning of the fringe scan. Note that using the power spectrum method no phase information can be extracted at all. A detailed description of the incoherent data reduction is found in Ratzka (2005).

3.2.6 Photometry

To determine the raw total flux of the target, first the standard data reduction methods for chopped data are applied to the photometric data: the average of the sky frames is subtracted from the average of the object frames. The result can be seen in the lower part of figure 3.8. As for faint sources the chopping does not lead to a satisfactory sky subtraction, two stripes on the detector frame, one above the target position and one below, are used to subtract an additional wavelength dependent sky estimate. The stripes consist of the rows 7 – 11 and 23 – 27 for the prism (*i.e.* from 0.52 arcsec to 0.86 arcsec above and below the spectrum centre) and of the rows 4 – 8 and 27 – 31 for the grism (*i.e.* from 0.82 arcsec to 1.16 arcsec above and below the spectrum centre). The position of these stripes can be adjusted by using the option `dsky`, which moves the stripes inward (`dsky` negative) or outward (`dsky` positive) by the amount of pixels specified. After applying the same mask as for the interferometric data (section 3.2.3), the frames are then compressed and averaged to a one-dimensional photometry, one for every telescope A, B and side of the beam splitter 1, 2:

$$I_{A1} = t\eta_A I_{\text{src}}, \quad (3.23)$$

$$I_{A2} = r\eta_A I_{\text{src}}, \quad (3.24)$$

$$I_{B1} = r\eta_B I_{\text{src}}, \quad (3.25)$$

$$I_{B2} = t\eta_B I_{\text{src}}. \quad (3.26)$$

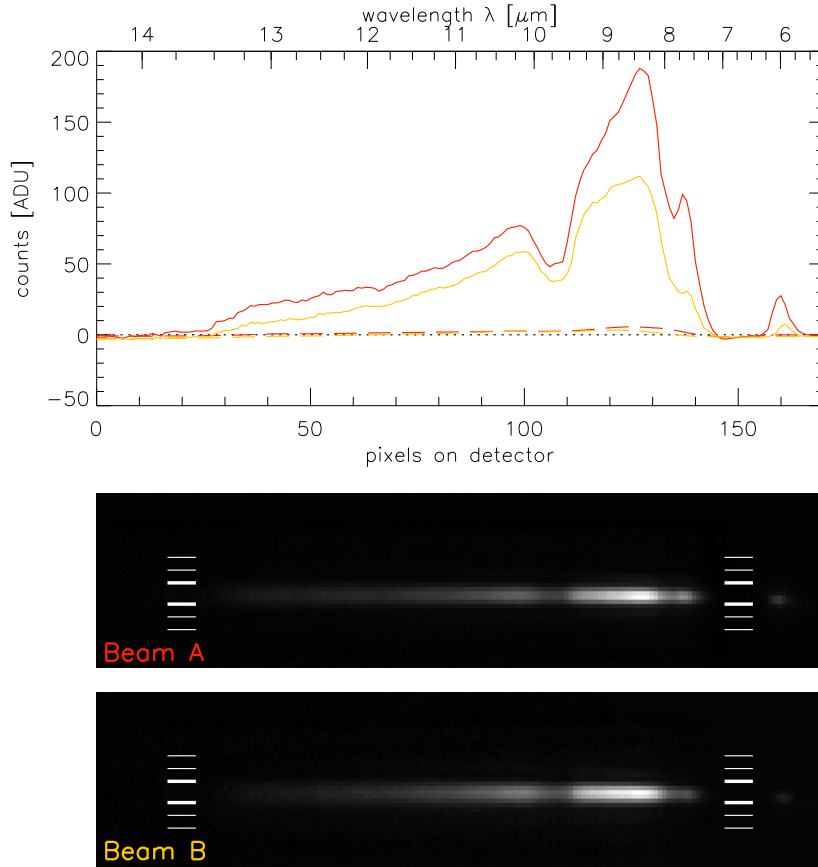


Figure 3.8: Photometry of a calibrator (HD 112213). The plot shows the integrated flux in a boxcar mask (marked by two thick lines on the detector frames, below) from telescope A (red) and telescope B (orange). The flux level determined in two extra sky bands above and below the object (thin lines on the detector frames) are shown as dashed lines. Note that the wavelength increases to the left.

Examples for I_{A1} and I_{B1} using a boxcar mask are shown in the upper part of figure 3.8. Clearly, the different telescope responses η_A and η_B can be seen. The Rayleigh-Jeans spectrum of the calibrator is filtered by atmospheric absorption (*c.f.* figure 1.4). The ozone absorption feature between 9.5 and 10.0 μm is clearly visible. The small bump at 6.0 μm results from a small, semi-transparent window of the atmosphere.

Two sets of total fluxes are extracted: One is needed for the determination of the visibility, and hence the same mask as for the interferometric data is applied. To account for the possible inequality of the two beams from the two telescopes, this total flux is calculated as the geometric mean:

$$I_{\text{geo}} = \sqrt{I_{A1} \cdot I_{B1}} + \sqrt{I_{A2} \cdot I_{B2}} \quad (3.27)$$

$$= 2\sqrt{rt\eta_A\eta_B} \cdot I_{\text{src}} \quad (3.28)$$

$$= f I_{\text{src}} \quad (3.29)$$

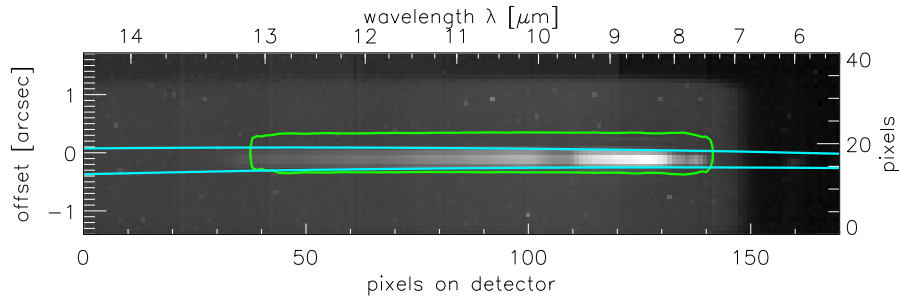


Figure 3.9: Standard deviation of the signal of the fringe track for HD 120404 dispersed by the prism. The position of the signal is clearly visible. The contours of half transmission of the masks are overplotted: the fixed mask from EWS is plotted in green and the fitted mask from MIA is plotted in cyan.

The second total flux is determined without applying a mask and by taking the arithmetic mean of the individual measurements:

$$I_{\text{arit}} = \frac{1}{2} (I_{A1} + I_{A2} + I_{B1} + I_{B2}) \quad (3.30)$$

$$= \frac{1}{2} (r + t) (\eta_A + \eta_B) \cdot I_{\text{src}} \quad (3.31)$$

$$\approx I_{\text{src}} \quad (3.32)$$

where the last approximation holds for $\eta_A \approx \eta_B \approx 1$ and $r \approx t \approx 0.5$. Combining (3.19) and (3.29) one obtains the raw visibility

$$V_{\text{raw}} = I_{\text{cor}}/I_{\text{geo}}. \quad (3.33)$$

3.2.7 Masks

For the determination of the correlated flux and the visibility, masks are used to suppress the noise signal on the detector frames above and below the spectrum. EWS uses fixed masks. It has a built-in library of masks for all different observing modes. The relevant mask is then used for all observations obtained in a certain mode. The mask for observations with the prism in high-sense mode has a width at half maximum of 8.6 pixels which corresponds to 0.74 arcsec. While EWS relies on a set of fixed masks, MIA uses interactively created masks. These are determined by fitting a Gaussian distribution perpendicular to the spectral dispersion direction (that is the y -direction) for every wavelength bin. The centre and width of the Gaussian distribution are then fitted by second order polynomials in dispersion direction in order to create a smooth mask. For the fitting, the photometric data is used and separate masks for the calibrator and the science target are determined. A comparison of the two masks for a calibrator star observed in high-sense mode with the prism can be found in figures 3.9 and 3.10. Fitting the mask individually for each object has the following two advantages: shifts in the position of the object are automatically taken care of and the width of the mask is adjusted to that of the PSF. Such a mask is hence very well adapted to the specific data. This can be clearly seen in the two figures: The mask determined from the interactive fit is only a little wider than the PSF from the calibrator. The fixed mask from EWS is not well centred on the object and it is much broader than the PSF. The adaptation of the mask position can also cause problems, for example when the position of the source changes slightly between the photometry and the fringe track. In this case, a broader mask

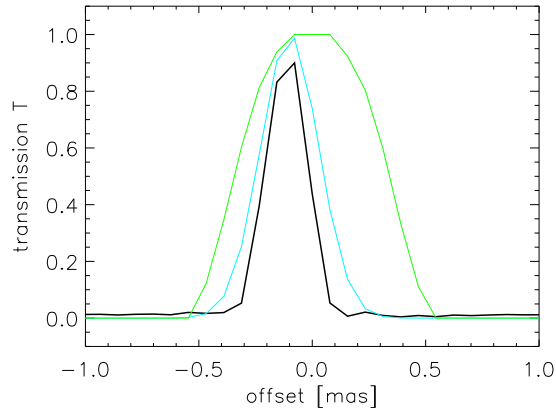


Figure 3.10: Cut across the mask and signal shown in figure 3.9. The signal is plotted in black, the fixed mask from EWS in green and the fitted mask from MIA in cyan.

is more reliable, as it still includes all the flux even after a small change of the position of the source. For an unknown reason, the masks for the prism in high-sense mode in EWS are truncated outside $\lambda < 7.5 \mu\text{m}$ and $\lambda < 13.1 \mu\text{m}$. This is unfortunate, as the N band is still transparent to some degree in these border regions (*c.f.* figures 1.4 and 3.8). In future updates of the software package, this constriction should be removed. A fixed mask is, however, not all that bad: For very faint sources, the signal is too weak to directly fit a mask to the data. In this case, the user can either manually adjust the parameters to find an “optimal solution” or a fixed mask is used. The first option is always prone to introduce biases.

The discussion whether fixed or fitted masks are of advantage is a complex issue. The reciprocal effects of the position of the source image on the detector must be considered for both the photometry and the fringe track for the science target as well as for the calibrator star. There is no final answer to the discussion – that is why the two options are actually available. For the data reduction of AGN, only fixed masks were used and this for three reasons: (i) simply for the reason that EWS natively uses fixed masks, (ii) because many of the AGN are so faint, that fitting a mask is problematic or even impossible and (iii) experimenting with fitting masks has shown that changing the mask parameters can have a significant impact on the result. We tried to avoid being tempted to do so.

3.3 Calibration

The same data reduction is applied to both the science object (index “obj”) and to the calibrator star (index “cal”) leading to the raw correlated flux (in ADU) $I_{\text{obj,cor}}$ and $I_{\text{cal,cor}}$ respectively, as well as to the raw total fluxes $I_{\text{obj,geo}}$, $I_{\text{obj,arit}}$, $I_{\text{cal,geo}}$, $I_{\text{cal,arit}}$ and to the raw visibilities V_{obj} and V_{cal} .

Finally, the raw fluxes and visibilities of the science target are calibrated using the data of a calibrator star, to account for instrumental visibility losses and to determine the absolute flux values. For this, the flux and the size of the calibrator must be known. Typically, calibrator sizes are $\sim 3 \text{ mas}$, so – to a first order – the calibrator can be assumed to be unresolved. If the diameter of the calibrator is known, the decrease of the visibility and the correlated flux can be taken into account, *e.g.* by assuming the star to be a uniform disk (see section 2.1.4). This correction is implemented in EWS: the diameter can be specified by the parameter `diam`. The

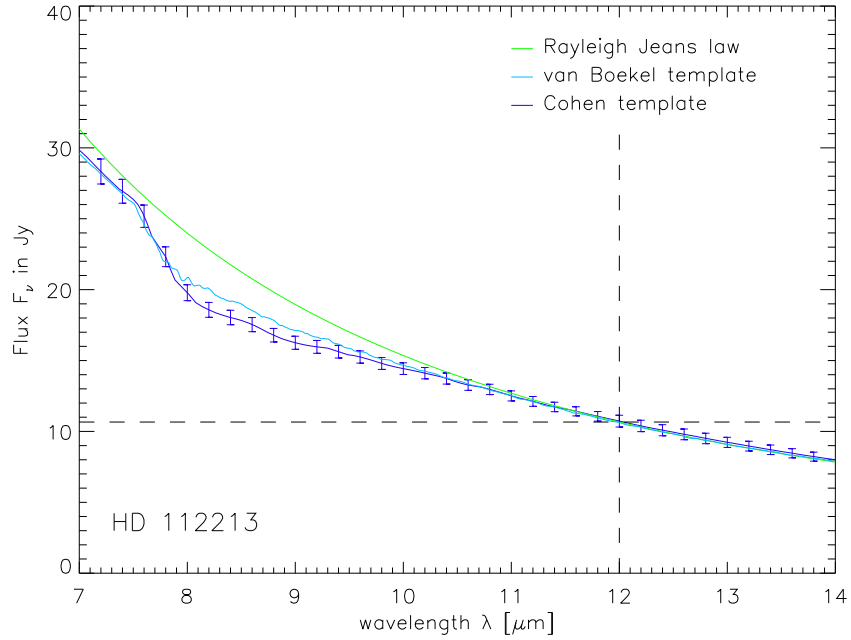


Figure 3.11: Comparison of three different approximations of the mid-infrared spectrum of the calibrator star HD 112213: Rayleigh-Jeans law (green), template spectrum provided by Roy van Boekel and template spectrum from Cohen *et al.* (1999).

spectral dependency of the flux can be approximated by the Rayleigh-Jeans law, scaled by a photometric point, *e.g.* the IRAS 12 μm flux. More accurately, a template spectrum (F_{cal}) can be used. Two template databases are considered here: templates from Cohen *et al.* (1999) and a database provided by Roy van Boekel, (*private comm.*). The latter template spectra were obtained by fitting stellar templates to multiband photometry. A comparison between the three templates for the calibrator HD 112213, namely the Rayleigh-Jeans approximation, the Cohen template and the van Boekel template can be found in figure 3.11.

To keep the influence of the photometry as small as possible, the calibrated correlated flux of the science object can be calculated according to

$$F_{\text{cor}}(\lambda) = I_{\text{obj,cor}}/I_{\text{cal,cor}} \cdot F_{\text{cal}} \quad (3.34)$$

using the option `nophot = 1` in EWS. This *direct calibration* for the correlated flux does not contain any photometric measurements. The calibrated total flux is given by

$$F_{\text{tot}}(\lambda) = I_{\text{obj,arit}}/I_{\text{cal,arit}} \cdot F_{\text{cal}} \quad (3.35)$$

and the calibrated visibility by

$$V(\lambda) = V_{\text{obj}}/V_{\text{cal}} = \frac{I_{\text{obj,cor}}}{I_{\text{obj,geo}}} \cdot \frac{I_{\text{cal,geo}}}{I_{\text{cal,cor}}}. \quad (3.36)$$

Note that in this case

$$V(\lambda) = F_{\text{cor}}(\lambda)/F_{\text{tot}}(\lambda) \quad (3.37)$$

only if

$$r = \frac{I_{\text{obj,arit}}}{I_{\text{obj,geo}}} \cdot \frac{I_{\text{cal,geo}}}{I_{\text{cal,arit}}} \equiv 1. \quad (3.38)$$

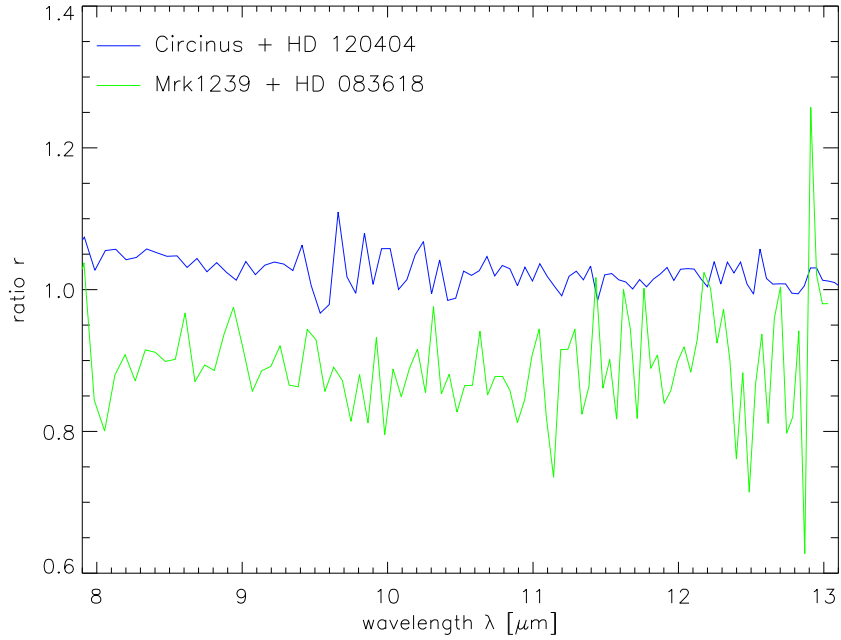


Figure 3.12: Example for the wavelength dependency of the ratio r for two source-calibrator combinations.

An example for the wavelength dependency of this ratio r is shown in figure 3.12. Alternatively (`nophot = 0`, default setting), the correlated flux can be determined as

$$F_{\text{cor}}^*(\lambda) = V(\lambda) \cdot F_{\text{tot}}(\lambda) = r \cdot F_{\text{cor}}(\lambda) \quad (3.39)$$

in order to fulfill the standard definition of the visibility (3.37). This *standard calibration* has the advantage of being less sensitive to atmospheric variations, changes in the image quality and pointing differences between the observation of the object and the calibrator. On the other hand, the fluxes from the science target and the calibrator enter twice. Especially for faint sources, the photometry has much larger errors than the correlated flux, which can lead to exaggerated error estimates for the correlated flux when using the standard calibration. For extended sources, the standard calibration will lead to a slight overestimate of the correlated flux, because light scattered into the masked area for the science target will lead to a lower $I_{\text{obj,geo}}$ and hence $r > 1$. It is thus to some degree related to the choice of the masks. Using the direct calibration, the correlated flux can be determined even if the photometry was not measured at all. The source 3C 273 discussed in chapter 6 is such an example.

There is no final answer to this “calibration issue”. In the end, the decision is reduced to the question whether the photometry of the science target, observed a few minutes after the fringe track, is more trustworthy than the fringe track of the calibrator which is normally observed half an hour after the science target and whether the source was correctly positioned inside the mask. Considering the low quality of the photometry and the frequent absence of an independent photometry measurement in the AGN data, the direct calibration of the correlated flux was used for all the data.

3.4 Error estimates

The determination of reliable errors for the final quantities of the data reduction is still an unsolved issue. For this reason, only a short overview of the problem will be given here. MIA does not produce any error estimates at all⁵. In this case, the only way to obtain any idea about the errors is to calibrate the science target with several calibrator stars and then to look at the scatter of the results. Ultimately, this means to look at the scatter of the calibrator data for which the fluxes and the visibility are known. This method requires that several calibrators were observed in the same instrument mode. The errors are also difficult to interpret if the calibrators were observed at different air masses or if the atmospheric conditions were not stable.

EWS uses a different approach. The quantities determined by the data reduction are derived from a large number of individual frames, normally on the order of a few thousand. EWS makes use of this to determine its error estimates. The original fringe track and photometry data is divided into 5 independent subsets from which the directly measured quantities I_{cor} , I_{geo} and I_{arith} are determined individually. The five values are then used to obtain their *root mean square deviation*. For the quantities derived later in the data reduction process, the errors are then propagated through the calculation. It is also obvious that these errors are only mere estimates and have to be considered with caution. They cannot be regarded as absolute errors, as systematic errors are not taken into account. These are most likely on the order of 5 – 15 %, as usually the case for observations in the mid-infrared. In this respect, especially the errors of the correlated fluxes seem to be rather underestimated, a fact which caused some headache when fitting the MIDI data of Circinus.

Because we almost exclusively used EWS for our data reduction, these errors are plotted in the figures in this thesis. They should be considered only as indicative values and not taken at face value.

⁵In the latest version of the software, an error of the correlated flux is calculated, although this is – according to Rainer Köhler, the author of the software – “undocumented, untested and impossible”.

Chapter 4

The dusty torus in the Circinus galaxy¹

4.1 Introduction

The Circinus galaxy (see figure 4.1) is a highly inclined ($\sim 65^\circ$) SA(s)b galaxy harbouring a Seyfert type 2 active nucleus as well as a nuclear starburst. At about 4 Mpc distance (1 arcsec \sim 20 pc, Freeman *et al.* 1977), the galaxy is among the nearest AGN and hence it is an ideal object to study the nuclear region of active galaxies. The nucleus is heavily obscured by dust lanes in the plane of the galaxy, so that it is best observed in the infrared. The galaxy can be considered a prototype Seyfert 2 object due to the presence of narrow emission lines (Oliva *et al.*, 1994), broad emission lines in polarised light (Oliva *et al.*, 1998), an ionisation cone traced by [O III], H α and [Si VII] (Veilleux and Bland-Hawthorn, 1997; Maiolino *et al.*, 2000; Wilson *et al.*, 2000; Prieto *et al.*, 2004), an outflow observed in CO (Curran *et al.*, 1998, 1999), bipolar radio lobes (Elmoultie *et al.*, 1998) and a Compton reflection component in X-rays (Matt *et al.*, 1996; Smith and Wilson, 2001). The ionisation cone, the outflow and the radio lobes have a position angle of about -40° , which is roughly perpendicular to the disk of the galaxy, to the circum-nuclear star forming rings and to the nuclear rings of molecular gas. Greenhill *et al.* (2003) have found an edge-on, warped accretion disk with a radius of $r_{\text{outer}} \sim 0.40$ pc which is traced by H₂O masers. The almost Keplerian velocity curve limits the mass of the central black hole to $M_{\text{BH}} < (1.7 \pm 0.3) \cdot 10^6 M_\odot$.

Modelling the SED of the nucleus of the Circinus galaxy was attempted by Siebenmorgen *et al.* (1997), Ruiz *et al.* (2001) and Schartmann *et al.* (2005). The latter two came to the conclusion that the presumed toroidal dust distribution is relatively small, with an effective emission region in the MIR of less than 3 pc (*i.e.* < 0.15 arcsec).

A detailed observational analysis in the mid-infrared was performed by Packham *et al.* (2005). The authors found extended emission with 2 arcsec size at position angles of 81° and 278° , which is consistent with the edges of the aforementioned ionisation cones. However, their PSF analysis indicates that any extended nuclear emission in the mid-infrared has sizes less than 0.20 arcsec (4 pc) or is very weak. This confirms that single dish observations with current telescopes are not capable of resolving the nuclear dust distribution even for the nearest AGN, such as Circinus. For this reason, interferometric observations of the Circinus nucleus in the mid-infrared with the Very Large Telescope Interferometer (VLTI) were performed.

This chapter is organised as follows. In section 4.2 we present the details of the observations and of the data reduction. Section 4.3 describes the properties of the interferometric data and the results directly deducible from them. Section 4.4 treats the modelling of the

¹Tristram *et al.* (2007), to be submitted to A&A.



Figure 4.1: 2MASS Atlas image mosaic of the Circinus galaxy, covering 8.0×8.0 arcmin on the sky. Image mosaic by S. Van Dyk (IPAC).

data: in three steps the complexity is increased from a one-dimensional size estimate to a two-dimensional physical model. The interpretation of our findings and implications thereof are discussed in section 4.5. Our conclusions are given in section 4.6.

4.2 Observations and data reduction

4.2.1 Observations

The data were acquired between February 2004 and May 2006 during a total of six epochs. The first data set was obtained in February 2004 in science demonstration time (SDT). All following observations were carried out using guaranteed time observations (GTO). Table 4.1 gives a summary of the observations.

For our observations, we used the default values for the chopping frequency ($f = 2$ Hz) chopping angle ($\alpha = 0$) and chopping throw ($\delta = 15$ arcsec) except for the observations on 2004 Jun 03, where a smaller throw of $\delta = 10$ arcsec was used. For the acquisition of Circinus, we used the SiC filter at longer wavelengths because of the rising spectrum of the source. For the acquisition of the calibrator stars, which are in the Rayleigh-Jeans part of their spectra, we used the N8.7 filter at shorter wavelengths. For the fringe track, we preferred to observe in “offset tracking” mode with the OPD stabilised at $50 \mu\text{m}$ from 0 OPD, because this is of advantage for a coherent data analysis. The observations on 2004 Jun 03 and 2005 Feb 21 and the first visibility point on 2005 Feb 28 were, however, observed tracking on the white light fringe. During these periods, the standard tracking software implemented at Paranal did not allow for using offset tracking.

Because our data were obtained over such a long period of time, the observation techniques evolved in the meantime. Additionally, the instrument itself has improved considerably since

Table 4.1: Log of the observations. Times, ambient values and baseline properties are for the start of the fringe track.

Date and time [UTC]	Object	DIT [mas]	NDIT fringes	NDIT phot. ^b	Airmass	Seeing ^a [arcsec]	BL [m]	PA [°]	Associated calibrator and comments		
2004 Feb 12:	UT3 – UT2										
06:55:11	Circinus	sci01	0.020	12000	(2000)	1.473	0.96	43.49	19.30	cal01	photometry unusable, used phot of sci02
07:06:46	Circinus	sci02	0.020	12000	2000	1.449	0.91	43.36	21.49	cal02	photometry used for sci01 and sci02
07:36:34	HD 120404	cal01	0.012	12000	2000	1.456	1.08	41.39	32.16		
08:27:38	HD 120404	cal02	0.012	12000	2000	1.416	0.56	40.33	42.18		
2004 Jun 03:	UT3 – UT2										
05:50:45	Circinus	sci03	0.012	8000	1500	1.693	0.68	29.16	92.99	cal03	
06:42:24	HD 120404	cal03	0.012	8000	1500	2.095	0.65	25.40	117.87		
07:58:04	Circinus	sci04	0.012	8000	(1500)	2.542	0.73	20.74	129.68	cal03	phot B unusable, replaced by copy of phot A
2005 Feb 21:	UT2 – UT4										
04:38:01	HD 107446	cal05	0.012	8000	1500	1.367	0.83	87.87	51.88		
05:25:00	Circinus	sci05	0.012	8000		1.617	0.77	87.38	35.68	cal05	use photometry from 2005-03-01T04:38:30
2005 Mar 01:	UT3 – UT4										
03:34:58	HD 120404	cal06	0.012	8000	1500	1.906	0.95	50.87	39.76		dsky = -2
04:06:04	Circinus	sci06	0.012	8000	1500	1.809	0.75	49.33	44.58	cal06	dsky = -2
04:38:30	Circinus	sci07	0.012	8000	1500	1.671	0.72	50.99	53.61	cal07	photometry used for sci07 and sci08
04:49:21	Circinus	sci08	0.012	8000		1.631	0.71	51.57	56.54	cal07	no photometry observed, used phot of sci07
05:12:31	HD 120404	cal07	0.012	8000	1500	1.581	0.55	54.82	65.93		
06:58:52	Circinus	sci09	0.012	8000	1500	1.358	0.74	58.09	88.34	cal08	
07:28:53	HD 120404	cal08	0.012	8000	1500	1.412	0.48	59.77	98.71		
09:21:08	Circinus	sci10	0.012	8000	1500	1.345	0.64	61.95	120.00	cal09	photometry used for sci10 and sci11
09:43:25	HD 120404	cal09	0.012	8000	1500	1.480	0.78	62.10	129.42		
10:08:22	Circinus	sci11	0.012	8000		1.400	1.25	62.36	130.50	cal09	no photometry observed, used phot of sci10
2005 May 26:	UT2 – UT3										
22:57:46	HD 120404	cal10	0.012	8000	1500	1.666	0.60	42.62	11.21		
23:29:03	Circinus	sci12	0.012	8000	3000	1.563	0.63	43.77	12.79	cal10	reset chopping in second half of phot B
23:43:07	Circinus	sci13	0.012	5000	3000	1.524	0.54	43.67	15.47	cal10	
01:37:29	Circinus	sci14	0.018	5000	3000	1.340	0.67	41.98	37.05	cal11	
02:02:11	HD 120404	cal11	0.018	5000	1500	1.409	1.52	39.64	47.39		
03:40:07	HD 120404	cal12	0.018	5000	1500	1.454	0.85	36.24	67.11		
04:07:02	Circinus	sci15	0.018	5000	3000	1.374	0.75	36.82	65.28	cal12	
04:17:27	Circinus	sci16	0.018	5000	3000	1.387	0.98	36.31	67.31	cal12	
04:28:22	Circinus	sci17	0.018	5000	3000	1.404	1.05	35.77	69.45	cal12	
2006 May 18:	UT2 – UT3										
06:16:21	Circinus	sci18	0.018	8000	4000	1.560	1.50	31.69	84.18	cal13	
06:42:24	HD 120404	cal13	0.018	8000	4000	1.788	0.84	28.96	100.07		
07:09:48	Circinus	sci19	0.018	8000	4000	1.754	0.98	28.21	96.40	cal13	
07:36:18	HD 120404	cal14	0.018	8000	4000	2.035	0.78	25.98	114.66		rejected due to very low correlated flux
08:04:13	Circinus	sci20	0.018	8000	4000	2.049	0.59	24.51	110.75	cal13	photometry used for sci20 and sci21
08:17:34	Circinus	sci21	0.018	8000		2.142	0.67	23.61	114.69	cal13	no photometry observed, used phot of sci20

^aFrom the seeing monitor (DIMM).^bA missing value signifies that no photometry was observed. A value in brackets denotes that the photometry was unusable.

the first observations were made in February 2004. This leads to a large variety of exposure times ranging from $DIT = 12$ ms to 20 ms. Similarly, the frame numbers range from $NDIT = 5000$ to 12000 for the fringe tracking and from $NDIT = 1500$ to 4000 for the photometry (see table 4.1). For the first 4 visibility points, only a tip tilt correction for the incoming wavefronts was possible using the STRAP units (Bonaccini *et al.*, 2000). A much better correction was obtained with the MACAO adaptive optics system (Arsenault *et al.*, 2003) since its implementation in late 2004, *i.e.* starting with our observations in February 2005. For Circinus, both systems were operated with a separate guide star at $50 \pm 2''$ distance from the nucleus. For the observations of the calibrators, the wavefront sensing was performed using the stars themselves. The overall ambient conditions for all the observations were good with seeing values from the site monitor varying from 0.5 to 1.8 arcsec. We had no problems with clouds or constraints due to wind, except for one observation. This observation (“sci05”), carried out in service mode on the UT2 – UT4 baseline, had to be aborted due to clouds building up over Paranal. Thus, no photometric data could be obtained for this measurement.

4.2.2 Data reduction

Not all measurements contain the full data set consisting of a fringe track and two photometries, so that they could be reduced in a straightforward manner. This has three reasons: first of all, several measurements were performed at the end of the night or of the allocated time and only the fringe track could be obtained. Secondly, for some measurements the photometries proved to be unusable or to be of very low quality. Finally, for the measurement on the UT2 – UT4 baseline, no photometry could be obtained at all due to the adverse weather conditions. To nevertheless make use of all the fringe tracks obtained, we completed the fragmentary data sets with photometric data from the other measurements preferably using measurements as close as possible in time. The details are included in the last column of table 4.1.

The data reduction was entirely performed by coherent visibility estimation using the software package EWS (*c.f.* section 3.2). The alternative software package MIDI Interactive Analysis (MIA), which is based on a power spectrum analysis, was only used to cross-check the results for a selected number of observations: in these cases the two methods gave consistent results. For the calibration, we exclusively used the calibrator HD 120404 associated with Circinus, with the exception of one case, the long baseline UT2 – UT4, where HD 120404 was not observed at all. In this case, we used HD 107446 instead. The quality of the calibrators were checked by comparison to all the other calibrators observed during the same night. We decided to reject only one calibrator measurement because of its low correlated flux compared to the other measurements during the night: cal14 observed on 2006 May 18 at 07:36:18. We corrected the Rayleigh-Jeans approximation for the template spectrum of the calibrator using a template spectrum, F_{cal} , from a database provided by Roy van Boekel, (*private comm.*). These template spectra were obtained by fitting stellar templates to multiband photometry (*c.f.* section 3.3).

The entire data reduction and calibration was performed in the same manner for all visibility points without any further individual adjustment of the parameters, in order not to introduce any biases.

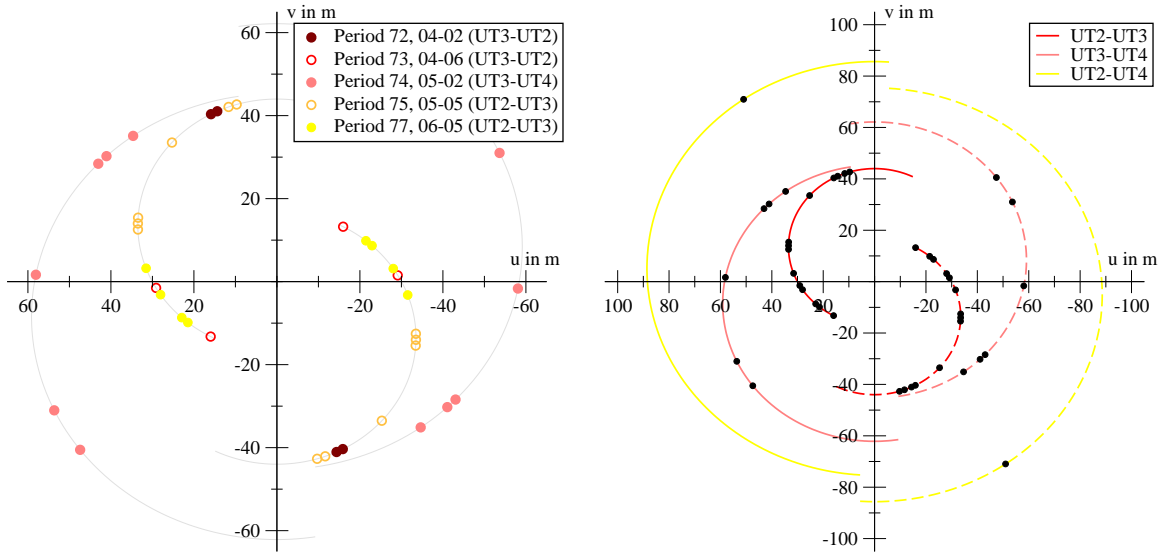


Figure 4.2: uv coverage for the Circinus galaxy obtained with MIDI, the MID-infrared Interferometric instrument at the VLTI. The left plot shows the position of the observed fringe tracks in the uv plane for the two shorter baselines, UT2 – UT3 and UT3 – UT4. The points are coded according to the epoch of observation. The right plot shows all the 21 observed fringe tracks as well as the uv tracks of the baselines for the three combinations of unit telescopes that were used.

4.3 Results

4.3.1 uv coverage

The interferometric data collected on Circinus constitute the most extensive interferometric data in the infrared or at shorter wavelengths of any extragalactic source so far. The uv coverage achieved is shown in figure 4.2. Each point represents the position of a fringe track leading to a visibility point. Because we measure the interferometric signal of a real function (namely the brightness distribution) which has a symmetric Fourier transform, there are two points for each measurement, symmetrical to the centre (*c.f.* equation 2.33). The different colours denote the different epochs of observation. We observed 21 fringe tracks and 31 usable photometries (note this is not the double of the fringe track number as it should optimally be; there are only 15 usable A photometries and 16 usable B photometries) for Circinus as well as 12 fringe tracks plus 24 photometries for HD 120404, the calibrator star. We were able to reconstruct a total of 21 visibility points from the data.

The distribution of the measurements in the uv plane in figure 4.2 has concentrations at several locations, that is, two or three points at almost the same location. This was caused by consecutive measurements of the interferometric signal. The differences between such measurements can be considered as indications for the accuracy of the measurements themselves. Several measurements also share the same photometry or calibrator data. In a strict sense, the true number of absolutely independent measurements is thus only on the order of 12, which is the number of independently measured calibrator data sets.

The observations were performed with only three baseline configurations: UT2 – UT3, UT2 – UT4 and UT3 – UT4. This causes the visibility points to lie on arcs in the uv plane, which correspond to the classical uv tracks known from radio interferometry. The uv tracks for these three baseline configurations are plotted in figure 4.2 as continuous lines. The uv

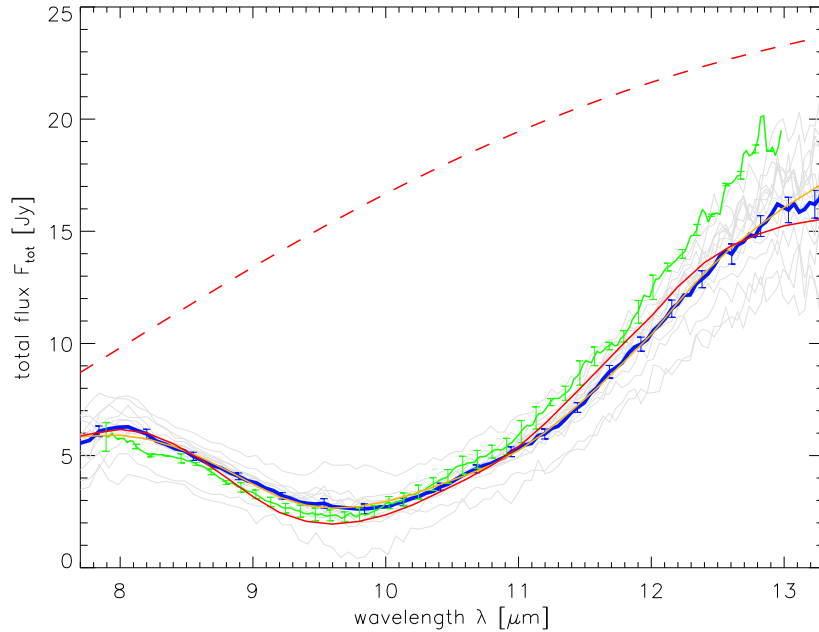


Figure 4.3: Spectrum of the total flux of the Circinus nucleus in the N band. The light grey curves are the 15 individual measurements of the total flux; error bars were omitted for the sake of clarity. The thick blue curve is the arithmetic mean of all the individual measurements, the error bars indicating the reduced standard deviation. The spectrum measured by Roche *et al.* (1991) is shown in green for comparison. The orange curve shows the fit of the model to the total flux only (fit 1), while the red curve shows the fit to the full data set consisting of the total flux and the correlated fluxes (fit 2). The dashed red curve is the emission for the latter fit, without including the extinction by dust. For details on the modelling, see section 4.4.4.

coverage is far from optimal, as there are several regions lacking measurements: at a position angle of -20° , no measurements were obtained at all and at a position angle of $+20^\circ$ only one baseline length ($BL = 40$ m) was observed. The void regions therefore need to be filled in by future observations.

4.3.2 Total flux

Figure 4.3 shows the calibrated total flux $F_{\text{tot}}(\lambda)$ of the Circinus nucleus, that is, its spectrum. In several of the individual measurements (light grey lines), a larger jiggle is visible between 9.5 and $10.0 \mu\text{m}$. This is due to absorption by ozone in the atmosphere of the earth, significantly decreasing the signal-to-noise ratio in this part of the spectrum. This is aggravated by the fact that the ozone feature coincides with the minimum of the flux in the intrinsic spectrum of Circinus. The individual measurements are all consistent with the average, when the associated individual errors (not shown in figure 4.3) are considered. The curves with the largest deviations from the average come from the measurements in 2004. These also have larger individual errors. The variations are mainly caused by imperfect background subtraction for early data or observations at high airmasses. We clearly see an increase in the data quality after the first measurements. The edges of the N band are located at $8.2 \mu\text{m}$ and $13.0 \mu\text{m}$. Towards shorter and longer wavelengths, the atmosphere is almost not transparent due to water absorption. Due to the large number of measurements, the averaged total flux is nevertheless usable beyond these boundaries.

The broad absorption feature dominating most of the spectrum is due to silicate absorption. We see no evidence for any line emission or emission of Polycyclic Aromatic Hydrocarbons (PAH), as observed at larger distances from the nucleus (*e.g.* in larger apertures, Roche *et al.* 2006). The nuclear spectrum measured by Roche *et al.* (2006) agrees with our measurement of the total flux within 20% (see figure 4.3). The differences are probably due to the higher spectral resolution ($R \sim 125$) and the different orientation of the slit in the Roche data.

4.3.3 Interferometric data

For all baselines observed, the visibility is well below $V = 1$, indicating that the emission region is well resolved with our interferometric resolution of $\lambda/2B \leq 40$ mas. By way of example, the correlated fluxes $F_{\text{cor}}(\lambda)$ and visibilities $V(\lambda)$ obtained on 2005 Feb 28 are shown in figure 4.4. During this night, observations were performed using the baseline UT3 – UT4. The baseline length only increased from 50 to 60 m, while the position angle underwent a major change from 44° to 131° . As in the total flux, the broad dip at $10 \mu\text{m}$ is due to silicate absorption. The quality of the data at the edges of the wavelength range and in a window between 9.5 and $10.0 \mu\text{m}$ deteriorates significantly due to atmospheric water and ozone absorption. We therefore only trust the spectra within these boundaries, that is, from $8.2 \mu\text{m}$ to $9.5 \mu\text{m}$ and from $10.0 \mu\text{m}$ to $13.0 \mu\text{m}$.

A clear increase of the correlated flux and the visibility can be observed, when the position angle increases. The increase is most evident in the correlated fluxes longward of $11 \mu\text{m}$. We directly interpret this as a change of size of the emitting source: at position angles of 44° to 57° the correlated flux and the visibility are low, *i.e.* the source is more resolved and hence the emission extended, while at angles of 120° and 131° the correlated flux and visibility are higher, *i.e.* the source is less resolved and, by consequence, the emission less extended. This statement is reinforced by the small increase in baseline length towards larger position angles, as the correlated flux and visibility should diminish (assuming a smooth brightness distribution): the change of size with position angle also has to overcome this effect. This is a direct and completely model independent evidence for an elongated structure perpendicular to the ionisation cone and outflow at $PA = -50^\circ$ in the Circinus galaxy.

Both, the visibility and the correlated flux can be used to analyse the structure of the target and both exhibit advantages and disadvantages. The visibility can be seen as measuring the “resolvedness” of the source, that is, it contains geometrical information on the source. The correlated flux can be interpreted as the remaining emission from the unresolved part of the source, which per se does not contain any geometrical information. It only receives a geometrical meaning after also providing the total flux. From our observations we know that the photometry is the most uncertain part of the measurement and we have less independent measurements of photometries than fringe tracks. Due to the determination of the correlated flux without involvement of the photometry as described in section 3.3, the uncertainties of the photometry have no influence on the correlated flux. The visibility, however, always contains the photometry, including its uncertainties. On the other hand, the correlated flux is not corrected for the alignment of the beams which has a significant influence on its amplitude. This is the reason for also observing the photometry in the first place. Indeed, some of the fluctuations in the photometries can be explained by the aforementioned factors. As the photometries enter into the calculation of the visibilities, the visibilities should be insensitive to misalignments or atmospheric transparency losses. We have checked the data and found no evidence for any misalignment (within 2 pixels, that is 160 mas, accuracy), so that the main source of variation must lie in the atmospheric transparency and sky brightness. Eventually,

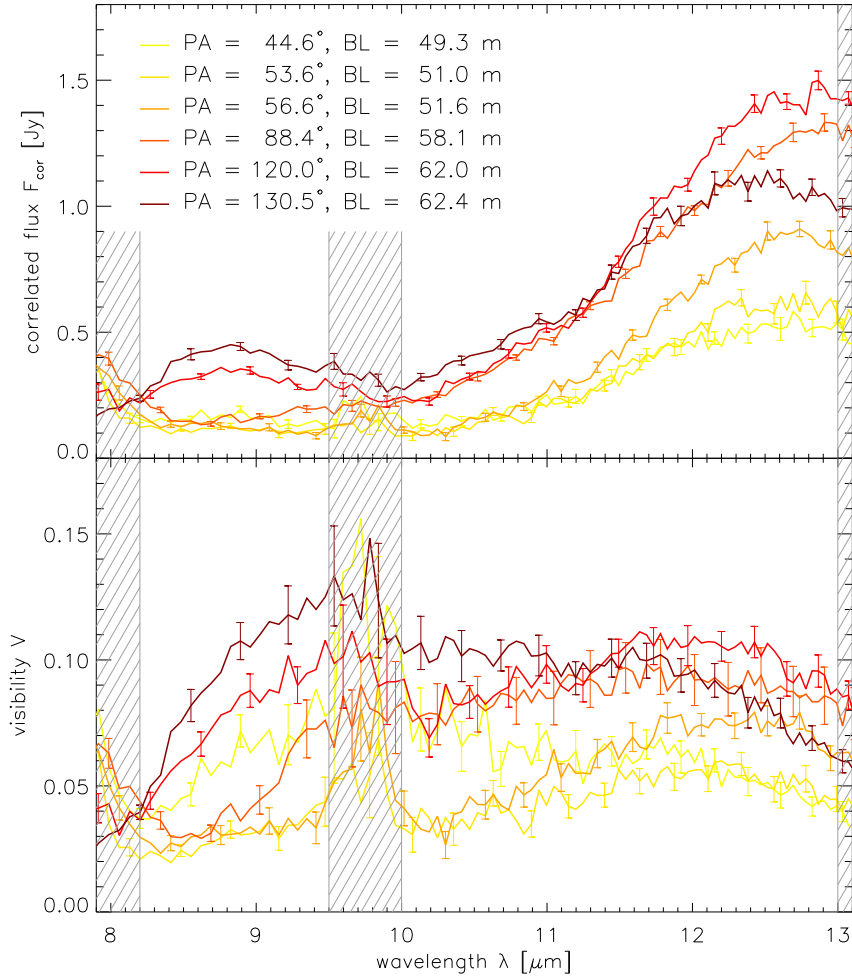


Figure 4.4: Top panel: Spectra of the correlated fluxes as observed during the night of 2002 Feb 28. Bottom panel: Visibilities for the same night. During these observations, mainly the position angle (PA) changed, while the projected baseline length (BL) stayed roughly the same. From the change in the correlated fluxes, direct implications on the morphology can be derived: the source observed is considerably more extended in the direction of $PA \sim 50^\circ$ than in the direction of $PA \sim 130^\circ$. Areas affected by atmospheric absorption are hatched in grey.

we consider both the visibilities and the correlated fluxes equally trustworthy and we will use both for the modelling described in the next section. Furthermore, we find that the essential information content is the same for both the visibilities and the correlated fluxes. This is reassuring.

The differential phase is less than 20° for almost all baselines. At the shortest baselines, we find some evidence for a phase shift and there is also weak evidence for phase shifts at positions where the visibilities show unexpected behaviour (especially for sudden downturns at the edge of the spectral range covered). Nevertheless, we find no evidence for a major asymmetry in the source. We therefore postpone a detailed analysis of the differential phase information to a later stage (*c.f.* section 7.1.1) and concentrate in this chapter on the interpretation of the visibility amplitude only.

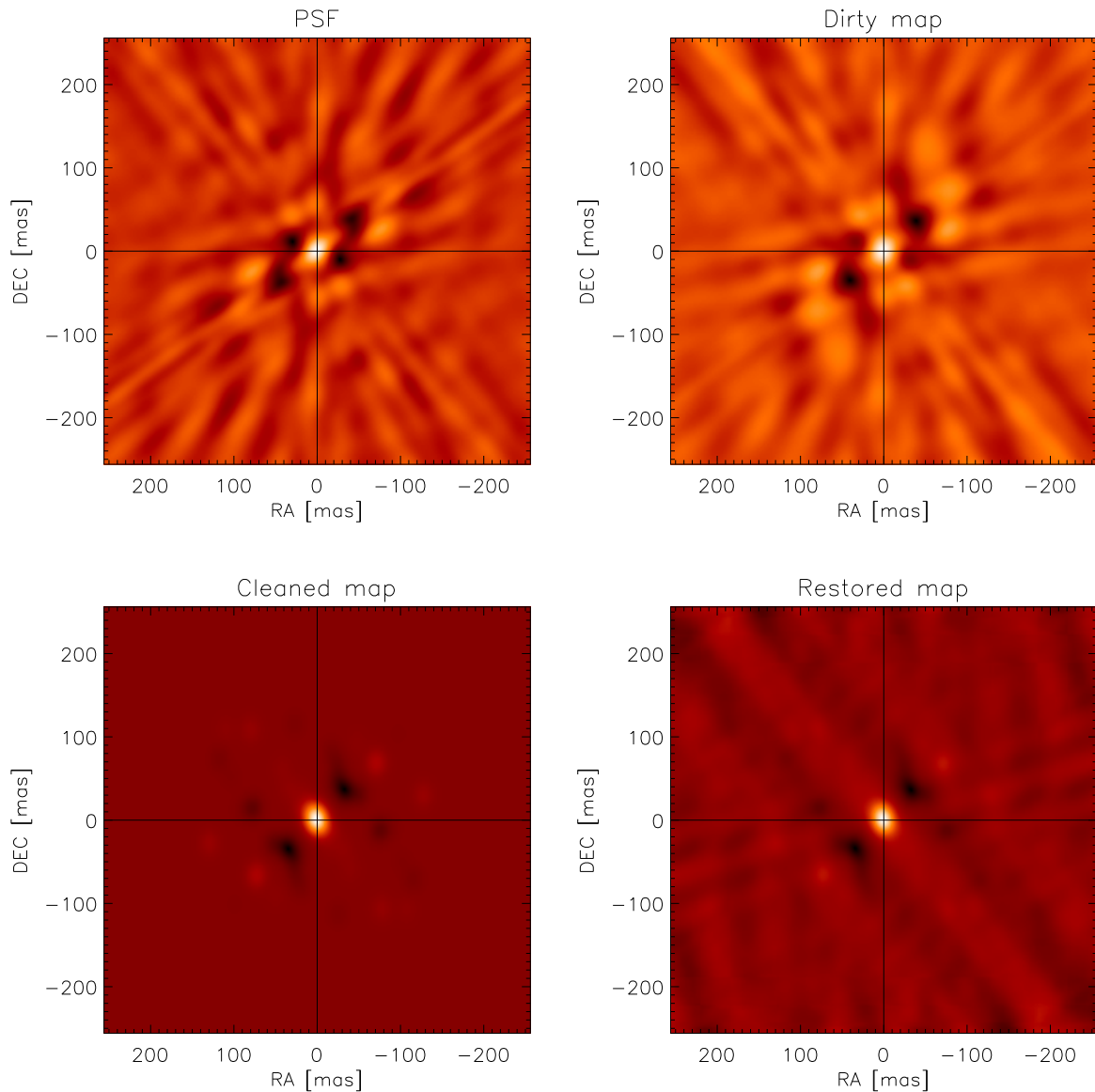


Figure 4.5: Attempt to reconstruct an image from the MIDI data on Circinus (see text for details).

4.4 Modelling

4.4.1 Image reconstruction attempt

In radio interferometry, commonly a flux distribution can be directly determined from the data by an inverse Fourier transform and a prescription, such as the “clean algorithm”. We tried applying such an algorithm to our data (see figure 4.5). The *beam* (top left in figure 4.5) corresponding to the measurements is essentially the Fourier transform of the uv plane shown in figure 4.2 with the visibility of each uv point set to 1. This would have been the case, had a point source been observed. Thus also the term *point spread function* (PSF), which is more commonly used in optical astronomy. The beam only contains information on the uv coverage. Due to the often low coverage of the uv plane, it normally contains strong periodic

patterns, the *side lobes*. The dirty map (top right in figure 4.5) is the Fourier transform of the uv plane including the visibility and phase information as given by equation (2.50). In a simple clean algorithm, the brightest peak is found in the dirty map. Normally also negative peaks are allowed. The peak of the beam is scaled to a certain fraction of the peak height, the so-called *gain* g (in our case $g = 0.2$), and then subtracted from the dirty map at the position of the peak. This procedure is carried out iteratively on the residual map, until the residuals are small enough. For each iteration i , the position of the peak (x_i, y_i) and the peak value h_i are noted. A Gaussian distribution is fitted to the core of the beam to obtain an estimate for the resolution of the interferometric set-up. This Gaussian is shifted to the position (x_i, y_i) and scaled to $g \cdot h_i$ for every iteration i . The *cleaned map* (bottom left in figure 4.2) is the sum of all these Gaussian distributions. It is supposed to be the best estimate for the source flux distribution. Finally the *restored map* (bottom right in figure 4.2) is the cleaned map plus the residual from the last peak fitting iteration.

As can be seen from figure 4.2, the form of the beam corresponding to our uv coverage is very bad and shows strong side lobes, which dominate the outcome of the reconstruction process. The results of such a reconstruction attempt are very poor and hard to interpret, reflecting only the general properties of the source. These general properties are much better constrained by the models considered in the following. We conclude that the current uv coverage of Circinus is unsuitable to attempt any image reconstruction.

In order to interpret the visibilities and extract information on the flux distribution and physical properties of the source, the data thus need to be fitted by models. Our approach to model the data consists of several steps of increasing complexity, avoiding any preconceptions due to an a priori knowledge of the source. The goal is to extract properties of the mid-infrared emission, such as size, elongation, depth of the silicate feature, etc. This will enable us to make statements concerning the nuclear dust distribution in the Circinus galaxy. The analysis was performed using the Interactive Data Language (IDL).

4.4.2 1D model

The first step in our analysis had the aim to obtain an estimate of the size of the emission region. To this end, we assumed the source to be rotationally symmetric and plotted all visibility measurements, regardless of the position angle, as a function of the baseline length BL : $V_\lambda(BL)$. This is typically done when analysing rotationally symmetric objects such as stars. This can be done for every wavelength bin measured independently with MIDI. Examples for such a plot are shown for two wavelengths, $8.5 \mu\text{m}$ and $12.5 \mu\text{m}$, in the top row of figure 4.6. The distribution of data points shows a decrease from 1 ($BL = 0$ m) with increasing baseline length and an irregularly oscillating behaviour for $BL > 35$ m. At first glance, the dependency is reminiscent of the expected visibility function for a uniform disk, which is a Bessel function of the first kind of order 1: $|J_1(BL)|$. The direct comparison in figure 4.6 reveals large discrepancies between such a Bessel function and the data. Additionally, our data shows no evidence for the 2π phase jumps that occur at the zero crossings of the Bessel function. We thus conclude that a uniform disk model cannot explain the data.

We chose an alternative approach to analyse the data: First we interpolated $V_\lambda(BL)$ using a linear spacing of 0.5 m for the baseline length BL . This interpolation was extended to a maximum baseline of 1000 m (blue curves in the top row of figure 4.6). We then applied an inverse Fourier transform to this visibility function for each wavelength bin: $I_\lambda(d) = \mathcal{F}_{BL}[V_\lambda(BL)](d)$. This reconstruction method gives a first order estimate of the radial brightness distribution of the nucleus $I_\lambda(d)$, where d is the angular distance from the centre. The shape of the visibility function $V_\lambda(BL)$ is only well determined for $20 \text{ m} < BL < 90 \text{ m}$. This in turn implies that we

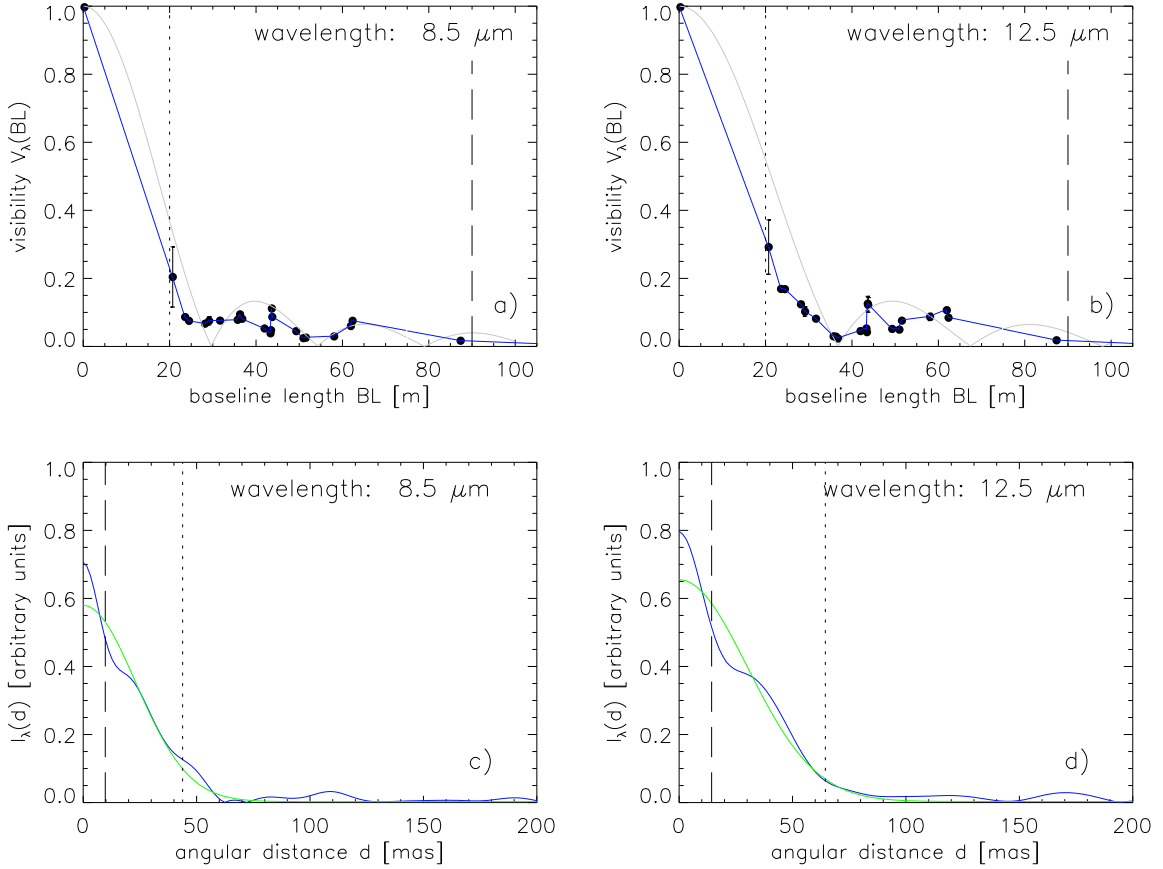


Figure 4.6: Radial 1D analysis of the mid-infrared emission in Circinus. Top row: Visibility as a function of baseline length for two wavelengths: $8.5\ \mu\text{m}$ (a) and $12.5\ \mu\text{m}$ (b) taking together all position angles. The data cannot be explained by a uniform disk model (light grey curves). The blue curve is an interpolated visibility function derived from the data. Bottom row, (c) and (d): For the same wavelengths, the inverse Fourier transform of the blue curve in the top row graphs is plotted, corresponding to a brightness distribution. Traced in green is the Gaussian distribution fitted to the Fourier transform in order to get an estimate for the size of the emitting source. The vertical lines indicate the angular size range probed by the interferometric measurements.

have probed angular sizes d between 10 and 70 mas, considering the entire wavelength range of the MIDI observations. These characteristic sizes in the Fourier and the real domain are indicated by vertical dashed and dotted lines in figure 4.6.

The reconstructed brightness distribution is composed of two components plus a small fraction of extended flux at distances of more than 100 mas of the centre. The extended component is fully resolved by our interferometric set-up, while our measurements probe the properties of the other two components. One should bear in mind that we assumed rotational symmetry for this analysis and already from the qualitative discussion of the data in section 4.3 we know that this is a crude simplification. We therefore used the reconstructed brightness distribution only to extract the effective size of the emission region in the mid-infrared and traced its evolution depending on the wavelength. For the sake of simplicity, this was achieved by fitting a Gaussian distribution to the reconstructed radial profiles at every wavelength bin. This Gaussian is shown in green in the bottom row of figure 4.6. A plot of the full width at half maximum (FWHM) of this Gaussian distribution is displayed in

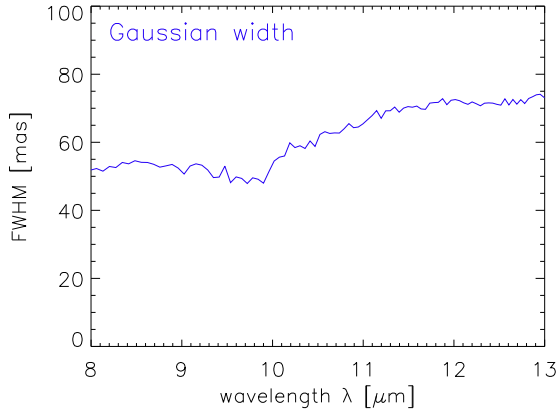


Figure 4.7: *FWHM* of the Gaussian distribution fitted to the radial profile of the brightness distribution of the Circinus nucleus (see figure 4.6). This first estimate for the effective size of the nuclear dust emission shows a slow increase with wavelength from 50 to 75 mas.

figure 4.7. We attribute the small dip in the size between 9.5 and 10.0 μm to artefacts coming from the ozone feature. From shorter to longer wavelength, the size of the flux distribution increases slightly from 50 to 75 mas. This indicates that the emission at longer wavelengths is more extended than at short wavelengths: the temperature of the dust decreases slowly with distance to the nucleus.

The concentration of the flux on scales of less than 100 mas again demonstrates the need for interferometric observations, as they are the only way to reach these resolutions in the infrared.

4.4.3 2D geometrical model

The next step of modelling consists of a two-dimensional, purely geometrical model, aimed to reconstruct the brightness distribution of the source from the visibilities. The model consists of two elliptical Gaussian distributions. We suspected such a model to be a good representation for the full two-dimensional data after finding an indication for two components in the one-dimensional analysis. The ellipticity is motivated by the fact that the direct inspection of the visibilities (section 4.3.3 and there especially figure 4.4) shows strong evidence for an elongation of the source. The brightness distribution has the following functional form²:

$$I(\lambda, \alpha, \delta) = f(\lambda) \cdot \exp \left(-4 \ln 2 \cdot \left[\left(\frac{\alpha \cos \phi(\lambda) + \delta \sin \phi(\lambda)}{r_1(\lambda) \cdot \Delta_1(\lambda)} \right)^2 + \left(\frac{\alpha \sin \phi(\lambda) - \delta \cos \phi(\lambda)}{\Delta_1(\lambda)} \right)^2 \right] \right) + \exp \left(-4 \ln 2 \cdot \left[\left(\frac{\alpha \cos \phi(\lambda) + \delta \sin \phi(\lambda)}{r_2(\lambda) \cdot \Delta_2(\lambda)} \right)^2 + \left(\frac{\alpha \sin \phi(\lambda) - \delta \cos \phi(\lambda)}{\Delta_2(\lambda)} \right)^2 \right] \right) \quad (4.1)$$

Here, α and δ are the offsets from the centre of the distribution in right ascension and declination respectively. This two component model has a total of six free parameters: the sizes of the two Gaussians, given by their full width at half maximum $\Delta_1(\lambda)$ and $\Delta_2(\lambda)$, their oblateness, represented by the axis ratio $r_1(\lambda)$ and $r_2(\lambda)$, the position angle $\phi(\lambda)$ of the major axis with respect to north and the relative intensity of the two components with respect to each other which is quantified by the factor $f(\lambda)$ for one of the components.

These parameters were then optimised using the following prescription: for a certain wavelength λ the flux distribution $I_\lambda(\alpha, \delta) = I(\lambda, \alpha, \delta)$ was generated according to the set of parameters. Then the Fourier transform $\mathcal{V}_\lambda(u, v) = \mathcal{F}_{\alpha, \delta} [I_\lambda(\alpha, \delta)](u, v)$ was calculated

²To be more descriptive, we use the FWHM $\Delta_n = 2\sqrt{2 \ln 2} \sigma_n$ in our definition of the Gaussian distribution instead of the variance σ_n in the standard definition.

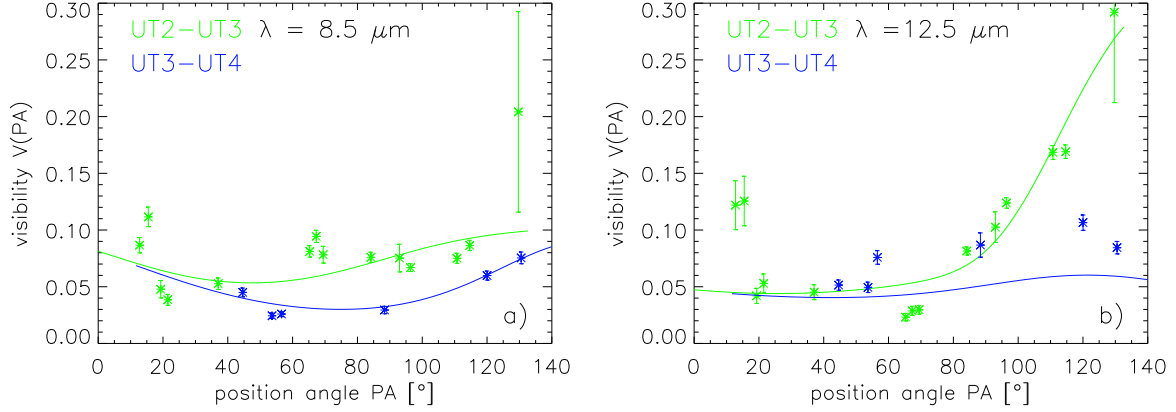


Figure 4.8: Comparison of the visibilities of the geometrical model (two elliptical Gaussian distributions) to the measured data for two distinct wavelengths: (a) 8.5 and (b) 12.5 μm . The data is plotted with asterisks; the modelled visibilities are the continuous lines. The two baselines shown here are plotted in two different colours, UT2 – UT3 in green (grey) and UT3 – UT4 in blue (black).

using a fast Fourier transform (FFT). The result corresponds to the visibility distribution in the uv plane. The visibility values for the model were extracted from this plane at the positions $u_i = BL_i \cdot \sin PA_i$, $v_i = BL_i \cdot \cos PA_i$, using the baseline information from our observations i consisting of the baseline length BL_i and the position angle PA_i . Finally, the modelled visibilities $V_i^{\text{mod}}(\lambda) = |\mathcal{V}_\lambda(u_i, v_i)|$ were compared to the observed ones $V_i^{\text{obs}}(\lambda)$. The discrepancy was weighted with the measurement errors $\sigma_{V_i^{\text{obs}}(\lambda)}$ to obtain the χ^2 :

$$\chi^2(\lambda) = \sum_{i=1}^{21} \left(\frac{V_i^{\text{obs}}(\lambda) - V_i^{\text{mod}}(\lambda)}{\sigma_{V_i^{\text{obs}}(\lambda)}} \right)^2. \quad (4.2)$$

The χ^2 was minimised using the Levenberg-Marquardt least-squares minimisation algorithm. This process was performed independently for the 51 wavelength bins measured by MIDI between 8 and 13 μm . A comparison of the model to the data is shown for 8.5 and 12.5 μm in figure 4.8. The resulting parameter dependencies are shown in figure 4.9. To have more practical parameters, the factor f was replaced by the ratio R of the flux in the compact component to the flux in the extended component. The reduced χ^2 (that is $\chi^2(\lambda)/N_{\text{free}}$ with $N_{\text{free}} = 21 - 6 = 15$ degrees of freedom), shown in the left panel of figure 4.10, varies strongly for different wavelengths. The fits are best in the middle of the wavelength range. Towards the edges of the N band, the fits get significantly worse. This is mainly due to the weighting of the discrepancy between model and data using the errors of the data $\sigma_i^{\text{obs}}(\lambda)$. Due to the bad signal-to-noise ratio for low fluxes, the errors are of the same order, or even larger within the silicate absorption feature, the atmospheric ozone feature, as well as at the edges of the N band. When considering a modified estimate for the quality of the fit,

$$\xi^2(\lambda) = \sum_{i=1}^{21} \left(\frac{V_i^{\text{obs}}(\lambda) - V_i^{\text{mod}}(\lambda)}{V_i^{\text{mod}}(\lambda)} \right)^2, \quad (4.3)$$

the discrepancy is of the same order, except at $\lambda > 12 \mu\text{m}$. The reduced ξ^2 , $\xi^2(\lambda)/N_{\text{free}}$, is shown in the right panel of figure 4.10.

With the high values of the reduced χ^2 , the fit is comparatively bad. This is partly due to an overly optimistic estimate of the errors of the visibilities. The errors only represent the

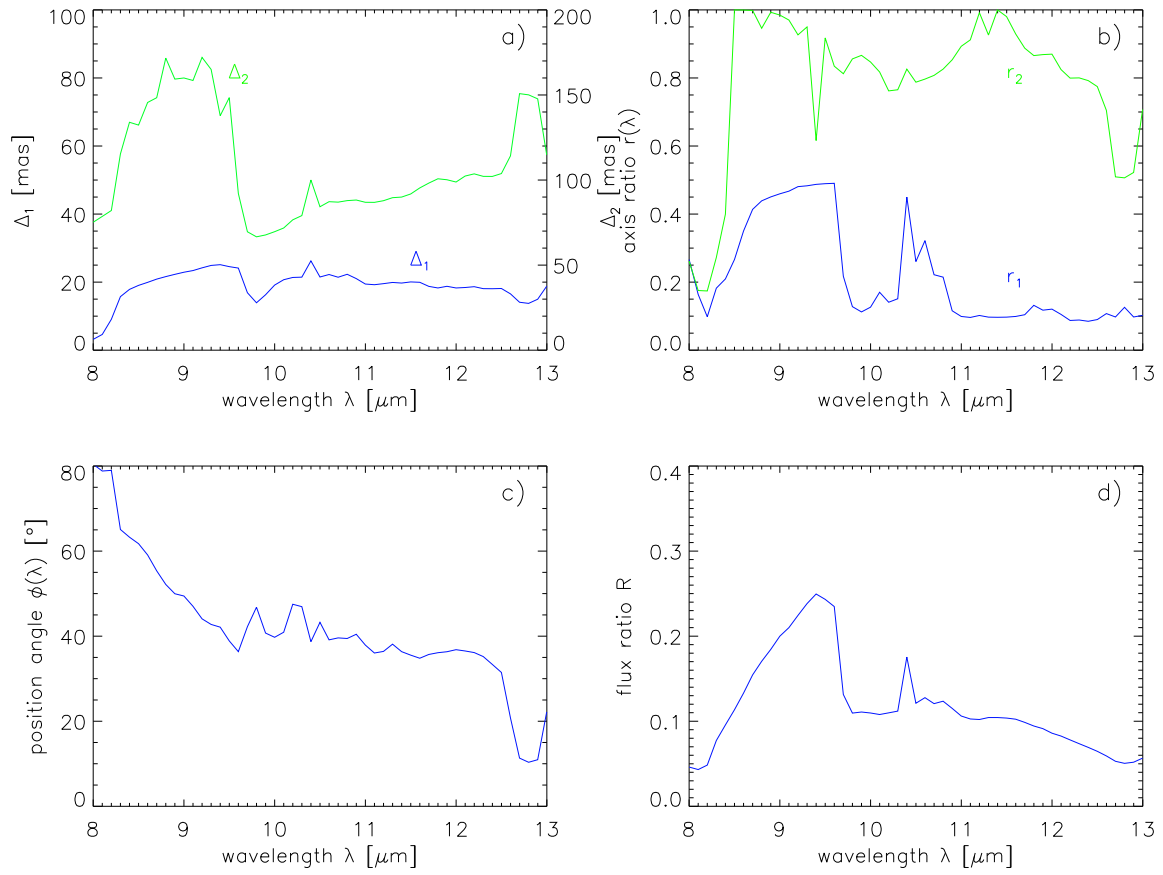


Figure 4.9: Dependence of the parameters for the two-dimensional geometric model on the wavelength. The six parameters are the two *FWHM* of the Gaussian components (a), the respective axis ratios r (b), the position angle ϕ of the elliptical distribution (c) and the ratio R of the flux in the compact over the extended component (d).

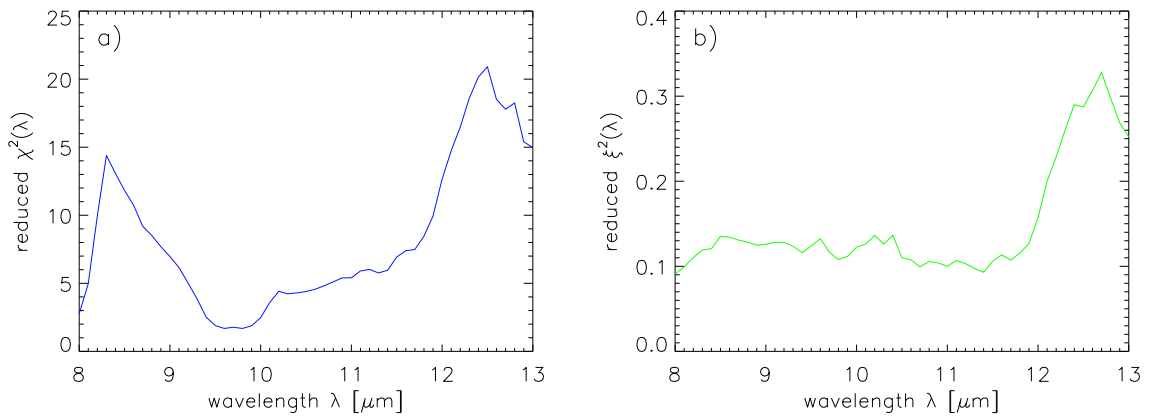


Figure 4.10: χ^2 (a) and ξ^2 (b) for the fit of the two component Gaussian model to the visibilities.

relative errors within one measurement and do not reflect the systematic errors between two measurements at different epochs. More importantly, we see in the bad fit quality evidence for a more complex structure of the source. This will be discussed in section 4.4.4.

No clear trend of the parameters with wavelength is identifiable. The smaller component has a rather constant size of approximately $\Delta_1 \sim 20$ mas and a rather high axis ratio of $r_1 = 0.2$. The position angle has a preferred orientation of $PA \sim 40^\circ$, which is more or less perpendicular to the ionisation cone. Towards both ends of the spectral range sampled ($8.0 \mu\text{m} < \lambda < 9.0 \mu\text{m}$ and $12.5 \mu\text{m} < \lambda < 13.0 \mu\text{m}$), the position angle deviates significantly from this value. A more regular behaviour of the parameters is found in the range from 11.0 to $12.5 \mu\text{m}$. Here also the intensity ratio stabilises at $R \sim 0.1$ and the size of the second component grows linearly with increasing wavelength. The large component hence comprises the bulk of the emission. The ellipticity of the larger component is relatively small, with $r_2 \sim 0.75$ for large parts of the spectral range, again exceeding these margins at the edges of the spectrum sampled. Some of the parameters show a certain reciprocal influence: decreasing the inclination of the smaller component between 8.2 and $9.5 \mu\text{m}$ leads to a larger emitting region and hence to a larger flux, which has an influence on the flux ratio between the two components and the size of the larger component. We hence do not see the decrease of ellipticity of the small component to be significant but rather as an artifact of the ambiguity of the data. Especially the ellipticity, the size and the flux ratio of the two components show some degree of degeneracy. We found that, by fixing some of the parameters to average values (*e.g.* PA to 40° or r_1 to 0.2), the quality of the fit for the individual wavelengths does not increase significantly. At the same time, however, the behaviour of the other parameters, which are then adjusted, looks steadier. We did not follow this path of analysis any further but decided to apply a physical model instead (see section 4.4.4). The overall erratic behaviour of the parameters and the quality of the fit, however, show that two Gaussians are not a good fit and that there are substantial differences at different wavelength bins. Nonetheless, we find that other models of the same simplicity produce no better fits. A more detailed discussion of alternative models will be given in section 4.4.5.

4.4.4 2D physical model

This model takes the analysis one step further and attaches physical properties to the emission region. The model consists of two black body Gaussian emitters behind an extinction screen. For the absorption we used the typical wavelength dependency of the extinction of interstellar dust (Schartmann *et al.*, 2005), but modified the profile of the silicate absorption feature using data from Kemper *et al.* (2004). We did not use the profile towards SgrA as derived by Kemper *et al.*, as it only covers the wavelength range from 8.0 to $12.7 \mu\text{m}$. Instead, we used the dust characteristics observed towards GSC3. We find the profiles towards GSC3 and SgrA to be identical within the accuracy of the low spectral resolution power of MIDI. The silicate absorption in Kemper *et al.* (2004) is a template extinction profile for interstellar dust absorption and we found it to be sufficient to describe the absorption feature we observe with MIDI (see also discussion in section 4.5.6). The optical depth observed towards GSC3 was smoothed and interpolated in the wavelength range from 7.9 to $13.5 \mu\text{m}$, where it substituted the values of the typical optical depth curve. To obtain our template absorption profile $\tau(\lambda)$, the entire optical depth curve was then normalised to 1 at the maximum absorption depth of the silicate profile: $\tau(9.7 \mu\text{m}) = 1$.

Our two component model has the following functional form:

$$F(\lambda, \alpha, \delta) = f_1 \cdot G_1(\lambda, \alpha, \delta) \cdot e^{-\tau_1 \cdot \tau(\lambda)} + f_2 \cdot G_2(\lambda, \alpha, \delta) \cdot e^{-\tau_2 \cdot \tau(\lambda)} \quad (4.4)$$

where τ_1, τ_2 are the individual optical depths of the absorption screens. The covering factors f_1 and f_2 are factors to scale the intensity of the black body Gaussian distributions G_1 and G_2 . The Gaussian distributions in turn are defined by

$$G_n(\lambda, \alpha, \delta) = F_{\text{bb}}(T_n, \lambda) \cdot \exp \left(-4 \ln 2 \cdot \left(\frac{\alpha \cos \phi + \delta \sin \phi}{r_n \cdot \Delta_n} \right)^2 - 4 \ln 2 \cdot \left(\frac{\alpha \sin \phi - \delta \cos \phi}{\Delta_n} \right)^2 \right) \quad (4.5)$$

for each of the two components $n = 1, 2$. The parameters of the Gaussians (r_1, r_2 for the axis ratios, Δ_1 and Δ_2 for the FWHM and ϕ for the orientation) are the same as in the previous section, except that they are not any longer wavelength dependent. The black body intensity F_{bb} depends on the temperature T_n and is given by

$$F_{\text{bb}}(T_n, \lambda) = \frac{2hc}{\lambda^3} \frac{1}{\exp \left(\frac{hc}{k_B \lambda T_n} \right) - 1}, \quad (4.6)$$

where h is Planck's constant, c the speed of light and k_B Boltzmann's constant. This model has 11 free parameters: the FWHM Δ_n , the axis ratio r_n , the temperature T_n , the factor f_n and the optical depth τ_n for each of the two components $n = 1, 2$. The common position angle ϕ is the eleventh parameter³. Similar to the procedure applied in section 4.4.3, the flux distributions at several wavelengths were generated and Fourier transformed. From the resulting distribution in the uv plane, the visibilities corresponding to the observed baselines $V_i^{\text{mod}}(\lambda) = |\mathcal{V}_\lambda(u_i, v_i)|$ were extracted. Additionally, the total flux was determined by integrating over the entire emission region: $F_{\text{tot}}^{\text{mod}}(\lambda) = \iint F(\lambda, \alpha, \delta) d\alpha d\delta$. For this model, the comparison to the observations was performed using the correlated fluxes and the total flux, because for this physical model, the precise flux values should match and not only the flux ratios. The correlated fluxes for the model were obtained by multiplying the modelled visibilities with the total flux of the model, *i.e.* $F_i^{\text{mod}}(\lambda) = V_i^{\text{mod}}(\lambda) \cdot F_{\text{tot}}^{\text{mod}}(\lambda)$. These could then be compared to the data. Again, the model parameters were optimised using the Levenberg-Marquardt least-squares minimisation. The χ^2 to be minimised is given as:

$$\chi^2 = \sum_{\lambda} \sum_{i=0}^{21} \left(\frac{F_i^{\text{obs}}(\lambda) - F_i^{\text{mod}}(\lambda)}{\sigma_{F_i^{\text{obs}}}(\lambda)} \right)^2. \quad (4.7)$$

where the sum over i is the summation over the 22 observed baseline orientations (21 baselines plus the total flux as a baseline with a baseline length of $BL = 0$ m). The $\sigma_{F_i^{\text{obs}}}(\lambda)$ are the errors of the correlated fluxes.

Two fits were performed: first the model was only optimised to fit the total flux (in the following "fit 1"). In this case, several parameters (r_1, r_2, f_1, f_2 and ϕ) were held fixed as they were degenerate. Then the model was fitted to the total data set including both the total flux and the 21 correlated fluxes ("fit 2"). In case of the fit of the total flux only, there is hence no summation over i in equation 4.7, as we simply had to use $i = 0$. The result of the fitting process is summarised in table 4.2.

A total of 21 wavelength bins were used for the fitting, so that fit 1 has $N_{\text{free}} = 21 \cdot 1 - 11 = 10$ degrees of freedom, while fit 2 has $N_{\text{free}} = 21 \cdot 22 - 11 = 451$. The resulting total fluxes for the two models are plotted in figure 4.3 in orange (fit 1) and red (fit 2) on top of the measured total flux. The correlated fluxes measured are compared to those from fit 2 in figure 4.11 at the two wavelengths already previously featured: 8.5 and 12.5 μm . This plot is the same

³Decoupling ϕ for the two components leads the fits to converge on a few dominant groups of visibility points only. This is the reason for keeping a single orientation angle for both components.

Table 4.2: Best fit parameters for the two component black body Gaussian models. The first column is for a fit of the total flux only (fit 1), the second column for a fit to both the total flux and the correlated fluxes (fit 2). The values in brackets were not fitted, but held fixed.

parameter	fit 1	fit 2
Δ_1 [mas]	23.6	21.1
r_1	(0.25)	0.21
τ_1	1.17	1.18
T_1 [K]	479.6	333.7
f_1	(1.00)	1.00
Δ_2 [mas]	279.0	96.7
r_2	(1.00)	0.97
τ_2	2.85	2.22
T_2 [K]	144.4	298.4
f_2	(1.00)	0.20
ϕ [°]	(60.0)	60.9
χ^2/N_{free}	0.56	36.86

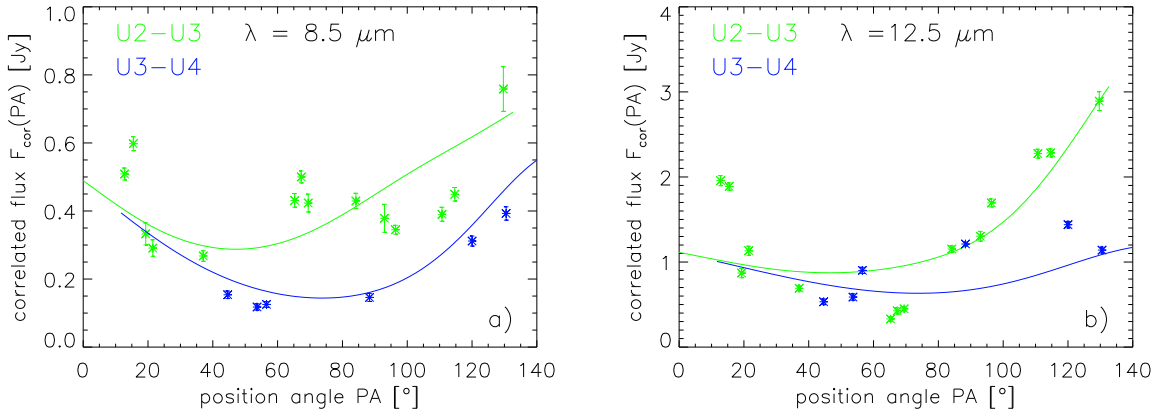


Figure 4.11: Comparison of the correlated flux of the physical model (fit 2) to the measured data for two distinct wavelengths: (a) 8.5 and (b) 12.5 μm . The measured fluxes are plotted with asterisks; the continuous lines are the modelled fluxes. Note the different flux ranges for the different wavelengths.

as that for the comparison of the geometrical model to the visibilities, except that now the correlated fluxes are compared. A comparison of fit 2 with all of the data, that is, the total flux and the 21 correlated fluxes dispersed from 8 to 13 μm , is given in figure 4.12.

The two components of this model have similar properties as those for the purely geometrical model: there is a smaller elongated component and a larger, round component. A sketch of the result of fit 2 is depicted in figure 4.13 and the flux distribution at 11 μm can be seen in figure 4.14. The smaller component has a FWHM of $\Delta_1 = 21$ mas, which corresponds to 0.4 pc at the distance of Circinus. It is highly ellipsoidal ($r_1 = 0.21$) and has a temperature of $T_1 = 334$ K. The distribution is found to be an optically thick black body ($f_1 = 1$). The second component is significantly larger, reflecting the fact that a large part of the flux ($\sim 90\%$) is resolved with our interferometric set-up. It has a FWHM of $\Delta_2 = 97$ mas, which corresponds to 2.0 pc, and it is found to have only a very small ellipticity and a temperature of less than 300 K. The component is a grey body with a covering factor of only 0.20. This

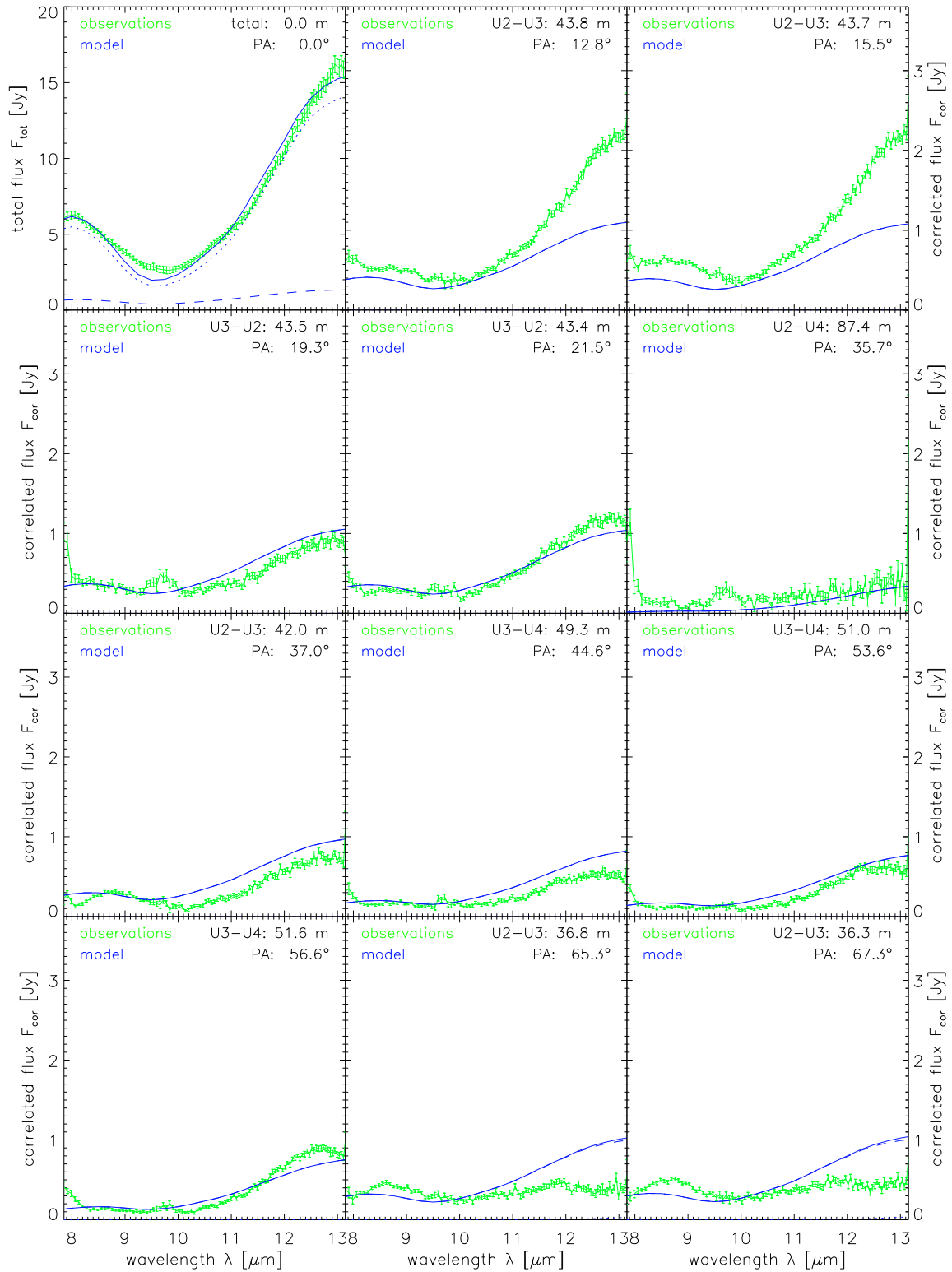


Figure 4.12: Comparison of the dispersed correlated fluxes (green) to the model fluxes for the physical model fit (fit2, blue) in the entire wavelength range from 8 to 13 μm . The dashed line represents the flux contribution of the small disk component, while the dotted line is the contribution of the large torus component.

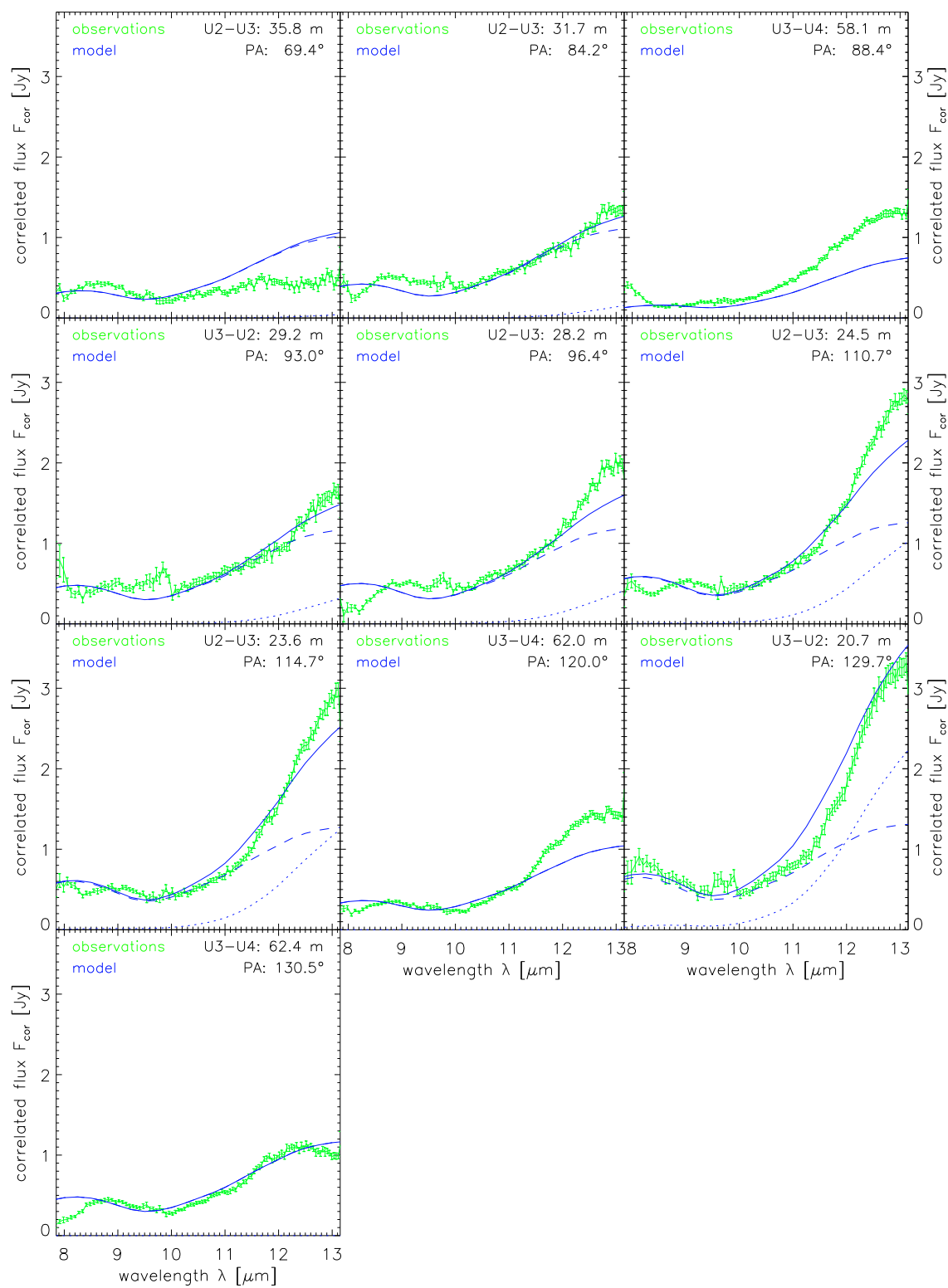


Figure 4.12: – continued –

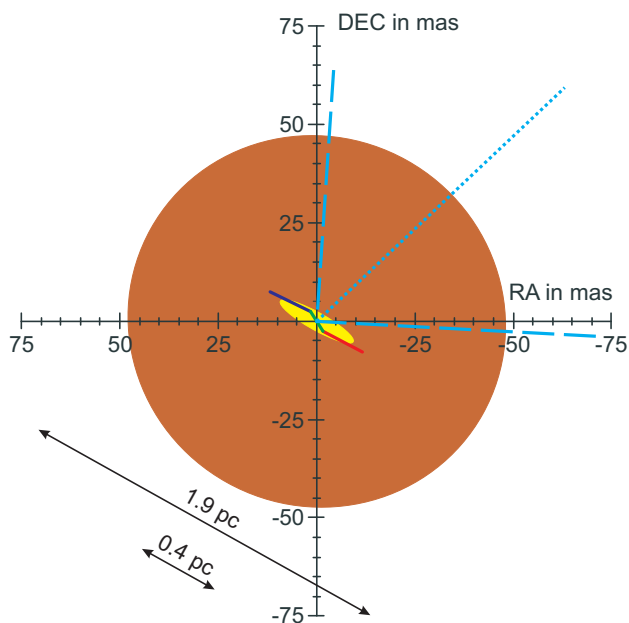


Figure 4.13: Sketch of the physical model (fit 2): a highly elongated warm emission region with a temperature of ~ 330 K (yellow) is surrounded by an extended, almost round and slightly cooler emission region with a temperature of ~ 300 K (brown). In the centre of the sketch, the locus of the H₂O maser emitters in a disk from Greenhill *et al.* (2003) is overplotted: the blue line to the north-east maps the receding masers and the red line to the south-west the approaching masers. The dashed light blue line traces the edge of the observed ionisation cone, the dotted line is the cone axis.

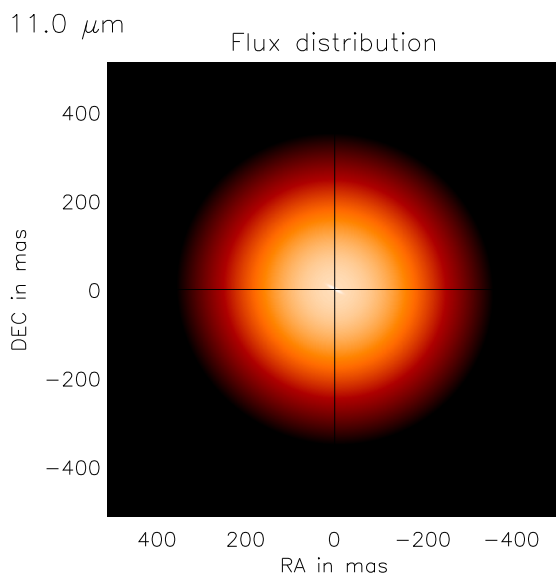


Figure 4.14: Flux distribution of the physical model (fit 2) at 11 μm in logarithmic scaling.

low covering factor allows an extended distribution of the flux, which is necessary to explain the low visibilities, while the integrated absolute flux of the component remains low and in accordance to the measured total flux values. For the fit of the total flux only, we see a larger temperature difference between the two components than when fitting all the data. In both cases, fit 1 and 2, the temperatures are the least constrained parameters. We therefore consider the 330 K for the inner component as a lower limit for the highest dust temperature and the 300 K as an upper limit for the cool component. Our data rules out a truly hot component with temperatures $T > 1000$ K, *i.e.* close to the sublimation temperature of the dust. This is consistent with Prieto *et al.* (2004), who also found no evidence for hot dust. The conclusion drawn from the growth of the size of the emitter with wavelength (section 4.4.2), namely that the temperature of the emitter decreases with increasing distance to the nucleus, is confirmed by the lower temperature of our larger component. The small component only contributes a minor fraction to the total flux. This can be seen in the top left graph of figure 4.12: the flux contribution by the extended component is delineated by a dashed line and that by the compact disk component by a dotted line. In contrast to the observations of NGC 1068 (Jaffe *et al.*, 2004; Poncelet *et al.*, 2006), the correlated fluxes in the Circinus galaxy do not show a relative increase of the flux to shorter wavelengths with respect to the flux at longer wavelengths. This shows that there is only a moderate increase of dust temperature towards the centre.

The model used here is a global model and hence the comparison with the data shows significant discrepancies. The reduced χ^2 of 37 indicates that deviations well above the 5σ -level are commonly found. The aim of our model was to extract the overall properties of the emitting source. The general behaviour of the correlated fluxes for the different baseline orientations can be well reproduced, but not the details. Looking at figure 4.11, the modelled fluxes only show a single “oscillation” in the range of position angles traced, due to the symmetry of the object when rotated by 180° . The measurements have considerably faster oscillations with changing position angle. The dispersed fluxes (figure 4.12) disagree strongest at the edges of the spectrum, at $8 \mu\text{m}$, where a downturn in several of our correlated fluxes is seen, or at $13 \mu\text{m}$, where the model deviates in both directions with respect to the data. The downturn at the short wavelength end, for example, explains the large discrepancy between the model and the data for the UT2 – UT3 baseline at $8.5 \mu\text{m}$ and for $90^\circ < PA < 120^\circ$ in figure 4.11 (a). As there are also small changes in the differential phase in these regions, we expect a further substructure of the source to be responsible for this unusual behaviour.

To verify this possibility, we undertook an additional experiment: we tried to reproduce the low covering factor of the larger component through clumpiness: instead of multiplying F_1 with the factor f_2 , an uneven surface $C(\alpha, \delta)$ was used. $C(\alpha, \delta)$ can be interpreted as a screen simulating clumpiness. To make the calculation consistent, the average value of C has to reproduce the covering factor: $\langle C(\alpha, \delta) \rangle = f_2$. The resulting flux distribution for such a clumpy model is shown in figure 4.15.

In such a simple experiment, it is possible to find clump distributions which trace the correlated flux much better (see for example figure 4.16). The reduced χ^2 can drop to values of $\chi^2/N_{free} < 25$. This supports the assumption that such deviations are generated by a substructure of the brightness distribution.

4.4.5 Other models

Apart from the geometrical shapes described above (namely elliptical Gaussians), we explored a multitude of other shapes in our models in order to match the data observed, for both the purely geometrical model as well as for the physical model. In both cases, we find that models

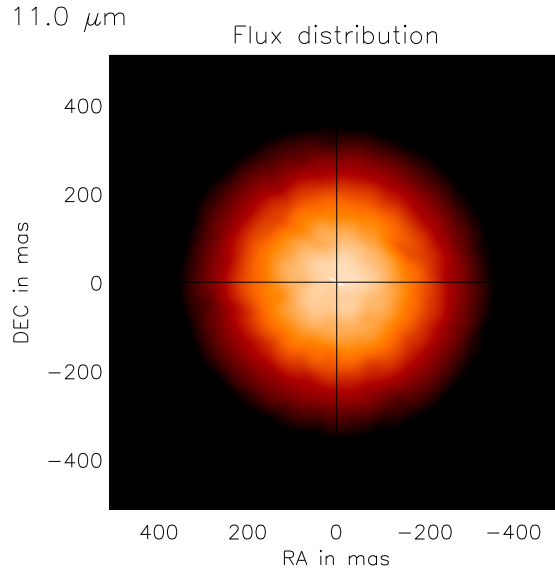


Figure 4.15: Flux distribution of the physical model with added clumpiness for the extended component at $11\ \mu\text{m}$ in logarithmic scaling.

including uniform disks produce results of similar χ^2 values as Gaussian distributions. The brightness distribution of such models has sharp edges. The same is true for models including point sources (*e.g.* representing the hot inner edges of the torus). Sharp edges have the great disadvantage that they produce oscillations in the uv plane: the uv plane is not uniform, but it has many minima and maxima in a quasi periodic pattern. Additionally, phase shifts occur at the minima in the uv plane.

Fitting such a model to the data, then first leads to a very general adjustment of the parameters, but the detailed outcome is highly ambiguous: the model parameters are optimised in such a way that the uneven uv plane best matches the few visibilities measured. This then depends on the individual configuration of the minima and maxima in the uv plane with respect to the position of the (few) visibility points measured. Different brightness distributions can lead to similar values of the visibility (or correlated flux) at these selected positions. For example, two point sources representing the hot inner edges of the torus result in a sinus wave in the direction of the two points in the uv plane. Increasing the distance of the point sources by a factor of two, doubles the frequency of the sinus wave in the uv plane. The larger and smaller spacings may then lead to similar visibilities at the few positions, where these can be compared to the data measured.

For this reason, we favoured uniform models with no sharp edges to describe our data. This restricts our conclusions to more general statements about the properties of the mid-infrared source of Circinus. However, we are confident that these properties are intrinsic to the source and neither an artefact of the specific model nor of the distribution of visibility points in the uv plane. To be able to make clearer statements about the detailed structure of the source, a more complete coverage of the uv plane is required and we are currently preparing to fill in the most obvious holes in the distribution of the visibility points, as far as this is possible with the baselines of the VLTI (see section 7.1.1).

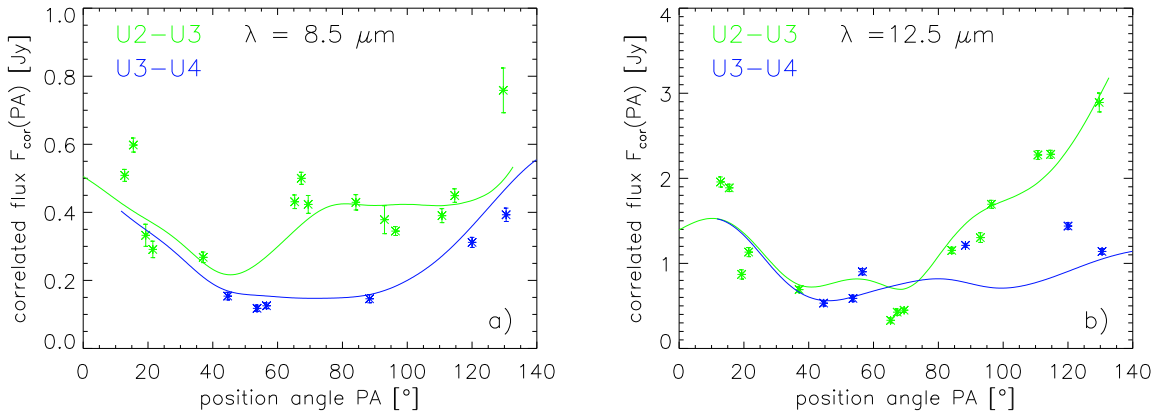


Figure 4.16: Correlated flux of the physical model with simulated clumpiness for the extended component: (a) 8.5 and (b) $12.5 \mu\text{m}$. The measured fluxes are plotted with asterisks; the continuous lines are the modelled fluxes. The clumpiness introduces significant changes in the correlated fluxes compared to the smooth model (see figure 4.11) which for certain clump configurations can lead to a significant decrease of the reduced χ^2 .

4.5 Discussion

The modelling of our interferometric observations reveals the presence of two components in the inner region of Circinus: an extended warm ($T_2 \sim 300 \text{ K}$) and round emission region showing strong silicate absorption and a smaller, slightly warmer ($T_1 \sim 330 \text{ K}$) and highly elongated emitter with a less pronounced silicate absorption feature. We interpret these two components as signs for a geometrically thick “torus” of warm dust and gas and a warmer, disk-like structure, respectively (see figure 4.17). The smaller and denser disk is seen at a high inclination and it partly exhibits the silicate band in emission. It is surrounded by the larger, less dense and clumpy torus component which gives rise to strong silicate absorption.

To understand the structure of the nuclear dust distribution in AGN, we developed hydrodynamical models of dusty tori (for a detailed description see Schartmann 2007). These models indeed also show a disk-like structure in the inner region which is surrounded by a geometrically thick “torus”. The torus is not continuous but has a filamentary structure (rather than clumpy) and the disk is turbulent.

In the following, we will develop a picture of the central parsec region in Circinus which aims to explain the results of the MIDI measurements in the context of the hydrodynamical model. In addition, the picture needs to be consistent with the previously known properties of this galactic nucleus.

4.5.1 Extinction

For the interpretation of the nuclear emission from Circinus and the silicate absorption in the torus, we need to reliably estimate the foreground extinction. Radiation from the nuclear region of Circinus suffers extinction from two main foreground absorbers: our own galaxy (Circinus is located at a galactic latitude of $b = -4^\circ$) and the intrinsic absorption in the galactic disk of the Circinus galaxy.

By observing the reddening of several stars in the vicinity of Circinus, Freeman *et al.* (1977) estimate the visual extinction due to our own galaxy to be only $A_V = 1.50 \pm 0.15 \text{ mag}$, as Circinus lies in a window of low galactic extinction. The extinction towards the nuclear

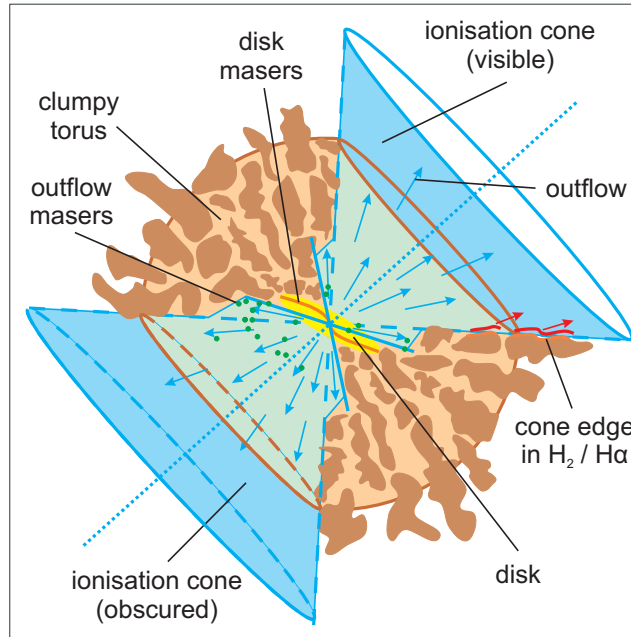


Figure 4.17: Sketch of dusty torus in the central parsec-sized region of the Circinus galaxy derived from the interferometric observations in the MIR.

region within Circinus itself is much less constrained and estimates from near-infrared colors vary from $A_V = 6$ mag for a foreground screen to $A_V = 20$ mag for a mix of dust and stars (Prieto *et al.*, 2004; Mueller Sánchez *et al.*, 2006). The near-infrared observations which underlie this estimate probe a region on scales of less than 10 pc distance from the nucleus. Taking into account the presence of a nuclear starburst (Mueller Sánchez *et al.*, 2006), we understand the values for a mix of dust and stars to be more realistic. By consequence, we assume the extinction by the foreground dust on the line of sight between us and ~ 2 pc from the nucleus to be $A_V \sim 20$ mag.

From the optical depth of the silicate feature for our large component, we can estimate the extinction towards those regions of the torus where the warm dust emission arises. Our value of $\tau_2 \sim 2.2$ is at the lower end of the values found by Roche *et al.* (2006), who cite a range of $2.2 \leq \tau_{\text{SiO}} \leq 3.5$, depending on where they extract the spectrum along their slit. We also have to take into account that, due to the low spectral resolution of MIDI, the minimum of the absorption trough is washed out. This automatically leads to lower optical depths. We therefore consider the two values to be in good agreement, although our observations rule out $\tau_{\text{SiO}} > 3.0$ for the nucleus. In the following, we will assume $\tau_{\text{SiO}} = 2.5$ towards the larger torus component with 1 pc radius.

From the wavelength dependency of the mass extinction coefficient (as calculated for example in Schartmann *et al.*, 2005), we read off the ratio of the optical depth in the visible (V at 548 nm) to that at the maximum of the silicate feature (at $9.5 \mu\text{m}$): $\tau_V = 12.2 \cdot \tau_{\text{SiO}}$. Hence, the absorption in the visual is $A_V = 1.09 \cdot \tau_V = 13.3 \cdot \tau_{\text{SiO}}$. For $\tau_{\text{SiO}} = 2.5$, we obtain $A_V = 33$ mag, which means that there are an additional 11 mag of extinction towards the torus region compared to that derived from the near-infrared colours. Most likely, the extinction towards the accretion disk itself is even higher.

In contrast to the MIDI observations of NGC 1068 (Jaffe *et al.*, 2004; Poncelet *et al.*, 2006), we do not observe a further increase of the silicate absorption feature when zooming into the nucleus with our interferometric observations. Instead, the absorption feature appears to be

less pronounced in the correlated fluxes, which can also be inferred directly from the convex shape of the visibilities (*e.g.* from figure 4.4). In general, the silicate feature is expected to appear in emission for lines of sight, where the (appropriately high) temperature decreases away from the observer. This is the case for the directly visible inner rim of the torus and, therefore, expected and observed for Seyfert 1 objects. In the opposite case (cold dust on the line of sight), the silicate feature will appear in absorption, as seen in Seyfert 2 objects. A decrease of the silicate feature in absorption therefore means that more and more of the Seyfert 1 type silicate emission is able to shine through the torus body. These findings are in accordance with the detection of a hidden Seyfert 1 nucleus in Circinus, a fact also suggested by the observation of broad emission lines in polarised light (Oliva *et al.*, 1998).

In summary, we conclude that the obscuration on our line of sight towards the inner parsec of Circinus is composed of the following three extinction components: extinction by our Milky Way, $A_V(\text{MW}) = 1.5$ mag, by the foreground dust within Circinus, $A_V(\text{disk}) = 20$ mag, and by the nuclear dust, $A_V(\text{nuclear}) = 11$ mag.

4.5.2 Energy budget

The energy emitted by the source in the N band can be estimated by integrating under the dereddened spectrum. The integration under the total flux measured by MIDI gives a luminosity in the N band of $L_{7.5-13.5\mu\text{m}} = 1.3 \cdot 10^9 L_\odot = 5.1 \cdot 10^{35}$ W.

To estimate the total luminosity of the dust emission, we integrate under the flux of our physical model (fit 2) from $\nu = 0$ to ∞ without applying any absorption, that is $\tau_1 = \tau_2 = 0$. Orientation effects only significantly affect the smaller disk component. A correction by assuming oblate spheroids seen edge-on leads to an increase of the flux by about 20%. With this method, we obtain a total luminosity from the dust of $L_{\text{dust}} = 4.1 \cdot 10^9 L_\odot$. This is four times more than the luminosity measured in the N band alone. Integrating under the dereddened (for $A_V = 24$ mag) Spitzer spectrum ($5\mu\text{m} < \lambda < 37\mu\text{m}$) gives a luminosity of $L_{\text{Spitzer}} = 7.6 \cdot 10^9 L_\odot$, which is consistent with our result when considering the contribution by the nuclear starburst included in the larger aperture of Spitzer. Considering that we have not traced the contribution by dust at $T \lesssim 150$ K, we round our value up to $L_{\text{dust}} \sim 5 \cdot 10^9 L_\odot$ as our best estimate for the luminosity of the nuclear dust at $r < 2$ pc in the infrared.

We can take this value to estimate the luminosity of the accretion disk, L_{acc} , which we hold responsible for heating the dust. In doing so, we have to take into account that not all of the accretion luminosity is available for heating the torus (see discussion in section 4.5.3). A significant fraction of L_{acc} will escape along the directions of the ionisation cones. With an opening angle of 90° (Veilleux and Bland-Hawthorn, 1997; Wilson *et al.*, 2000), the total solid angle covered by the torus, as seen from the centre, is $2\sqrt{2}\pi$. This corresponds to about 0.7 of the full sphere. Assuming a radiation characteristic for an optically thick accretion disk which is proportional to $\cos\theta$, about half of the radiation is emitted in direction of the dust in the torus. That is, only half of the energy can be reprocessed and radiated in the infrared. If we thus assume $0.5 \cdot L_{\text{acc}} \sim L_{\text{dust}}$, this leads to a luminosity of the central energy source of $L_{\text{acc}} \sim 10 \cdot 10^9 L_\odot$.

Consistent with our estimate, Moorwood *et al.* (1996) also report the flux of the nucleus to be $\sim 10 \cdot 10^9 L_\odot$. Their integration under the UV bump yields the same flux as we observed in the MIR: $L_{\text{UV}} = 5 \cdot 10^9 L_\odot$. Oliva *et al.* (1999) cite a total ionising radiation of the nucleus on the order of $L_{\text{ion}} = \frac{1-4 \cdot 10^{10}}{\sin^2 i} L_\odot$, where i is the inclination angle of the ionisation cone with respect to our line of sight. For $i > 60$ (Elmoultie *et al.*, 1998), this translates into $10 - 70 \cdot 10^9 L_\odot$. Luminosities of the AGN in Circinus significantly higher than $10 \cdot 10^9 L_\odot$ can be ruled out, as this would imply a higher MIR flux than we observed. The currently

derived intrinsic 2 to 10 keV luminosities of the nuclear X ray source are all below $5 \cdot 10^8 L_\odot$, which is well below the energy needed to heat the dust. The dust is mainly heated by soft X rays and UV radiation rather than by radiation in the 2 to 10 keV band alone.

Finally, we can compare our luminosity estimate for the accretion disk to the Eddington luminosity. For a black hole with a mass of $M_{\text{BH}} = 1.7 \cdot 10^6 M_\odot$, this luminosity is $L_E = 56 \cdot 10^9 L_\odot$. With our value of $L_{\text{acc}} \sim 10 \cdot 10^9 L_\odot$, we find Circinus to accrete at 18% of its Eddington luminosity.

4.5.3 Temperature dependency and clumpiness

Less than a parsec from this central energy source, the dust is most likely heated by the active nucleus alone and not by a homogeneous energy input, such as by a starburst. The discussion of the energy budget of the nucleus has shown that no further energy source is necessary. A heating by a nuclear energy source is also suggested by the decrease of the dust temperature to the outside.

The temperature decrease we observe is, however, very shallow and the temperature of our large component is relatively high considering the distance of its dust to the heating source: the dust has a temperature of ~ 300 K out to distances of 1 pc from the nucleus. To investigate the implications of this finding on the properties of the dust distribution, we compare the dust temperature in Circinus to the temperature expected for a direct illumination of the dust and to the temperature inferred from our radiative transfer modelling of continuous and clumpy AGN tori. The various temperature dependencies are shown in figure 4.18 and we will discuss them one by one in the following.

Assuming a naive radiation equilibrium, the temperature of a dust particle at the distance r from the illuminating source with the luminosity L_{acc} is given by

$$T_{\text{N}}(r) = 194 \left(\frac{L_{\text{acc}}}{r^2} \frac{\text{pc}^2}{10^{10} L_\odot} \right)^{1/4} \text{ K.} \quad (4.8)$$

Taking into account the absorption and emission characteristics of the dust grains leads to a more realistic description of the temperature dependency (Barvainis, 1987). For emission in the infrared, the temperature dependency then reads:

$$T_{\text{B}}(r) = 624 \left(\frac{L_{\text{acc}}}{r^2} \frac{\text{pc}^2}{10^{10} L_\odot} \right)^{1/5.6} \text{ K.} \quad (4.9)$$

The two temperature dependencies $T_{\text{N}}(r)$ and $T_{\text{B}}(r)$, calculated for $L_{\text{acc}} = 8 \cdot 10^9 L_\odot$, are plotted by a green dashed line and a green continuous line respectively. The realistic case leads to significantly higher temperatures than the naive case, as the individual dust particles reradiate the energy less effectively than a black body. Here, we have not taken into account the anisotropic radiation characteristic of the central energy source, the accretion disk, which emits less energy in direction of the dust distribution than in direction of the ionisation cones (see section 4.5.2). This leads to a lower temperature of the dust near the plane of the disk, so that $T_{\text{B}}(r)$ should be considered as an upper limit for the dust temperature at a certain radius.

In the case of a continuous dust distribution, the temperature is expected to drop steeply outside the inner funnel of the torus, where the dust is directly illuminated by the central source. The dust at larger radii is shielded from the nuclear light and by consequence only reaches lower temperatures. For a clumpy torus, the temperature dependency should be somewhat intermediate between the continuous case and the radiation equilibrium for totally

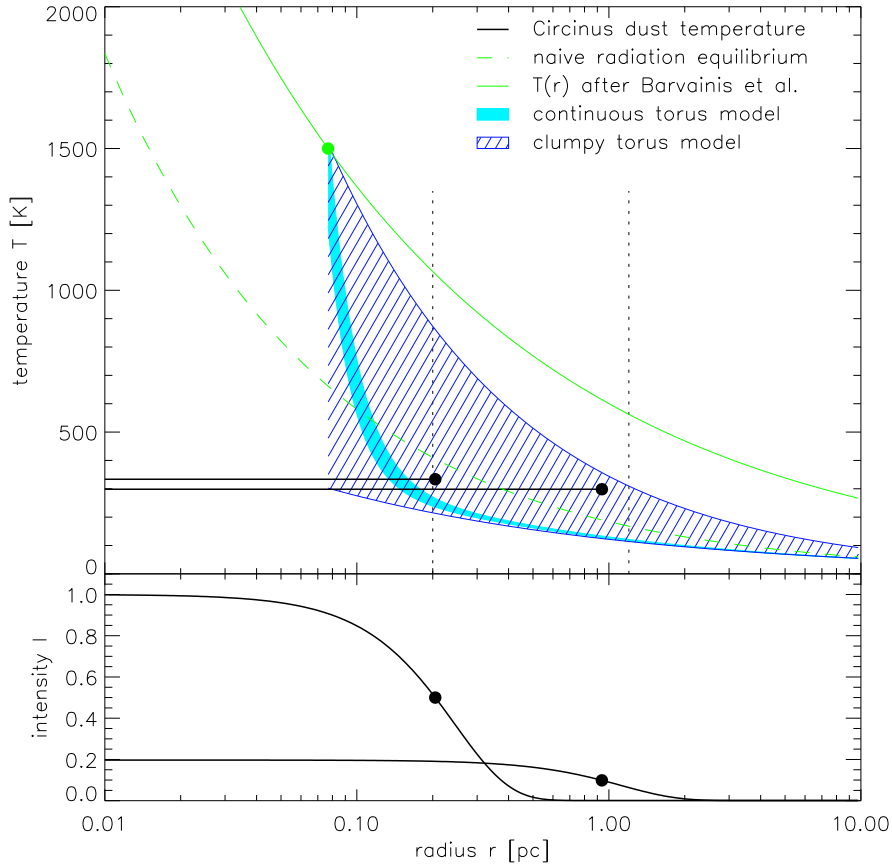


Figure 4.18: Comparison between the radial temperature distribution of our simple “physical” model (thick black continuous lines) and the temperature distributions for a clumpy (hatched area) and continuous torus (light blue) as well as for dust directly illuminated by the central energy source (green). The point where the sublimation temperature of the dust, $T_B(r) = 1500$ K, is reached is marked by a circle. The lower part of the graph shows the intensity of the Gaussian components (depending on the covering factor f). The HWHM of the Gaussian components are marked by circles. The scales probed by our interferometric set-up lie within the dotted vertical lines.

unobscured lines of sight, that is, $T_B(r)$. The behaviour is reproduced by the radiative transfer modelling of AGN tori: the shaded areas show the temperature ranges (from mean to maximum temperature) of the individual cells in a continuous and a clumpy torus model (for a detailed description of the modelling we refer to Schartmann *et al.*, 2007). For this purpose, the radii were rescaled so that the inner radii of the torus, where the sublimation temperature is reached, coincide with the sublimation radius predicted by $T_B(r)$. As expected, the continuous model (filled, light blue area) has a very strong drop in the temperature behind the inner edge of the dust distribution, while the clumpy model (dark blue, hatched area) has a much wider temperature range, including lower temperature clouds at small distances from the nucleus and higher temperatures at larger distances.

Finally, the thick black continuous lines trace the temperatures of the two dust components in Circinus. The lines are drawn out to the half width at half maximum (HWHM) of the respective component. From the figure it is obvious that the temperatures seen by MIDI disagree with a continuous dust distribution as the temperatures lie significantly above the distribution and no sharp temperature rise to the centre is seen. The high temperatures at

large distances from the nucleus can only be achieved when clouds also at larger distances have free lines of sight to the heating source. As the temperatures lie within the temperature range for a clumpy dust distribution, we conclude that the dust must be distributed in a clumpy medium. All our temperatures lie below those of $T_B(r)$, as expected for partial shadowing of the clouds.

There are several further indications for an non-continuous distribution of the dust in our data:

First, we interpret the low filling factor of the large component in our physical model to be evidence for an inhomogeneity of the emitting dust. The only way for thermal emission of warm dust ($T \sim 300$ K) to be as extended as we observe it with our interferometry, while at the same time being consistent with the total flux of the source, is by a patchy emission.

The most compelling evidence, however, comes from the behaviour of the correlated fluxes (a) with wavelength or (b) with changing baseline (for the sake of simplicity we will only refer to the correlated fluxes F_{cor} in this paragraph, nevertheless the same statements are true for the behaviour of the visibilities V). The behaviour observed cannot be explained by a smooth brightness distribution.

First let us consider the set of all visibility points observed at a single wavelength, *i.e.* $F_{\text{cor},\lambda}(PA)$. In this case, the need for clumpiness becomes obvious comparing figure 4.11 with figure 4.15, as was already discussed in section 4.4.4. We have also compared the variations we observe in our data to those that can be seen in the correlated fluxes of our clumpy radiative transfer models (Schartmann *et al.*, 2007): when we calculate the correlated fluxes of such a torus model for different position angles, $F_{\text{cor},\lambda}(PA)$, we obtain variations of up to 50% of the flux, similar to those shown in figure 4.15. The variations become stronger for longer baselines, where substructures are better resolved.

Similarly, the need for a clumpy structure becomes obvious when considering the individual visibility points at different wavelengths, that is, the dependence of the correlated flux over the N band, $F_{\text{cor},PA}(\lambda)$. In this case, we observe wiggles in the correlated fluxes that can only be reproduced by a substructure, *e.g.* the downturn at $\lambda > 12 \mu\text{m}$ for $BL \sim 36$ m, $PA \sim 67^\circ$ (see figure 4.12).

An inhomogeneous dust distribution complicates the problem of determining the morphology of the source significantly, when interferometric methods are used. With the current uv coverage, we are not able to say anything about the details of the clump distribution of the source. More data are needed to disentangle these and also to enable us to trace how the morphology changes with the wavelength.

4.5.4 Orientation and geometry of the dust distribution

Both direct inspection of the data (see figure 4.4) and our modelling reveal that the source is elongated in direction of $PA \sim 60^\circ$. This effect is dominated by our observations with longer baselines (UT3 – UT4); the shorter baseline observations (UT2 – UT3) do not show a clear orientational preference. In our interpretation, this means that the inner component is more disk-like, while the outer component traces an almost spherical component.

The orientation of our disk component is in very good agreement with the orientation of several components in this AGN which are directly related to the nuclear dust distribution: its axis coincides with the direction of the ionisation cone, which points towards $PA = -44^\circ$ (Maiolino *et al.*, 2000; Wilson *et al.*, 2000) and the bidirectional outflow observed in CO pointing towards $PA = 124^\circ$ and $PA = -56^\circ$ (Curran *et al.*, 1998). Our measurements are hence the first direct confirmation for the presence of a dust structure extended perpendicularly to

the outflow and the ionisation cone in an AGN without taking any previous knowledge on the source into account.

The nucleus of Circinus is special in another feature: it displays a very strong emission of water vapour masers. This emission was first detected by Gardner and Whiteoak (1982). A detailed study was performed by Greenhill *et al.* (2003): The VLBI observations of the $6_{16}-5_{23}$ transition of H_2O show an S shaped locus and a wider distribution of maser sources at the nucleus of the Circinus galaxy. The authors attribute the sources detected to two distinct populations: a warped, edge-on accretion disk and a wide angle outflow. The warped disk has an inner radius of (0.11 ± 0.02) pc and extends out to ~ 0.4 pc. These are the only observations at the same or even better spatial scale as ours. An almost perfect alignment is found between the outer radius of the maser disk with a position angle of $PA = 56 \pm 6^\circ$ (Greenhill *et al.*, 2003) and our disk component (*c.f.* Figures 4.13 and 4.12).

Because of the high axis ratio of $r_1 = 0.21$, our observations suggest a high inclination of the smaller disk component with respect to the plane of the sky: $i_{\text{disk}} > 60^\circ$. Our model is also consistent with an edge-on disk ($i = 90^\circ$), which then has to be warped or has to have a thickness of $h/r = r_1$ to appear as we observe it. When observed edge-on, the maser disk with a warp of 27° can easily produce the same extent as observed for our smaller component. Considering this and the good agreement of the position angles, we believe the maser emission originates in the dense dusty and molecular medium associated with our disk component.

From the present data, we cannot make any detailed statements concerning the shape of the larger torus component, as its proportions are not very well constrained. It must be significantly extended also in the direction of the ionisation cone and the measurements are consistent with an almost circular dust distribution when seen in projection. When seen almost edge-on, this implies $h/r \sim 1$. The component can, however, not be entirely spherical but it must have an opening angle of 90° for the ionisation cones (see figure 4.17). From our side on viewing position, we see a projection of this hollowed spherical dust structure, which leads to its almost circular appearance. More measurements at shorter baselines are necessary to provide better constraints on the distribution of the more extended dust emission.

4.5.5 Collimation of the ionisation cone and outflow

In the context of the two components, namely the disk and the torus, it is interesting to address the question which component causes the collimation of the outflow and the ionisation cone. The latter has an opening angle of 90° and a sharp boundary seen clearest in [O III] and $\text{H}\alpha$ (Wilson *et al.*, 2000). The same opening angle is found for the extended X-ray emission, overlapping with the ionisation cone (Smith and Wilson, 2001) as well as for the CO outflow (Curran *et al.*, 1999). Finally, the high ionisation lines in direction of the ionisation cone reported by Maiolino *et al.* (2000) ([Si VI]) and Prieto *et al.* (2004) ([Si VII]) show an even smaller opening angle. Summarised, this means that at scales > 2 pc only 30% of the solid angle are exposed directly to the nuclear engine. This cannot be explained by the $\cos\theta$ radiation characteristic of the accretion disk, especially considering the sharp boundaries of the cone. On scales less than 1 pc, Greenhill *et al.* (2003) found a wide angle outflow of maser emitters. It is supposed to cover 80 to 90% of the solid angle, corresponding to an opening angle of 120° . This is consistent with a collimation of the outflow by a disk with a warp of 27° . This leads to the conclusion that the large torus component extending from ~ 0.2 to 1.0 pc must be responsible for the further collimation of the wide angle outflow to the narrow one observed at larger scales (see figure 4.17).

Further support for this picture comes from the observation of molecular hydrogen gas just below the ionisation cone on scales from 6 pc (Mueller Sánchez *et al.*, 2006) up to 20 pc

(Maiolino *et al.*, 1998, 2000). This gas most likely is part of the cooler regions of the dusty torus. Once clouds enter the ionisation cone and are directly irradiated by the central source, they emit $H\alpha$ and $[\text{Si VI}]$ emission, which is observed in the ionisation cone and which is especially strong on its southern edge. The clouds are then accelerated and entrained by the outflow (for a more detailed discussion, see Packham *et al.* 2005).

As an alternative to the thick toroidal dust distribution in unified models, warped disks are often put forward. Fully in line with this, Greenhill *et al.* (2003) have claimed that the warped disk alone may be responsible for the obscuration of the nuclear source and for the collimation of the outflow in Circinus, obviating the need for a geometrically thick dust distribution. Our observations, however, have added the decisive component: they have proven that a geometrically thick dust distribution is indeed present in the nucleus of Circinus. Furthermore, it is obvious that the opening angle observed at larger scales is too narrow to be produced by merely a disk with a warp of 27° . Hence the disk component cannot be the source of the collimation for the outflow and ionising radiation alone.

From our observations we cannot say anything about cooler dust, with temperatures $T < 100$ K, and it is likely that the structure we observe is embedded in a larger component of cool gas and dust extending out to the starburst on scales of 10 pc.

4.5.6 Dust properties

The MIDI data agrees with the dust absorption in Circinus to be of the same type as the interstellar absorption observed towards the nucleus of our own galaxy (section 4.4.4), *i.e.* the dust composition is the same. This is in agreement with Roche *et al.* (2006) who found Trapezium type dust absorption in their total spectrum. This implies that the dust is composed of a mixture of 15% amorphous pyroxene and 85% of amorphous olivine by mass, with grain sizes less than $0.1 \mu\text{m}$ (Kemper *et al.*, 2004). In fact, there is no evidence for the presence of any crystalline silicates in the nucleus of Circinus. This indicates that the dust must originate to a large degree from the interstellar medium in the galaxy, assuming standard timescales for the amorphitisation in the order of several Myrs. Local formation of the dust by stellar ejecta and supernovae of the starburst would lead to a crystalline fraction of at least 3%, which should lead to a detectable change of the silicate absorption profile. The dust production of the nuclear starburst thus cannot be the main dust supplier. On the other hand, there seems to be no significant dust processing in the torus itself, as might be expected to happen in the radiation field of the accretion disk. The result is interesting compared to that found for NGC 1068, where the dust absorption towards the nucleus clearly does not agree with the standard intergalactic absorption profile (Jaffe *et al.*, 2004; Poncelet *et al.*, 2006). This in turn suggest dust processing in the torus. Concerning the dust types, there seems to be no clear cut picture among Seyfert galaxies.

4.6 Conclusions

We have obtained interferometric observations of the nucleus of the Circinus galaxy covering a wavelength range from 8.0 to $13.0 \mu\text{m}$. Through direct analysis of the data and several steps of modelling with increasing complexity, we have extracted the following new information on the nuclear dust in this active nucleus:

1. The dust is distributed in two components:
 - (a) a dense and warm ($T_1 = 330$ K) disk component with a radius of 0.2 pc and

- (b) a less dense and slightly cooler ($T_2 = 300$ K) geometrically thick torus component extending out to 1 pc.
2. This disk-torus configuration is in perpendicular orientation to the ionisation cone and outflow and it coincides with the orientation of the maser disk, which we directly associate with our disk component.
 3. From the total energy needed to heat the dust, we infer a luminosity of the accretion disk on the order of $L_{\text{acc}} = 10 \cdot 10^9 L_{\odot}$, which corresponds to $\sim 20\%$ of the Eddington luminosity of the nuclear black hole.
 4. The properties of the larger torus component are less constrained. With an $h/r \sim 1$, it is consistent with a edge-on spherical structure which has cavities for the ionisation cone and outflow. This component is responsible for collimating the radiation and the wide angle outflow ($> 120^\circ$) originating in the nucleus to the observed opening angle of the ionisation cone and outflow of 90° at larger distances.
 5. We find strong evidence for clumpiness of the torus from three lines of evidence:
 - (a) The large component only has a low effective filling factor.
 - (b) The visibility measurements show an irregular behaviour that can be explained by clumpiness.
 - (c) The temperature drop-off of the dust, $T(r)$, has a shallow decrease requiring free lines of sight towards the nucleus on scales of a parsec.
 6. The silicate absorption depth is less pronounced for the disk component than for the extended component giving evidence for the silicate feature in emission in the innermost regions of the dust distribution.
 7. The silicate absorption profile is consistent with that of normal galactic dust. We hence see no evidence for dust reprocessing.

Chapter 5

MIDI Interferometry of Centaurus A¹

5.1 Introduction

At 3.83 Mpc distance (Rejkuba, 2004)², Centaurus A (NGC 5128, see figure 5.1) is the closest active galaxy. Its activity was first noticed at radio frequencies (Bolton *et al.*, 1949), where it is one of the brightest and largest objects in the sky, extending over about $8^\circ \times 3^\circ$ (Junkes *et al.*, 1993). An inner system of radio jets and lobes, about 12 arcmin in size (Clarke *et al.*, 1992) has also been detected in X-rays (Döbereiner *et al.*, 1996; Hardcastle *et al.*, 2003). The source of this large scale activity is an active galactic nucleus (AGN) in the centre of an elliptical galaxy, which is undergoing late stages of a merger event with a spiral galaxy (Baade and Minkowski, 1954). The core of Centaurus A is heavily obscured by the dust lane of the spiral and becomes visible only at wavelengths longwards of $0.8 \mu\text{m}$ (Schreier *et al.*, 1998; Marconi *et al.*, 2000). It harbors a supermassive black hole, the mass of which has recently been determined from the velocity field in a circum-nuclear gas disk to be $M = 6 \cdot 10^7 M_\odot$ (Häring-Neumayer *et al.*, 2006). See Israel (1998) for a comprehensive review of the general properties of Centaurus A.

The proximity of Centaurus A offers unique opportunities to look into the very core of an AGN, as 1 parsec corresponds to 53 mas. Despite this fact, single-telescope observations have not been able to resolve the core at any wavelength: at short wavelengths ($\sim 1 \mu\text{m}$) the upper limit for its size is about 100 mas (1.9 pc). Radio interferometry with VLBI networks reveals a core-jet structure within the central parsec: the well-collimated radio jet can be traced over > 60 mas at $\lambda = 6$ cm (Tingay *et al.*, 1998). Also a counter-jet is clearly detectable. Nevertheless, the radio core (with inverted spectrum $S_\nu \sim \nu^2$ between 6 and 1 cm) is hardly resolved even with millimeter VLBI: at 43 GHz, Kellermann *et al.* (1997) find an angular diameter (FWHM) of 0.5 ± 0.1 mas (0.01 pc).

The nature of the near- and mid-infrared emission from the parsec-size core of Centaurus A remains a matter of debate. Although several authors (*e.g.* Bailey *et al.* 1986; Turner *et al.* 1992; Chiaberge *et al.* 2001) have argued that high frequency synchrotron radiation might be an important contribution to the emission, others assume that the extremely red near-infrared colors of the unresolved core hint at the existence of a hot, AGN-heated dust structure (see Israel 1998 and references therein), which has been postulated to exist in the central parsec of more luminous AGN and has recently been resolved by mid-infrared interferometry of nearby Seyfert 2 galaxies (chapter 4; Jaffe *et al.* 2004; Ratzka *et al.* 2006; Tristram *et al.*

¹Adapted from Meisenheimer *et al.* (2007), accepted for publication in A&A.

²Recent distance measurement of Centaurus A range between 3.4 and 4.2 Mpc with typical uncertainties of $\pm 10\%$.

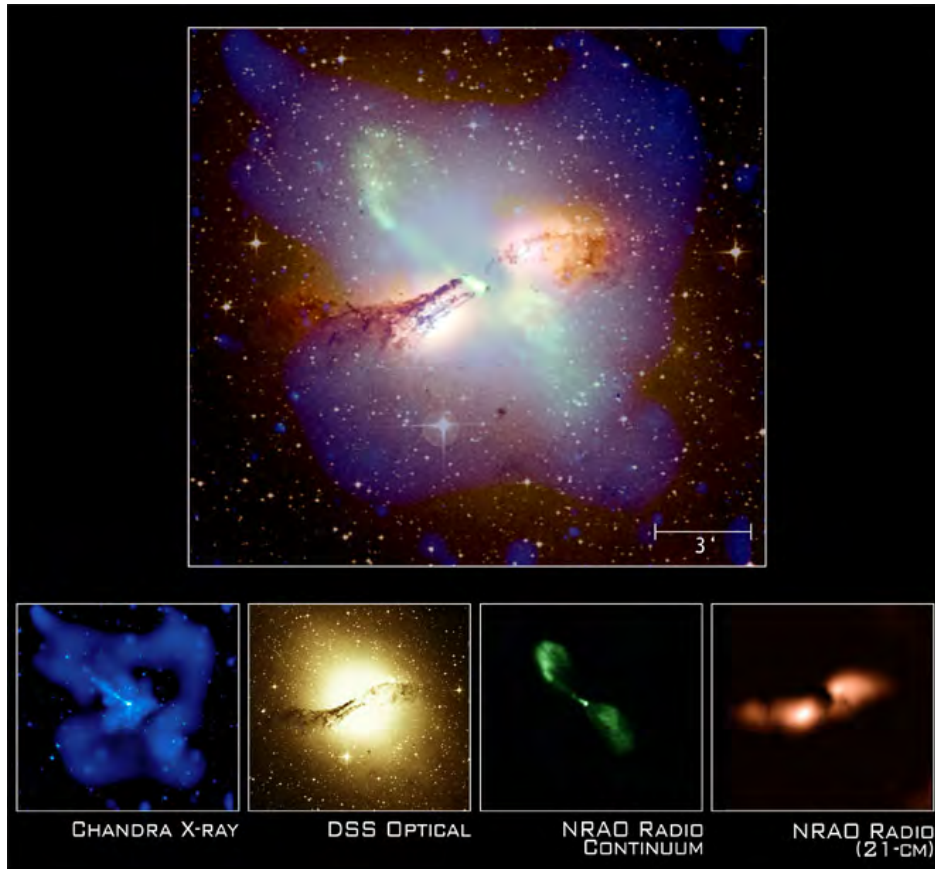


Figure 5.1: Composite image (top panel) of the galaxy Centaurus A, made up of the individual images shown in the bottom row: X-ray (blue), optical (stars, orange and yellow), radio continuum (synchrotron radiation, green) and 21 cm line (H_2 , pink). (Credits: X-ray: NASA/CXC/Karovska *et al.*, 2002; Optical: Digitized Sky Survey U.K. Schmidt Image/STScI; Radio continuum image: NRAO/AUI/NSF/Condon *et al.*, 1996; Radio 21-cm image: NRAO/AUI/NSF/Schiminovich *et al.*, 1994.)

2007). In order to resolve the core emission on sub-parsec scales, interferometric observations are mandatory. In this chapter, we will report on the first high-frequency interferometry of Centaurus A.

5.2 Observations

5.2.1 Interferometric observations and data reduction

The interferometric observations of Centaurus A were obtained with MIDI during two nights of guaranteed time on 2005 Feb 28 and 2005 May 26, which were also used for the observation of Circinus (see section 4.2.1). The log of the interferometric observations is given in table 5.1. We used two telescope combinations with a roughly orthogonal configuration: UT3 – UT4 and UT2 – UT3.

At both telescopes, the wavefront was corrected using the adaptive optics system MACAO. The standard settings for the chopping frequency, $f = 2$ Hz, the chopping angle, $\alpha = 0$, and the chopping throw, $\delta = 15$ arcsec, were used. The short wave N band filter at $8.7 \mu\text{m}$ and an exposure time of 4 ms were used for the acquisition images. To obtain a clear detection of

Table 5.1: Log of the MIDI observations of Centaurus A and the calibrator HD 112213. The derived correlated flux (averaged over $\pm 0.2 \mu\text{m}$) is given for two wavelengths, least affected by the silicate absorption.

Date: Telescopes Target	LST [hour]	Baseline		Resolution ^a [mas]	Correlated flux at	
		length [m]	PA [°]		$\lambda = 8.3 \mu\text{m}$ [Jy]	$\lambda = 12.6 \mu\text{m}$ [Jy]
28 Feb 2005:		UT3 – UT4				
Cen A	12:02	58.2	96	14.8	0.45 ± 0.04	0.73 ± 0.05
HD 112213	12:26	61.3	105	14.0		
Cen A	14:24	62.4	120	13.6	0.34 ± 0.05	0.60 ± 0.05
HD 112213	14:50	61.1	130	13.9		
26 May 2005:		UT2 – UT3				
Cen A	11:53	46.5	27	18.2	0.66 ± 0.04	0.91 ± 0.06
HD 112213	12:44	45.5	40	17.7		
Cen A	14:05	44.1	46	19.2	0.76 ± 0.04	1.01 ± 0.06
HD 112213	14:32	41.5	54	20.4		

^aResolution $\lambda/2B$ at $\lambda = 8.3 \mu\text{m}$.

the nucleus of Centaurus A, a total of 3000 to 5000 exposures had to be taken. For the fringe tracks on Feb 28, the integration time per frame was $\text{DIT} = 12 \text{ ms}$, which was increased to $\text{DIT} = 18 \text{ ms}$ for the second observation on May 26. We took $\text{NDIT} = 8000$ frames per fringe track on Feb 28, and $\text{NDIT} = 5000$ on May 26. For all of the observations, we used the offset tracking mode, at an offset of $50 \mu\text{m}$ from 0 OPD. The integration time during photometry of Centaurus A was 12 ms, and the total number of photometry frames was increased from 4000 in the first measurement in February to 10000 frames for the measurements in May. The calibrator associated with the observations of Centaurus A was HD 112213.

All interferometric and photometric data were reduced with the EWS package (see section 3.2). For the observations of Centaurus A, the best sky subtraction – that is, the most consistent total flux for all four independent measurements – was obtained when using two sky windows located at 0.39 arcsec to 0.90 arcsec above and below the object spectrum, respectively. The calibrated flux densities of Centaurus A were derived using a spectrum of HD 112213, based on a template fit to five band photometry by Roy van Boekel, (*private comm.*).

5.2.2 Additional single-telescope observations

To understand the nature of the mid-infrared emission in Centaurus A, the interferometric data were supplemented by measurements at lower and higher frequencies, using millimeter and near-infrared data.

Near-infrared photometry at $1.2 < \lambda < 2.2 \mu\text{m}$ with NACO:

Near-infrared observations were performed on 2003 Jun 12 and 14 as well as on 2004 Apr 1 with NAOS-CONICA (NACO) at UT4. NACO consists of the high-resolution near-infrared

imager and spectrograph CONICA (Lenzen *et al.*, 1998) and the Nasmyth Adaptive Optics System (NAOS) (Rousset *et al.*, 1998). It provides adaptive-optics corrected observations in the range of $1 - 5 \mu\text{m}$ with 14 to 54 arcsec fields of view and 13 to 54 mas.

The nucleus is unresolved at all wavelengths with a size (FWHM) of 0.10 arcsec in J band, 0.088 arcsec in H band, and 0.059 arcsec in K band. The flux values given in table 5.2 are extracted in circular apertures of 0.20 arcsec, 0.18 arcsec, and 0.12 arcsec diameter in J, H and K, respectively (for details see Neumayer *et al.*, in preparation).

Millimeter observations with the SEST and the JCMT:

We determined flux densities of the Centaurus A nucleus in the millimeter wavelength range with the 15 m Swedish-ESO Submillimetre Telescope (SEST) on Cerro La Silla (Chile). The measurements presented here were obtained in February and March 2003 as close in time as possible to the epoch of the MIDI observations discussed in this chapter.

We have used these data to construct a best fit millimeter spectrum (frequency range 85 – 270 GHz) with spectral index ($S_\nu \sim \nu^\alpha$) $\alpha = -0.41 \pm 0.05$, and extracted for each receiver band the standardised flux densities at 90, 150 and 230 GHz listed in table 5.2.

In March, May and July 2003, we also obtained measurements at 265/268 GHz with the 15 m James Clerk Maxwell Telescope (JCMT) on Mauna Kea (Hawaii), the mean of which is also listed in Table 5.2. Over the full two-year period, these JCMT measurements suggest a significant drop in nuclear intensity from about 7 Jy to 4.5 Jy (for more details see Israel *et al.*, in preparation).

5.3 MIDI Results

The results of our MIDI observations are summarised in figures 5.2 to 5.4, which show the total flux $F_{\text{tot}}(\lambda)$, the correlated flux $F_{\text{cor}}(\lambda)$, and the visibility $V(\lambda)$ between 8 and $13 \mu\text{m}$ as observed on 2005 Feb 28 and May 26. Most of the observed spectral region is affected by the very broad absorption band due to silicates. The depth of the silicate feature is identical in F_{cor} and F_{tot} , indicating that both the core and extended components suffer the same extinction. The [Ne II] emission line at $\lambda = 12.90 \mu\text{m}$ is clearly detected in all four spectra displayed in figure 5.2, but not present in any of the correlated flux spectra in figure 5.3 which have superior signal-to-noise ratio. This indicates that the [Ne II] emission line arises in an extended region ($> 50 \text{ mas}$), which is over-resolved by the interferometric observations.

Centaurus A was one of the first targets to be observed with MIDI with an average N band flux $\langle F_{\text{tot}} \rangle$ below 1 Jy. For such faint sources, it is a greater challenge to measure the total flux F_{tot} accurately, rather than to determine the correlated flux, as the strong background naturally cancels out in the interferometric observations. Although figure 5.2 shows that we managed to get largely consistent results for F_{tot} in the two epochs, a closer inspection reveals discrepancies of 30% around $12 \mu\text{m}$ during one night (top panel: February 28). When comparing both nights, we find deviations $> 35\%$ in the silicate absorption feature (compare top and bottom panel) which can increase to more than a factor of 3 in the atmospheric ozone absorption band between 9.5 and $10.0 \mu\text{m}$. We attribute these discrepancies to uncertainties in the background subtraction.

An estimate of the uncertainties in determining the correlated flux F_{cor} (see figure 5.3) might be obtained by comparing the measurements over one night (*i.e.* with similar baseline, see table 5.1). Over most of the spectral range, they are confined to $\pm 10\%$. However, the significant difference between the measurements of F_{cor} on February 28 and on May 26 has

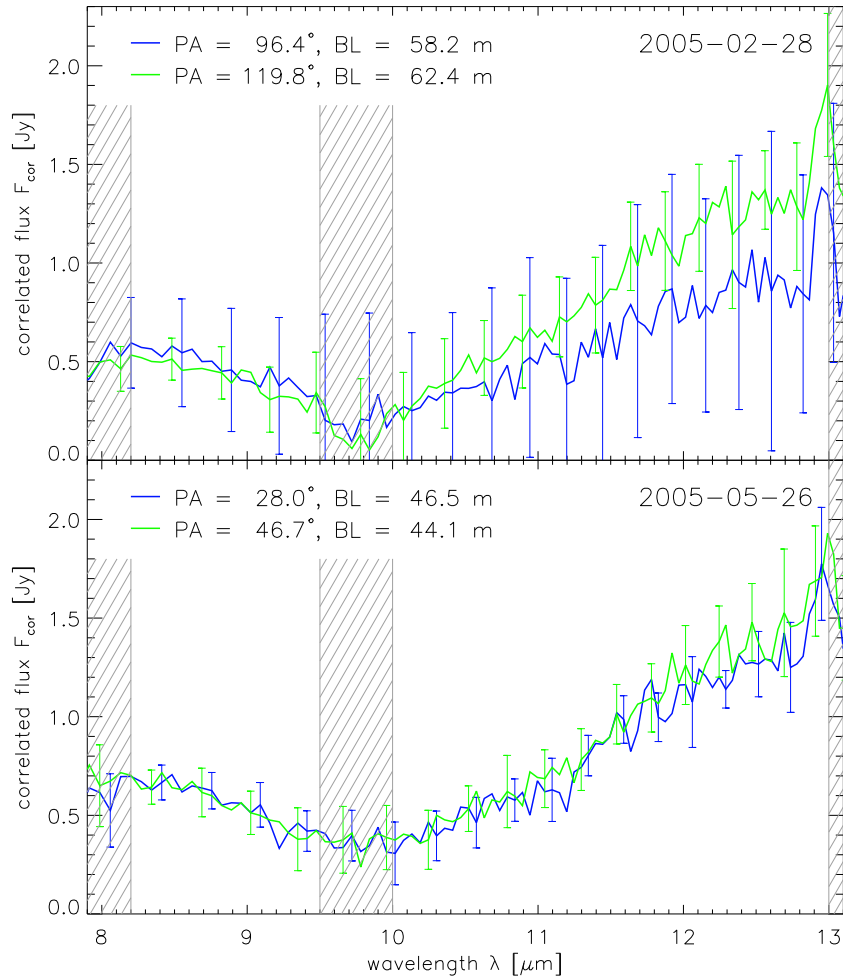


Figure 5.2: Spectrum of the total flux F_{tot} between 8 and 13 μm as observed on 2005 Feb 28 (top panel) and on 2005 May 26 (bottom panel). The obvious differences in F_{tot} are caused by imperfect background subtraction (see text). The errors are dominated by systematic uncertainties. The wavelengths $9.5 < \lambda < 10.0 \mu\text{m}$ are affected by the atmospheric ozone band (especially for observations on Feb 28, see also section 1.5). This area and the edges of the N band are hatched in grey. Note the broad silicate absorption feature at $8.5 < \lambda < 12 \mu\text{m}$ and the [Ne II] emission line at $\lambda = 12.90 \mu\text{m}$.

to be interpreted as the true interferometric signal, showing that the core of Centaurus A is marginally resolved along $PA \simeq 120^\circ$ with a 60 m baseline.

Due to the aforementioned uncertainties in F_{tot} , it is hard to judge which of the details observed in the spectral visibilities $V(\lambda)$ displayed in figure 5.4 are real: clearly, the values $V(\lambda) > 1$ obtained from the May 26 observations (lower panel) are caused by incorrect background subtraction in F_{tot} and thus indicate that the level of uncertainty in the visibility measurements can reach 30%. Accordingly, we regard the two visibility measurements of February 28 (top panel) as consistent with each other, despite the change in the baseline position angle by 23° .

Taking all discussed uncertainties into account, we conclude that there is no indication for intrinsic flux variability between the two observed epochs and that the most robust result of our measurements is the difference in the correlated flux between the two observations (that

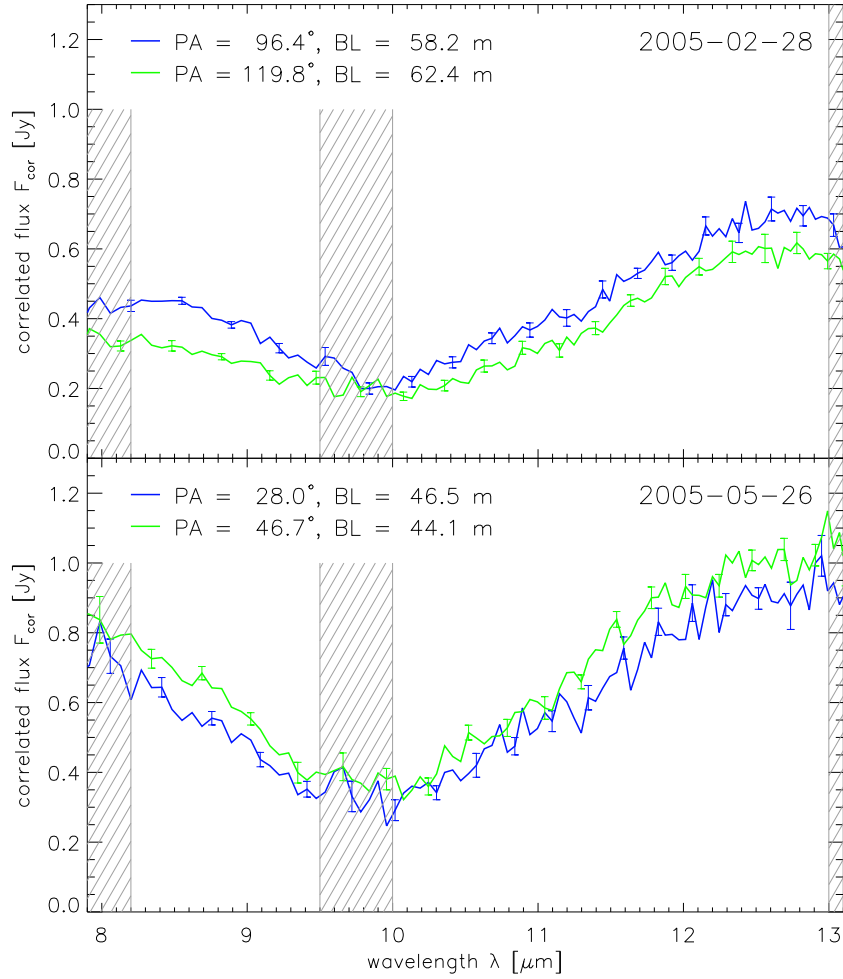


Figure 5.3: Spectrum of the correlated flux F_{cor} between 8 and 13 μm , as observed on 2005 Feb 28 (top panel) and on 2005 May 26 (bottom panel). As for F_{tot} (figure 5.2), the spectral shape is dominated by silicate absorption, but no evidence for the [Ne II] emission line is present. In contrast to figure 5.2, here the errors are dominated by photon noise.

is, the two projected baselines). The ratio

$$f_{12} \equiv \frac{F_{\text{cor}}(\text{Feb28})}{F_{\text{cor}}(\text{May26})} \quad (5.1)$$

can be approximated by a linear function $f_{12}(\lambda) = 0.8 - 0.04(\lambda - 8 \mu\text{m})$ between 8 and 13 μm (compare figure 5.5). As on May 26 we find $F_{\text{cor}} \equiv F_{\text{tot}}$ within the errors, we regard $V(\text{May26}) \simeq 1$ and $V(\text{Feb28}) = f_{12}$ as the best measurements of the visibilities. The decrease in the visibility towards longer wavelengths indicates that the source is significantly extended along $PA \simeq 120$ and that the extended emission has a spectrum which rises steeply between 9 and 13 μm , as expected for the emission from thermal dust at temperatures $T < 300 \text{ K}$ (see detailed discussion in section 5.5.2). We derive the spectrum of the compact core (figure 5.5) by averaging $F_{\text{cor}}(\text{Feb28})$ and $f_{12}F_{\text{cor}}(\text{May26})$. From the formal 2σ -limit of the visibility around $\lambda = 8 \mu\text{m}$ observed on May 26 ($V \geq 0.9$), one derives an upper limit of about 6 mas FWHM for the size of the core.

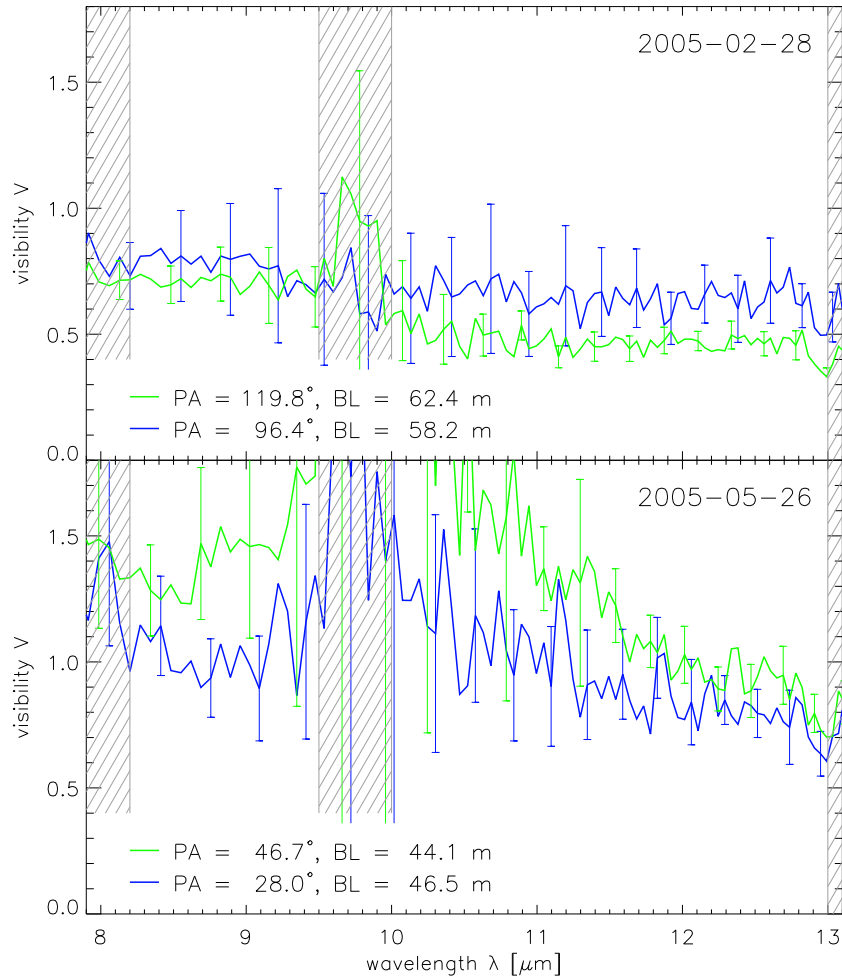


Figure 5.4: Spectrum of the visibility V between 8 and 13 μm as observed on 2005 Feb 28 (top panel) and on 2005 May 26 (bottom panel). The areas affected by atmospheric absorption are hatched in grey. Especially the wavelengths $9.5 < \lambda < 10.0 \mu\text{m}$ are strongly affected by the atmospheric ozone band. Errors are dominated by the (systematic) errors in F_{tot} .

5.4 Overall core spectrum of Centaurus A

In order to understand the nature of the – unresolved – core emission between 8 and 13 μm ($\nu = 2.3 - 3.7 \cdot 10^{13}$ Hz), it is necessary to consider not only our interferometric measurements with MIDI but also our photometry at lower and higher frequencies, as well as supplementary data from the literature. At radio frequencies ($\nu < 43$ GHz, $\lambda > 7$ mm), this is straightforward, as *very long baseline interferometry* (VLBI) measurements clearly outperform our mid-infrared interferometry in terms of resolution and extinction is not an issue. Table 5.2 lists interferometric measurements of the core flux based on the VLBI and VLBA maps by Tingay *et al.* (1998). The spectrum of the radio core is strongly inverted, $\alpha \gtrsim 2$ for $F_\nu \sim \nu^\alpha$ (compare to figure 5.7). It is unresolved at $\nu \leq 22$ GHz, but has been marginally resolved at 43 GHz with 0.5 ± 0.1 mas FWHM (Kellermann *et al.*, 1997), which corresponds to a radius of the radio core of $R_{\text{core}} = 0.0047$ pc = $1.5 \cdot 10^{14}$ m. Comparing this with the Schwarzschild radius of the $M = 6 \cdot 10^7 M_\odot$ black hole ($R_s = 1.8 \cdot 10^{11}$ m = 1.2 AU), one finds $R_{\text{core}} = 830 R_s$.

Table 5.2: Flux measurement of the core of Centaurus A.

Frequency [Hz]	Wavelength [μm]	F_ν [Jy]	$F_{\nu,0}^a$ [Jy]	Date ^b [year]	Instrument	Beamwidth [mas]	Reference
$4.8 \cdot 10^9$	63 000	1.2		1993.13	VLBI	2.6	Tingay <i>et al.</i> (1998)
$8.4 \cdot 10^9$	35 700	2.4		1996.22	VLBA	2.4	Tingay <i>et al.</i> (1998)
$22.2 \cdot 10^9$	13 500	3.5		1995.88	VLBA	1.2	Tingay <i>et al.</i> (1998)
$90.0 \cdot 10^9$	3 530	8.6 ± 0.6		2003.18	SEST	57 000	this paper
$1.50 \cdot 10^{11}$	2 000	6.9 ± 0.3		2003.18	SEST	32 000	this paper
$2.35 \cdot 10^{11}$	1 270	5.8 ± 0.2		2003.18	SEST	20 000	this paper
$2.70 \cdot 10^{11}$	1 110	5.9 ± 1.0		2003.30	JCMT	18 000	this paper
$3.75 \cdot 10^{11}$	800	8.5		1991.35	JCMT	14 000	Marconi <i>et al.</i> (2000)
$6.67 \cdot 10^{11}$	450	6.3		1991.35	JCMT	10 000	Hawarden <i>et al.</i> (1993)
$2.38 \cdot 10^{13}$	12.6	0.62 ± 0.03	1.125	2005.28	MIDI	22	this paper
$2.63 \cdot 10^{13}$	11.4	0.43 ± 0.03	1.074	2005.28	MIDI	20	this paper
$2.88 \cdot 10^{13}$	10.4	0.25 ± 0.02	0.987	2005.28	MIDI	17	this paper
$3.23 \cdot 10^{13}$	9.3	0.28 ± 0.02	1.135	2005.28	MIDI	17	this paper
$3.61 \cdot 10^{13}$	8.3	0.47 ± 0.05	0.869	2005.28	MIDI	14	this paper
$7.90 \cdot 10^{13}$	3.80	0.20 ± 0.04	0.368	2003.36	NACO	90	Prieto, priv. comm.
$1.35 \cdot 10^{14}$	2.22	$41.5 \cdot 10^{-3}$	0.190	1997.61	NICMOS	250	Marconi <i>et al.</i> (2000)
$1.39 \cdot 10^{14}$	2.15	$(33.7 \pm 2.0) \cdot 10^{-3}$	0.169	2004.25	NACO	59	this paper
$1.80 \cdot 10^{14}$	1.67	$(4.5 \pm 0.3) \cdot 10^{-3}$	0.052	2003.45	NACO	88	this paper
$1.87 \cdot 10^{14}$	1.60	$4.8 \cdot 10^{-3}$	0.065	1997.69	NICMOS	170	Marconi <i>et al.</i> (2000)
$2.34 \cdot 10^{14}$	1.28	$(1.3 \pm 0.1) \cdot 10^{-3}$	0.049	2003.45	NACO	100	this paper
$3.69 \cdot 10^{14}$	0.81	$7 \cdot 10^{-6}$	0.010	1997.80	WFPC2	100	Marconi <i>et al.</i> (2000)

^aCorrected for extinction by adopting $A_V = 14$ mag (see text).^bIn cases in which several observations were averaged, we give an average date.

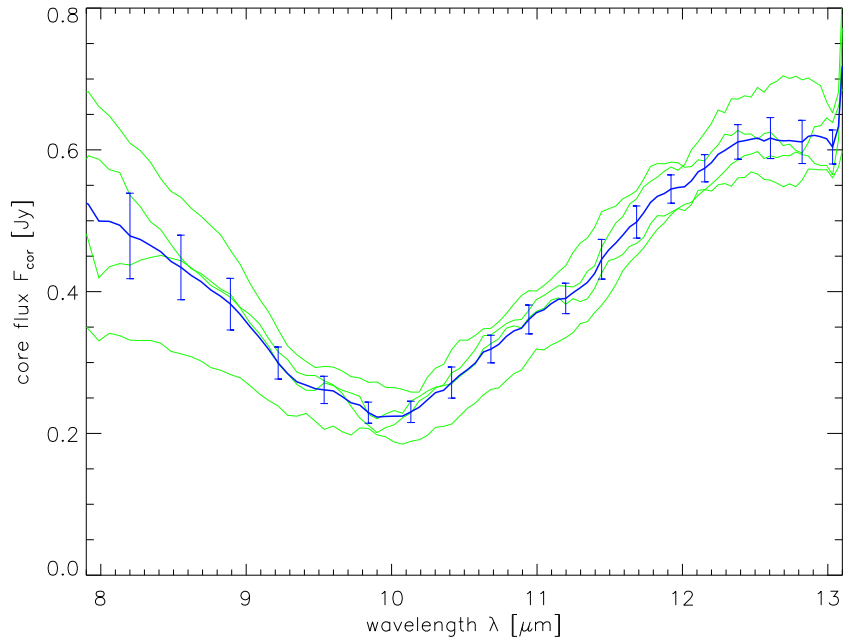


Figure 5.5: Spectrum of the four individual measurements (green) and the averaged correlated flux F_{cor} (blue) of the unresolved core (see text for details). The errors are derived from the scatter between the individual spectra.

It is much more problematic, to determine the core spectrum in the (sub-)mm regime between 90 and 670 GHz ($3 \text{ mm} > \lambda > 0.45 \text{ mm}$), due to the lack of interferometric data and the contribution of thermal emission of cold dust in the dust lane ($T \simeq 35 \text{ K}$) shortwards of $\lambda \simeq 800 \mu\text{m}$ (Hawarden *et al.*, 1993). Nevertheless, we think that our new millimeter photometry between 90 and 270 GHz – albeit obtained with single dish telescopes – should represent the core flux rather well, since the most important contaminants, the kiloparsec radio jet with its steep spectrum $F_\nu \sim \nu^{-0.75}$ (Clarke *et al.*, 1992), and the thermal dust emission, dominant at shorter wavelengths, should be negligible here.³ Indeed, we find no deviations of our flux measurements between 90 and 270 GHz from a straight, non-thermal power law $F_\nu \sim \nu^{-0.41}$. However, as illustrated by the comparison of our photometry from 2003 with that derived 12 years earlier by (Hawarden *et al.*, 1993) from mapping observations at 800 and 450 μm (see table 5.2 and figure 5.7), variability is significant at these wavelengths and can reach a factor of 1.5 or more. Thus, one has to be careful when trying to reconstruct an overall spectrum from non-simultaneous observations.

So far we have considered only radio to sub-mm frequencies, at which dust extinction can be neglected. This simplification certainly does not apply at $\lambda < 30 \mu\text{m}$ (10^{13} Hz): there is no way to obtain the intrinsic spectrum of the core of Centaurus A without correcting for the obvious extinction on our line-of-sight.

An absolute minimum for the extinction towards the core of Centaurus A is set by the value of $A_V \simeq 8 \text{ mag}$ determined from the arcsec-scale extinction map by Marconi *et al.* (2000) and Neumayer (*private comm.*). Presumably, this extinction is caused by the dust lane in Centaurus A. However, based on the presence of a circum-nuclear disk of about 80 pc

³From figure 3 in Hawarden *et al.* (1993), we estimate a maximum contamination from the dust lane of $< 0.4 \text{ Jy}$ ($< 10\%$) within our 18 arcsec beam at 270 GHz.

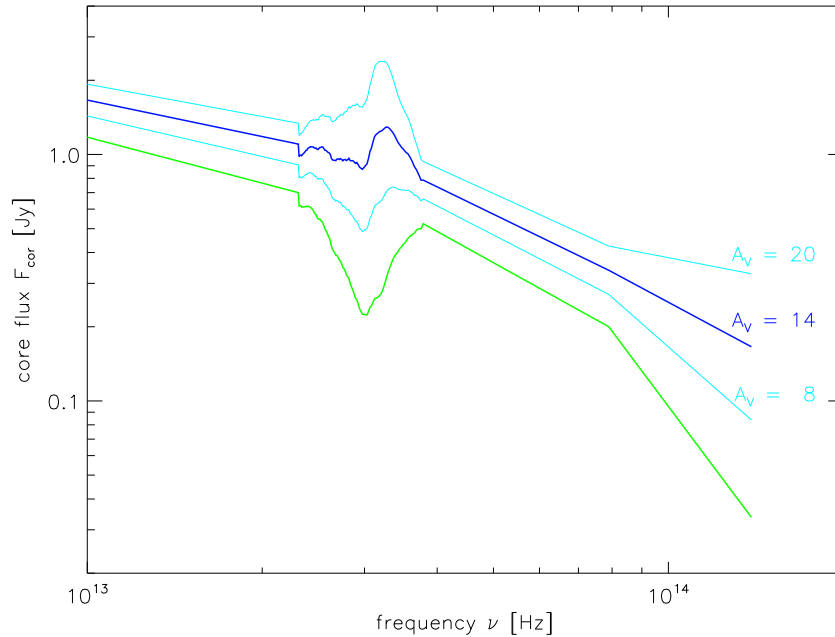


Figure 5.6: Spectrum of the core of Centaurus A between 10^{13} and $2 \cdot 10^{14}$ Hz for different values of the assumed foreground extinction. The green curve shows the observed flux F_{cor} (averaged over all measurements); the dark blue curve is corrected for a foreground extinction of $A_V = 14$ mag. The remaining residuals of $\pm 10\%$ at $9.5 \mu\text{m} > \lambda > 8.2 \mu\text{m}$ are caused by an imperfect match of the short wavelength shape of the silicate absorption. Neither leads the assumption of a minimum foreground extinction of $A_V = 8$ mag nor that of the higher extinction of $A_V = 20$ mag to a satisfactory removal of the silicate feature (cyan).

diameter, observed in molecular (Israel, 1998) and ionised gas (Schreier *et al.*, 1998; Marconi *et al.*, 2000), it is expected that the total extinction on our line-of-sight towards the core is much higher. In fact, extinction values between $A_V \simeq 14$ mag and $A_V > 40$ mag have been discussed in the literature. Here, we estimate the extinction towards the mid-infrared core by

1. assuming a galactic extinction law (Schartmann *et al.*, 2005) with a modified silicate profile using Kemper *et al.* (2004) as for Circinus (see section 4.5.1), and
2. requiring the extinction corrected spectrum in the range of $8 \mu\text{m} < \lambda < 13 \mu\text{m}$ to be as smooth as possible, *i.e.* requiring the prominent silicate feature to disappear (see figure 5.6).

This leads to our “best-guess” value of $A_V = (14 \pm 2)$ mag, where the error is estimated from the fact that $A_V = 8$ mag and $A_V = 20$ mag are clearly rejected.

We list both the observed (F_ν) and extinction corrected ($F_{\nu,0}$) values of the core flux in table 5.2, and display them in figure 5.7 as open circles and filled dots, respectively. The five values derived from our interferometric observations represent F_{cor} averaged over the measurement on February 28 and May 26, 2005. The solid line in figure 5.7 gives the best-fit standard synchrotron spectrum between $4 \cdot 10^{10}$ and $2 \cdot 10^{14}$ Hz. It is characterised by an optically thin power law $F_\nu \sim \nu^{-0.36}$, which cuts off exponentially above some cutoff frequency $\nu_c = 8 \cdot 10^{13}$ Hz and becomes optically thick below $\nu_1 = (45 \pm 5)$ GHz. We regard obvious

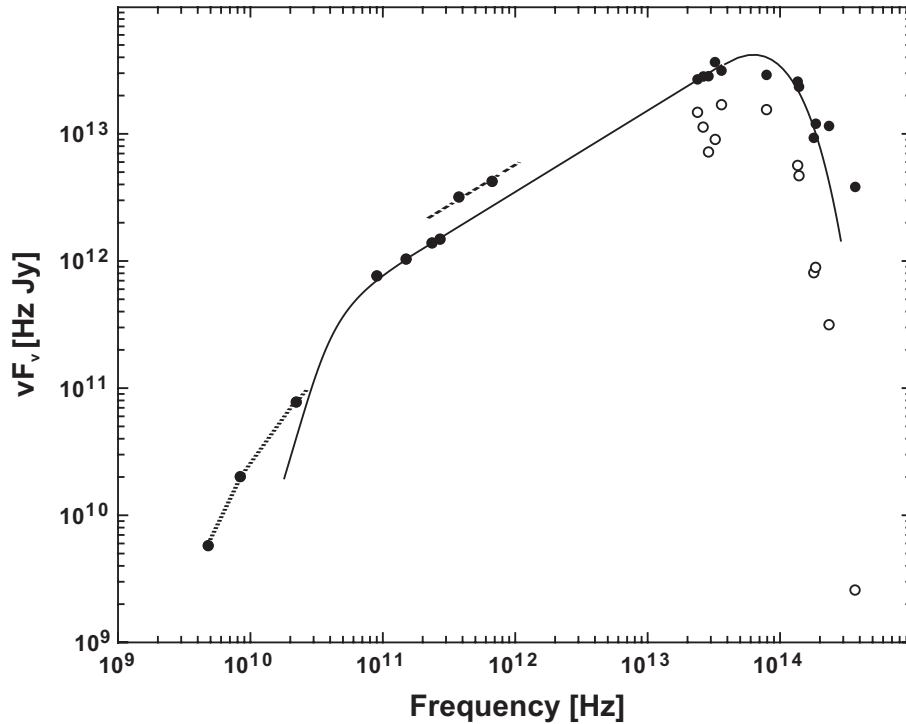


Figure 5.7: Overall spectrum of the core of Centaurus A. The open circles show the observed flux values, the filled dots are corrected for the foreground extinction of $A_V = 14$ mag (compare figure 5.6). The synchrotron spectrum (solid line) shows an optically thin power law $F_\nu \sim \nu^{-0.36}$, which cuts off exponentially at $\nu_c = 8 \cdot 10^{13}$ Hz and is self-absorbed below $\nu_1 \simeq 4.5 \cdot 10^{10}$ Hz. Evidence for variability exists around $3 \cdot 10^{11}$ Hz (dashed line through photometry in 1991) and above ν_c (various epochs between 1997 and 2005, *c.f.* table 5.2). The excess at cm wavelengths ($\nu < 2 \cdot 10^{10}$ Hz, connected by dotted lines) is due to optically thick components of larger size.

discrepancies between this synchrotron spectrum and the intrinsic, extinction corrected flux values $F_{\nu,0}$ as further evidence for variability of the core of Centaurus A.

5.5 Discussion

Our interferometric observations reveal the existence of two components in the inner parsec of Centaurus A: a resolved component, the “disk”, which is most extended along $PA \simeq 120^\circ$ and the unresolved “core”.

5.5.1 The synchrotron core

In section 5.4, it was demonstrated that the core spectrum can be fitted by a synchrotron spectrum with millimeter-to-mid-infrared power law $F_\nu \sim \nu^{-0.36}$ which cuts off exponentially towards higher frequencies. The most likely interpretation is that this source represents the “base” of the radio jet, that is, the innermost point of its relativistic outflow, at which interaction with the surrounding medium leads to the onset of efficient particle acceleration within the jet flow (for details see Meisenheimer *et al.*, 2007).

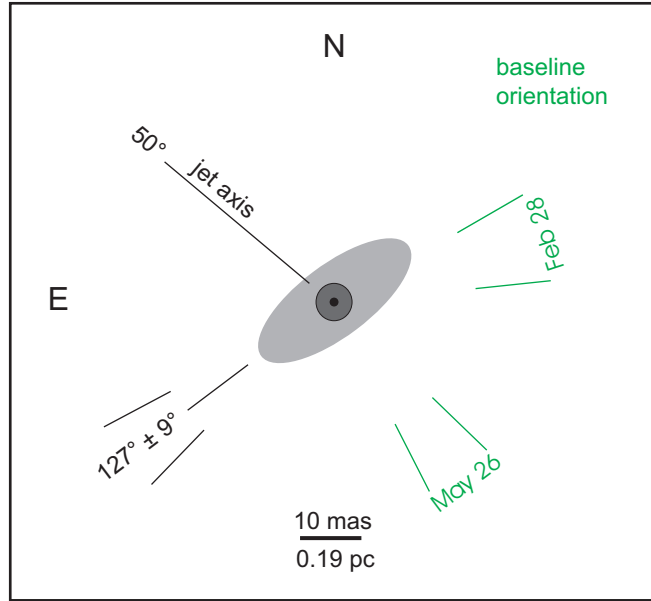


Figure 5.8: Sketch of our model for the mid-infrared emission from the inner parsec of Centaurus A. We identify the unresolved point source of < 6 mas FWHM (dark grey) with the VLBI core ($FWHM = 0.5 \pm 0.1$ mas, indicated as black dot). It is surrounded by an elongated structure of dust emission (light grey), the major axis of which is orientated along $PA = 127^\circ \pm 9^\circ$. From the visibilities observed with two baselines on February 28, we derive a major axis length of about 30 mas. Note that the major axis orientation is consistent with being perpendicular to the radio jet axis and that the axis ratio can be explained by a thin disk which is inclined by $\sim 66^\circ$.

5.5.2 Nuclear dust emission from the parsec-sized disk

As pointed out in section 5.3, our current – very limited – coverage of the uv plane leads us to the conclusion that the centre of Centaurus A is essentially unresolved along $PA \simeq 40^\circ$, but shows a clear indication for an extended component along $PA \simeq 120^\circ$. Until future interferometric observations with other baselines allow us to better constrain the size and shape of the extended component, we simply assume that the visibility $V^{\text{Feb28}}(\lambda) = 0.8 - 0.04(\lambda - 8\mu\text{m})$ along $PA = 108^\circ \pm 12^\circ$ is caused by the superposition of the unresolved synchrotron core and a well resolved, inclined disk, the major axis of which must be orientated roughly perpendicularly to $PA = 37^\circ \pm 9^\circ$, along which we find $V(\lambda) \simeq 1$. Further MIDI observations with a projected baseline > 100 m (using UT1 – UT4) will allow us to pin down the flux ratio between “core” and “disk” more accurately (see section 7.1.1). The size of the disk is poorly confined by the present observations, but needs to be $\gtrsim 30$ mas ($= 0.57$ pc) at $\lambda = 13\mu\text{m}$, in order to be consistent with our simple two-component model. As there might be a marginal decrease in the visibility along $PA \simeq 40^\circ$ towards the longest wavelengths, only an upper limit of ~ 12 mas can be given for the projected width of the disk. Figure 5.8 sketches this interpretation. Note that within the current uncertainties, the major axis of the disk could well be orientated exactly perpendicularly to the direction of the parsec scale radio jet at $PA(\text{jet}) = 50^\circ$ (Tingay *et al.*, 1998) and could represent an inclined thin disk, the axis of which is aligned with the radio axis at $50^\circ < \theta < 70^\circ$ with respect to our line-of-sight.

From the visibility V^{Feb28} and the extinction corrected flux values in table 5.2, we derive $F_{\text{disk}}(8.3\mu\text{m}) = (0.21 \pm 0.10)$ Jy and $F_{\text{disk}}(12.6\mu\text{m}) = (0.71 \pm 0.20)$ Jy, respectively. Interpreting this steep rise towards long wavelengths as the Wien tail of a blackbody spectrum from

warm dust, leads to a dust temperature of $T \simeq 240$ K. With this temperature, we derive a rough estimate of the bolometric power emitted by the dust: $P_{\text{dust}} \gtrsim 3 \cdot 10^{34}$ W. Since the dust disk seems too thin to cover more than 1π steradian (seen from the central accretion disk), we conclude that a heating power $P_{\text{heat}} \geq 10^{35}$ W is required to explain the apparent dust emission.

Regarding the size of the dust disk, it is instructive to calculate the dust sublimation (inner) radius for the required heating power $P_{\text{heat}} \gtrsim 10^{35}$ W and a sublimation temperature of 1500 K:

$$r_{in} = 1.3 \text{ pc} \left(\frac{P_{\text{heat}}}{10^{39} \text{ W}} \right)^{1/2} \gtrsim 0.013 \text{ pc}.$$

As this corresponds to < 1 mas, that is $< 1/20$ of our resolution, it is hard to determine how much the innermost parts of the dust disk could contaminate the flux from the unresolved core. In any case, we conclude that the amount of dust emission from the central parsec of Centaurus A is most likely limited by the available illuminating radiation. Thus, it is impossible to determine the gas and dust content of the innermost parsec from mid-infrared observations.

5.5.3 Comparison with other radio sources

Finally, we compare our findings on Centaurus A with other AGN which host a similarly massive black hole. It is evident that even the closest and least luminous Seyfert 2 galaxies (Circinus, NGC 1068) contain nuclear dust concentrations (“tori”) which radiate 10 to 100 times more powerfully in the mid-infrared than Centaurus A. This might be explained by the lack of an appropriate heating source. Therefore the total amount of cold dust in the inner parsecs can hardly be constrained. So certainly, Centaurus A is not a “well-hidden” Seyfert nucleus.

Instead, it shares many properties of nearby FR I radio galaxies (see section 1.1): The morphology and luminosity of its parsec to kiloparsec jets is well in the range observed for nearby FR Is. As in other FR I galaxies (Balmaverde *et al.*, 2006; Evans *et al.*, 2006), its nuclear X-ray emission is produced at least partly at the base of the radio jet. Most of the dust extinction towards the core occurs in dust structures on scales of 50 to thousands of parsec. However, the existence of a narrow-line region which exhibits high ionisation lines and our new evidence for a very compact nuclear dust disk (0.6 pc diameter) are features of Centaurus A, which are untypical for FR I radio galaxies. It is worth noting that the small dust luminosity of Centaurus A places it among the “mid-IR weak” radio galaxies, which comprise about half of a sample of FR II galaxies observed by Ogle *et al.* (2006) with the Spitzer Space Telescope.

The most unique feature of Centaurus A is its rather powerful synchrotron core, the spectrum of which peaks around 10^{14} Hz. Even the much more powerful radio galaxy M 87, which hosts a 50 times more massive black hole, cannot compete with Centaurus A in this respect. Since relativistic beaming cannot account for the difference⁴, we would like to argue that the luminous synchrotron core is an intrinsic property of Centaurus A. It is attractive to speculate that the more-than-average amount of dust and gas in the innermost parsec, as established by our detection of an extended mid-infrared emission, could play an important role in building up a strong internal shock at $d < 0.026$ pc which is capable of converting a

⁴Most authors believe that the M 87 jet is within about 20° of our line of sight. This would argue for a significantly higher Doppler factor ($\delta \gg 1$) in M 87 than inferred for Centaurus A.

significant fraction of the out-flowing kinetic energy into relativistic particles so close to the core.

5.6 Conclusions

Our interferometric observations of Centaurus A in the N band ($8 < \lambda < 13 \mu\text{m}$) provide strong evidence that its mid-infrared emission is dominated by an unresolved synchrotron core. Additionally, the observations with interferometric baselines orientated roughly perpendicularly to the parsec scale radio jet, reveal an extended component which naturally can be interpreted as a geometrically thin, dusty disk, the axis of which coincides with the radio jet. Its diameter is about 0.6 pc. It contributes between 20% (at short wavelengths, $\lambda \simeq 8 \mu\text{m}$) and 40% (at $\lambda \simeq 13 \mu\text{m}$) to the nuclear flux from Centaurus A and contains dust which is heated up to about 240 K.

We have further demonstrated that, assuming an extinction of $A_V = (14 \pm 2)$ mag, all flux measurements of the core between radio and near-infrared frequencies can be fitted nicely by a synchrotron spectrum, although there is evidence for temporal variability. The spectrum is characterised by a rather flat power law $F_\nu \sim \nu^{-0.36}$ which cuts off above $\nu_c = 8 \cdot 10^{13}$ Hz and becomes optically thick below $\nu_1 \simeq 4.5 \cdot 10^{10}$ Hz.

Chapter 6

Fainter sources observed with MIDI

6.1 Introduction

NGC 1068, Circinus and Centaurus A are the brightest AGN in the mid-infrared accessible from Paranal, that is, with $DEC < +35^\circ$. Their brightness is due to their small distance from Earth, $D \sim 16$ Mpc for NGC 1068 and $D \sim 4$ Mpc for Circinus as well as for Centaurus A. Their proximity allows them to be studied in detail at all wavelengths. Intrinsically, they are not very bright sources at all, especially Circinus and Centaurus A are comparatively dim. Interferometric observations of Circinus and Centaurus A were presented in chapters 4 and 5 of this thesis. First interferometric studies of NGC 1068 were presented in Jaffe *et al.* (2004) and Poncelet *et al.* (2006). An extensive study with similar detail to that of the Circinus galaxy is currently being performed by David Raban at the Sterrewacht Leiden in the context of his PhD thesis.

All other AGN have total fluxes in the mid-infrared of significantly less than 1 Jy. The lower luminosity is mainly a result of the larger distances to these sources, although many of them are intrinsically more energetic sources. All fainter AGN are more than $D = 25$ Mpc from Earth. Due to the larger distances, the angular scales also get smaller and the expectation is that they are less resolved. For interferometric observations, this implies that, for similar baseline lengths, the visibilities will be higher as for the three bright sources. This is a fortunate relation, as it allows us to also track the fringes of such AGN in the first place. In fact, the correlated fluxes for a few faint sources are larger than those for Circinus (see section 6.4).

The galaxy NGC 4151 is a special case. With an unresolved emission in the N band of $F_N = 1.4$ Jy (Radomski *et al.*, 2003), it is the brightest Seyfert 1 galaxy. It is the only extragalactic source ever to be observed with the Keck Interferometer (Swain *et al.*, 2003). Due to its northerly position at $DEC = +39^\circ 24'$, it does not rise more than 26° (corresponding to an airmass of 2.3) above the horizon at the location of the VLTI. Nevertheless, it would be a great success to also observe this source with MIDI. It would once and for all show that the MIDI at the VLTI is the best instrument to interferometrically study AGN. Due to the difficulty to observe it from Paranal, it is also included in the list of weaker targets discussed in this chapter.

6.2 Target list and observational challenges

A list of all AGN which have been targeted – either successfully or unsuccessfully – with MIDI is given in table 6.1. For the sake of comparison, also the three brighter sources are

included in this list. All of the fainter AGN were observed in high-sense mode using the prism as the dispersive element.

For observations of faint sources, the most challenging part is the acquisition and the photometry.

The first problem is that the adaptive optics system, *i.e.* MACAO, often fails to close the loop on the nucleus of the galaxy when no bright guide star is present. The AO system has a hard time, because the nuclei are not very bright in the optical (due to obscuration) and, worse, because they are extended sources. The chopping during the acquisition and the photometry are an additional complication for the AO system, since in every chopping cycle the loop has to be opened for the *off target position* (sky position) and then closed again for the *on target position*. The difficulties have caused MACAO to open the loop for several sources. Especially the MACAO unit on UT2 appears to have problems with faint or extended sources (*c.f.* section 3.1.2). Where MACAO fails to deliver a continuous wavefront correction, it might be advisable to use the STRAP units instead. The last resort would be to completely forego the AO correction. The flux is then spread out on the detector over a larger area. This will, however, make the detection of the source itself harder (see next paragraph) and significantly reduce the signal-to-noise ratio, if the seeing conditions are not perfect. To date, most of the faint sources have been observed with Coudé guiding on the nucleus, although for some of the sources a possible guide star is in range (see table 6.1). Especially in the case of NGC 7469, future observations should be carried out using the guide star available.

The second problem that may appear during acquisition is that the source is not visible in the mid-infrared even after very long integration times. An example for an acquisition where this is almost the case was given in the last row of figure 3.1. The residual background from the delay line tunnels can prevent the detection of such faint sources. Hopefully, the situation will be improved soon when the VCMs will be fully operational (see section 2.2.3). If the source is bright enough in the NIR, one can also try to only acquire it with IRIS. One then has to trust that the alignment of the beams in IRIS also produces a good alignment of the beams in MIDI.

The fringe detection itself does not seem to be the limiting factor for the observation of faint sources: all sources, where a stable AO correction was achieved and where the source was seen in the acquisition, could be fringe tracked.

The following individual problems were encountered when attempting to observe the fainter targets:

- **MCG-3-34-064** – For this object no source was found during the acquisition.
- **NGC 7469** – MACAO on UT2 was unable to lock on the extended nucleus.
- **LEDA 17155** – The acquisition was possible with UT3, but failed for UT2.
- **NGC 3281** – MACAO could not lock on the extended nucleus.
- **IC 4329A** – MACAO could not keep the loop closed during chopping.
- **NGC 5506** – MACAO could not lock on the extended nucleus.
- **NGC 4151** – MACAO could not keep the loop closed on UT2 while chopping. No stable fringes could be found, probably due to the high airmass.

Table 6.1: List of all AGN, for which observations with MIDI have been attempted. The columns are: (1) name and (2) type of the galaxy; (3) distance to Earth assuming $H_0 = 73 \text{ km s}^{-1} \text{ Mpc}^{-1}$; (4) date and (6) ESO programme number of the first successful observation or last unsuccessful observation attempt; (6) angular distance ψ and (7) visual magnitude V of the best Coudé guide star if present; (8) type of Coudé guiding; (9) number of successful fringe tracks obtained (without judgment of whether the data is useful or not); (10) observer or person in charge of the data analysis.

Galaxy Name (1)	Type (2)	D [Mpc] (3)	First Observation (4)	Programme number (5)	guide star ψ ["] (6)	V [mag] (7)	Coudé Guiding (8)	Number of fringes (9)	Person (10)
NGC 1068	Sy 2	16	2003 Jun 15	060.A-9224(A)		none	nucleus	9+19 ^a	Raban
Circinus	Sy 2	4	2004 Jun 03	060.A-9224(A)	50	12	star	21	Tristram
NGC 5128	FR I	4	2005 Mar 01	074.B-0213(B)	44	13	star	5	Tristram
MCG-3-34-064	Sy 2	66	2005 May 27	075.B-0697(A)		none	nucleus	none	Beckert
NGC 3783	Sy 1	45	2005 May 27	075.B-0697(A)		none	nucleus	5	Beckert
MCG-05-23-016	Sy 1.9	35	2005 Dec 19	076.B-0038(A)	22	15	star	1	Tristram
Mrk 1239	Sy 1	82	2005 Dec 19	076.B-0038(A)		none	nucleus	2	Tristram
NGC 1365	Sy 1.8	52	2006 Sep 11	077.B-0026(B)	65	15	nucleus	2	Jaffe
NGC 7469	Sy 1	75	2006 Sep 11	077.B-0026(B)	13	15	nucleus	1	Jaffe
LEDA 17155	Sy 2	196	2006 Sep 11	077.B-0026(B)		none	nucleus	none	Jaffe
NGC 3281	Sy 2	49	2007 Feb 07	078.B-0031(A)	53	17	nucleus	none	Raban
IC 4329A	Sy 1	74	2007 Feb 07	078.B-0031(A)	59	17	nucleus	1	Raban
3C 273	Quasar	650	2007 Feb 07	078.B-0031(A)	53	14	nucleus	2	Raban
NGC 5506	Sy 2	29	2007 Feb 07	078.B-0031(A)		none	nucleus	none	Raban
NGC 4151	Sy 1	14	2007 Feb 07	078.B-0031(A)		none	nucleus	none	Raban

^a9 fringe tracks in science demonstration time (SDT) using the prism and 19 fringe tracks in open time using the grism.

6.3 Observations and data reduction

In the following, three sources will be considered in greater detail: MCG-05-23-016, Mrk 1239 and 3C 273. Details of the observations for these three sources as well as for the associated calibrators are given in table 6.2.

In order to reach an acceptable signal-to-noise ratio, longer integration times are needed: The *NDIT* for the fringe tracks and the photometry were increased to 12000 and 8000 frames, respectively. Since the photometry is the limiting factor for the determination of the visibility, the photometry was obtained twice for several sources. This and the often longer acquisition procedure lead to a considerably longer time for the measurement of one visibility point (*c.f.* section 3.1.5). The measurement can take up to 1 hour for the science target only, that is, the full, calibrated visibility point takes 1.5 hours.

The data reduction for these sources was only possible with EWS. A reduction attempt with MIA failed. As for Circinus, the settings for the data reduction were `smooth = 10`, `gsmooth = 10`, `dave = 1` and `nophot = 1`.

6.3.1 Mrk 1239 and MCG-05-23-016

For the second observation of Mrk 1239 (sci53), the MACAO loop was open for a portion of the second photometry of beam B (UT2). To fix this, the faulty photometry was replaced by the one taken during the first observation (sci52, see table 6.2). The second observation of the calibrator HD 083618 was obtained at the end of the night and no photometric data could be recorded. The data set was completed using the photometry from the first observation of this calibrator (cal52). To obtain the final fluxes and the visibility, the two individual measurements of Mrk 1239 were averaged. This was possible because the position angle and baseline length only differ insignificantly. Because the errors on the photometry of MCG-05-23-016 and the second measurement of Mrk 1239 were implausibly large, they were truncated corresponding to a relative error of 90%.

6.3.2 3C 273

For 3C 273, MACAO could not keep the loop closed during chopping and, by consequence, no acquisition images and photometry could be obtained. Given the pointlike nucleus with $V = 12.8$ mag (Türler *et al.*, 2006), the reason for this malfunction remains unexplained. Instead, the beams were aligned with IRIS in the K band (9.7 mag). The two useable fringe tracks were recorded consecutively. For the data reduction, they were merged and reduced as a single, long track. Because no photometric data was available, only the calibrated correlated flux could be determined. Intermediate band photometry with VISIR was obtained in an observation run on 2007 Mar 01, that is, 23 days after the interferometric observations (see also section 7.1.3). VISIR, the *VLT Imager and Spectrometer for the mid-InfraRed*, provides a long-slit spectrometer as well as a high sensitivity imager in both the N and the Q bands (Lagage *et al.*, 2004). The two filters observed are PAH1 ($\lambda_0 = 8.59 \mu\text{m}$, $\Delta\lambda = 0.42 \mu\text{m}$) and SiC ($\lambda_0 = 11.85 \mu\text{m}$, $\Delta\lambda = 2.34 \mu\text{m}$; Smette and Vanzi, 2007). The calibrator star for the VISIR observations was HD 124294. The data reduction for the VISIR data is similar to that for the acquisition images of MIDI. The photometry was extracted in a 2.25 arcsec aperture. For the calibration, the template spectrum from the catalogue by Roy van Boekel (*private comm.*) was used. The errors were estimated by increasing the aperture to 3.00 arcsec and by decreasing it to 1.50 arcsec – for both the calibrator and the source in the opposite way.

Table 6.2: Log of the observations of MCG-05-23-016, Mrk 1239 and 3C 273. The columns are the same as in table 4.1.

Date and time [UTC]	Object	DIT [mas]	NDIT fringes	Airmass	Seeing ^a ["]	BL [m]	PA [°]	Associated calibrator and comments		
2005 Dec 19:	UT2 – UT3	075.B-0697(A)								
05:07:40	HD 090610	cal51	0.018	8000	2500	1.715	0.91	45.09	28.2	
06:39:51	MCG-05-23-016	sci51	0.018	12000	2 × 8000	1.115	0.75	46.13	36.4	cal51
07:31:59	Mrk 1239	sci52	0.018	12000	2 × 8000	1.135	0.70	41.09	40.6	cal52
08:15:17	HD 083618	cal52	0.018	8000	2500	1.091	0.51	43.89	44.8	
08:47:23	Mrk 1239	sci53	0.018	12000	2 × 8000	1.087	0.55	44.81	44.8	cal53
09:29:39	HD 083618	cal53	0.018	8000		1.129	1.00	46.28	43.3	phot B unusable, replaced phot B of sci52 replaced missing phot by that of cal52
2007 Feb 07:	UT2 – UT3	078.B-0031(A)								
06:04:10	3C 273	sci61	0.018	8000		1.286	0.74	36.69	31.0	cal61
06:08:32	3C 273	sci62	0.018	8000		1.272	0.71	36.98	31.6	cal61
06:31:50	HD 098430	cal61	0.018	8000	4000	1.018	0.60	45.85	38.6	

^aFrom the seeing monitor (DIMM).

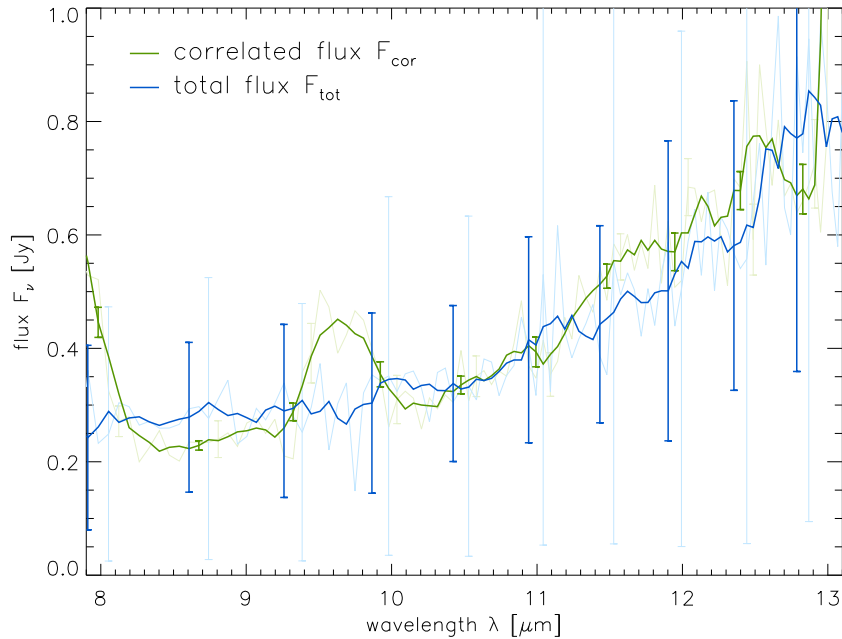


Figure 6.1: Spectrum of the total flux and the correlated flux of MCG-05-23-016. The data (in light green and light blue) were smoothed in wavelength direction with a boxcar width of $\Delta\lambda \approx 0.4 \mu\text{m}$ to obtain smoother curves and smaller errorbars (dark green and blue).

6.4 Results

6.4.1 MCG-05-23-016 and Mrk 1239

Essentially, only one uv point for each MCG-05-23-016 (ESO 434-G040) and Mrk 1239 were obtained in order to check the feasibility of observations. The spectra of the total and correlated fluxes are shown in figures 6.1 for MCG-05-23-016 and in figure 6.2 for Mrk 1239. The visibilities for both sources are reproduced in figures 6.3 and 6.4. For sources as weak as these, the errors determined with EWS have to be considered with particular caution. Especially the photometry can have very large – or, to be more precise, unrealistically large – errors. The large errors propagate into the visibility, but not into the correlated flux due to its direct calibration (see section 3.4). The latter seems to have rather too small errors.

The shapes of the spectra of the two sources are characteristic for the type of the nucleus. MCG-05-23-016 is a lenticular Seyfert 1.9 galaxy at a distance of approximately 35 Mpc, which has been studied mostly for its X-ray emission (*e.g.* Balestra *et al.*, 2004; Mattson and Weaver, 2004). The spectrum rises strongly towards longer wavelengths. It has a very shallow silicate absorption feature (see also Frogel *et al.*, 1982). Mrk 1239 is a Seyfert 1 galaxy located at a distance of about 82 Mpc. Its unresolved near-infrared emission shows a strong bump at $2.2 \mu\text{m}$, which is interpreted in terms of very hot dust ($T = 1200 \text{ K}$), near its sublimation temperature, very likely located both in the upper layers of the torus and close to the apex of the polar scattering region (Rodríguez-Ardila and Mazzalay, 2006). It has a flat spectrum in the MIR or, with some imagination, perhaps even some silicate emission.

The flux values measured are on the order of 0.4 Jy for MCG-05-23-016 and 0.5 Jy for Mrk 1239 for both the correlated and the total fluxes. That is, the correlated fluxes of both sources are consistent with unresolved objects ($F_{\text{cor}} \approx F_{\text{tot}}$). Observations with longer

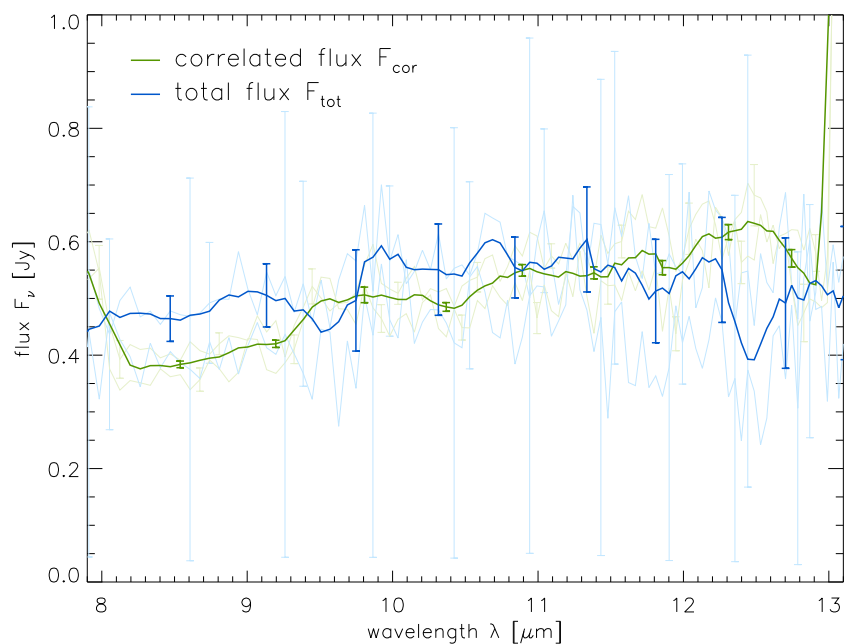


Figure 6.2: Spectrum of the total flux and the correlated flux of Mrk 1239. The two measurements (in light green and light blue) were combined by a weighted mean and then smoothed in wavelength direction with a boxcar width of $\Delta\lambda \approx 0.4 \mu\text{m}$ to obtain smoother curves (dark green and blue).

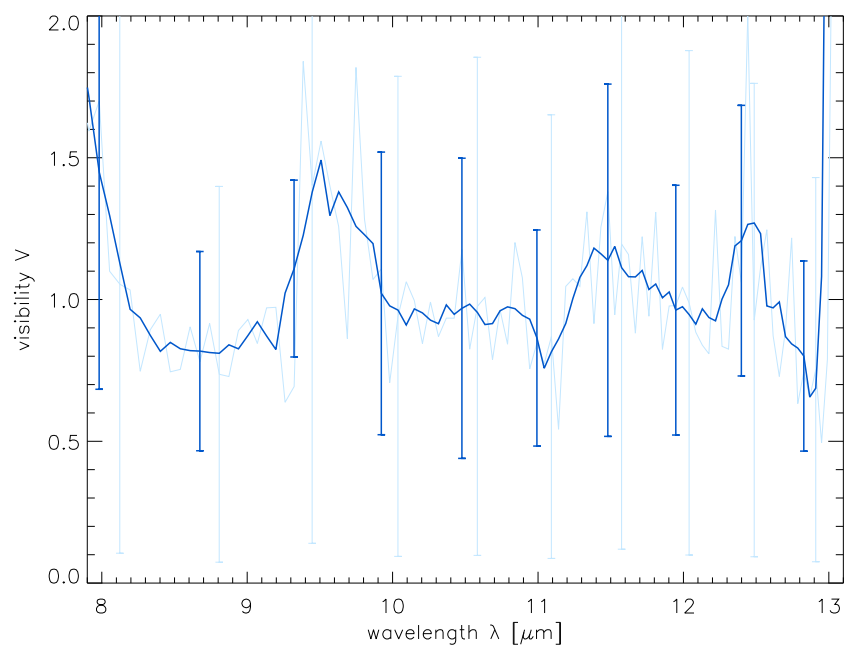


Figure 6.3: Spectrum of the visibility of MCG-05-23-016. The directly measured data of MCG-05-23-016 is drawn in light blue. The same smoothing as in figure 6.1 was applied to the visibilities to obtain the dark blue curve.

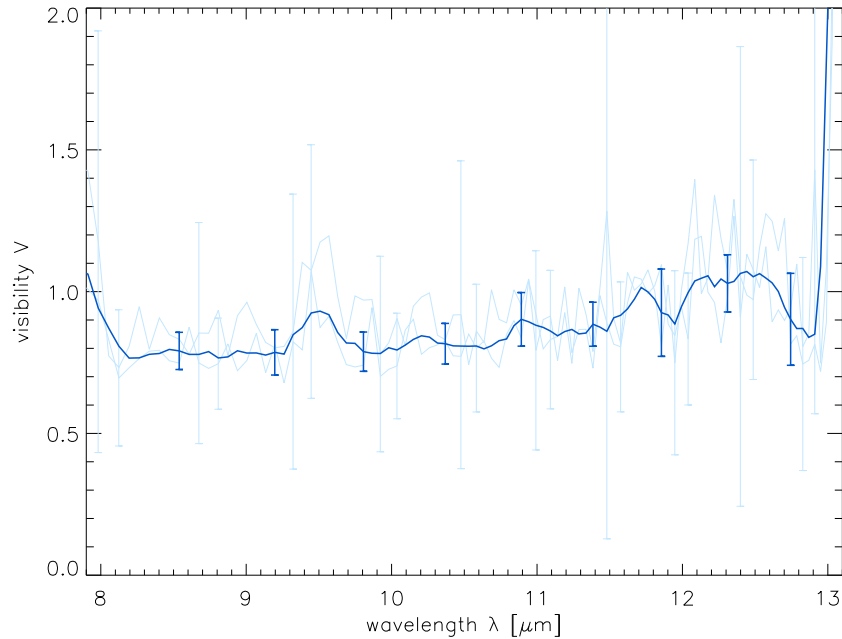


Figure 6.4: Spectrum of the visibility of Mrk 1239. The two individual data sets for Mrk 1239 are drawn in light blue. The same combination and smoothing as in figure 6.2 was applied to the visibilities to obtain the dark blue curve.

baselines are thus needed. Note that the correlated fluxes are larger than those for Circinus (compare figure 6.2 to yellow curve in upper panel of figure 4.4)

Assuming a Gaussian flux distribution, we can derive an upper limit for the sizes of the emission regions. Using equations (2.44) and (2.45), it is possible to directly set the full width at half maximum $FWHM(\lambda)$ of the Gaussian brightness distribution in relation to the visibility $V_B(\lambda)$:

$$FWHM(\lambda) = \frac{\lambda}{B} \cdot \frac{2}{\pi} \sqrt{-\ln 2 \cdot \ln V_B(\lambda)} \quad (6.1)$$

The full widths are shown in figure 6.5 for both sources. By definition, $FWHM = 0$ when $V(\lambda) \geq 1$ (see section 2.1.4). The errors for the $FWHM$ were calculated for 2σ deviations of the visibility¹. Accepting the errors at their face values, we can read off an upper limit of the size by eye. We conclude that the emission region in MCG-05-23-016 has a size of less than 20 mas, which corresponds to less than 4 pc at the distance of the galaxy. The MIR source in Mrk 1239 is most likely similarly small with a size of less than 15 mas, that is, less than 6 pc. When interpreting the latter limit, one has to take into account that in the Seyfert 1 case, the infrared flux is dominated by the flux from the accretion disk, which appears as a point source. This implies that the limit derived from our data is not a measure for the size of the dust torus alone, but for the combination of the torus and the accretion disk flux. To disentangle the two contributions, further measurements (with the same position angle but longer baseline lengths) must be obtained.

¹Because of the nonlinear dependency of the $FWHM$ on the visibility in equation (6.1), the upper and lower limits were calculated directly from the upper and lower limits of the visibility.

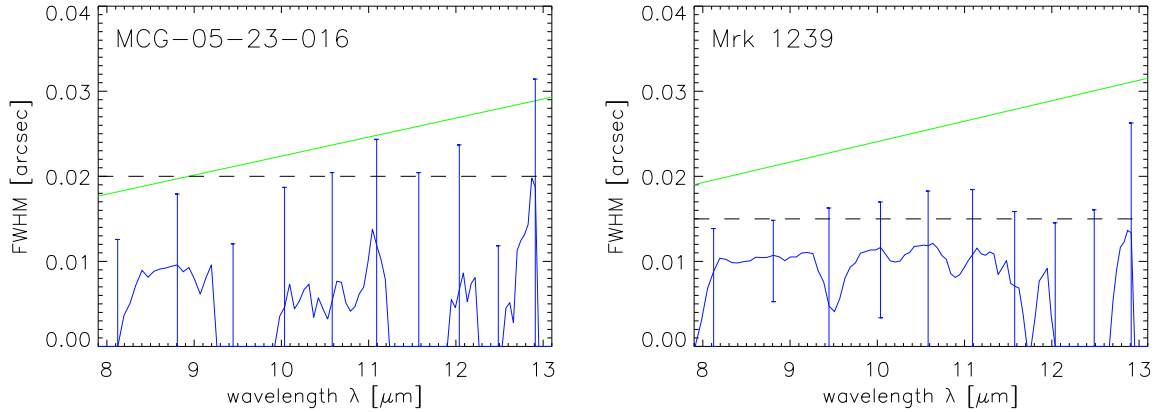


Figure 6.5: Size estimates for the nuclear MIR emission in MCG-05-23-016 (left) and Mrk 1239 (right). The $FWHM$ of a Gaussian distribution corresponding to the visibilities shown in figures 6.3 and 6.4 is given in blue. The errorbars correspond to 2σ deviations of the visibility. From this, an upper limit on the size of the brightness distribution can be derived (dashed horizontal lines). The resolution of the interferometric set-up according to $\zeta = \lambda/2B_{\text{proj}}$ (see equation 2.13) is also shown in green.

6.4.2 3C 273

3C 273 (PG 1226+023) was the first quasar to be discovered (see section 1.1). Because it is the brightest object of its kind and because it exhibits a one-sided jet which is visible from the radio regime to X-rays, it is one of the best observed and studied AGN. The quasar is located at a redshift of $z = 0.158$, which corresponds to a distance of 650 Mpc ($H_0 = 73 \text{ km s}^{-1} \text{ Mpc}^{-1}$). A detailed review of the source is given by Courvoisier (1998).

The results of our measurements, that is, the correlated flux from MIDI and the VISIR photometry, are shown in figure 6.6. The MIDI spectrum is slightly concave and a power law fit yields $F_{\text{cor}} \propto \lambda^{2.0 \pm 0.1}$. To our surprise, the VISIR data points are below the correlated flux. The VISIR data points are consistent with earlier MIR photometry, *e.g.* TIMMI2 observations from 2004 Jun 19 (Türler *et al.*, 2006) or Spectroscopy with the Spitzer Space Telescope (Hao *et al.*, 2005). The Spitzer spectroscopy has shown the silicate feature in slight emission, indicating the presence of significant amounts of hot dust. Due to this silicate emission, the Spitzer spectrum is slightly convex, in contrast to the spectrum observed with MIDI, which is rather concave. The only explanation we can think of is that 3C 273 had an outburst during the MIDI observations. Variability of up to $\sim 60\%$ has been observed in the mid-infrared at $10.6 \mu\text{m}$ (Neugebauer and Matthews, 1999). The hypothesis of an outburst could also explain the change in the shape of the spectrum: during the outburst, the spectrum would have been dominated by a power law synchrotron emission (similar to Centaurus A), while in the normal state a significant amount of the flux originates in warm dust.

Despite the possibility that an outburst could explain the discrepancy between the MIDI data and the other observations, we remain suspicious of the MIDI data. New observations with MIDI should be performed and it is imperative to ensure that a photometry is obtained as closely as possible in time to the fringe tracks.

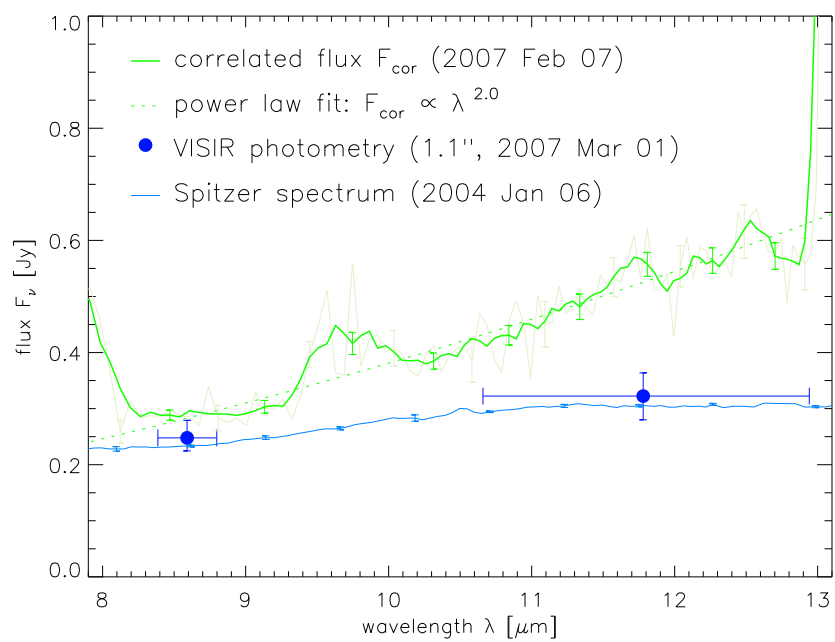


Figure 6.6: Spectrum of the correlated flux measured with MIDI on 2007 Feb 07 (green) and intermediate band photometry measured with VISIR (blue). The “bump” in the MIDI spectrum between 9.5 and 10.0 μm due to low signal-to-noise ratio in the ozone absorption band. For the VISIR data, the error bars in wavelength direction correspond to the width of the filter at half of the maximum transmission. Also plotted is the Spitzer spectrum from (Hao *et al.*, 2005).

Chapter 7

Outlook and conclusions

7.1 Outlook

7.1.1 Further interferometric investigations

The investigation of AGN using interferometric methods is only at its beginning. The first results have shown that we have a powerful tool to probe the geometrical and physical properties of the nuclear matter in AGN on scales of less than one parsec. However, only a limited number of questions have been answered so far. And they have only been answered for three objects. In fact, the difficulty in interpreting the data and the disparate results for each of the three objects investigated raise a number of new questions: What is the detailed structure of the torus? Is it possible to quantify the degree of clumpiness? Can we determine whether the disk component is warped? What are the properties of the dust? Is there any dust processing? Are we only looking at a few particular objects? Can we make more general statements which are valid for all AGN? In order to address these questions, interferometric observations and the analysis of the interferometric data have to continue:

1. **Further analysis of the data:**

The immediate task is to continue the analysis of the data which is already available. The data for several targets listed in table 6.1 have not yet been analysed. The results of this analysis will provide the ground to plan further, more detailed studies of the most interesting objects. For NGC 1068, Circinus and Centaurus A, the analysis should likewise continue and also include the information in the differential phases. The phase information allows the measurement of the relative offset of the peak of the emission at different wavelengths. It can be used to determine an asymmetry of the source and it can be used to derive the inclination of the dust structure. It will also constrain radiative transfer models, as these show asymmetries in their brightness distributions, when the objects are not seen exactly edge- or face-on. Moreover, it has to be explored to what degree an irregular behaviour of the visibility amplitude in conjunction with phase drifts or jumps can be seen as evidence for an inhomogeneous dust distribution. In the case of positive results, this would provide further evidence for the clumpiness of the torus.

2. **Further observations of the bright sources:**

For the three well-studied objects (NGC 1068, Circinus and Centaurus A), the coverage of the uv plane should be improved in order to better constrain the current models. As has been pointed out in section 4.3.1, there are still significant holes in the uv coverage for the Circinus galaxy. The same is true for NGC 1068.



Figure 7.1: Clouds over the dome of the residencia (the accommodation facilities) at Paranal Observatory on 2005 Apr 15. The planned AT observations of Circinus failed due to these clouds. For future interferometric observations of AGN we hope for no clouds! Image courtesy of David Raban.

For these two highly resolved sources, observations at shorter baselines are needed to better constrain the properties of the extended dust emission. Such observations are not possible with the unit telescopes. Shorter baselines down to 16 m^1 are only possible with the auxiliary telescopes. Because of the smaller light collecting area of these telescopes and the low correlated fluxes of the sources, such observations will be challenging. A first attempt to observe Circinus with the auxiliary telescopes was scheduled on 2007 Apr 15. This run failed due to bad weather conditions on Paranal (see figure 7.1). A second attempt, this time for NGC 1068 is planned for October 2007.

At the same time, NGC 1068 and Circinus should also be observed using longer baselines in order to check for an unresolved point source. Vanishing visibilities for longer baselines will also rule out uniform disks and other models with sharp edges, as these produce an oscillating and hence measurable visibility also for longer baselines.

In Centaurus A, new measurements at different position angles and with longer baselines will better constrain the orientation and proportion of the dust disk as well as of the portion of flux coming from the unresolved synchrotron core (*c.f.* section 5.5.2). An observing run including measurements of Circinus and Centaurus A with the UT2 – UT4 baseline was scheduled to take place on 2007 May 04. It also fell victim to bad weather conditions on Paranal.

3. Image reconstruction:

The final goal will be to reconstruct images from the interferometric data. A densely covered and uniform uv plane (see previous “action item”) is a prerequisite to attempt such a reconstruction. For the reconstruction itself, two methods offer themselves: a maximum entropy method and a clean algorithm. The latter has already been tried on Circinus but without much success (see section 4.4.1).

¹Theoretically, the shortest baseline possible is 8 m, but this is currently not offered by ESO.

4. Further observations of the faint sources:

For the fainter sources which have already been observed, measurements with a second, longer baseline should be obtained, as the sources only become interesting when they start to be marginally resolved. Together with a second observation using a perpendicular baseline orientation, the data could be used to determine the size of the emission region and to estimate the orientation of the source. This information could then be compared to other orientation indicators, such as outflows or ionisation cones. Because no Seyfert 1 galaxy has been studied in detail so far, one very important aspect has not yet been addressed: it remains to be seen whether there are any intrinsic differences in the dust distribution between Seyfert 1 and Seyfert 2 nuclei. The question is whether they both possess the same type of tori, or whether type 1 objects are less dusty.

5. Enlargement of the source sample:

A larger sample of objects has to be studied in order to draw more general conclusions on the distribution of dust in AGN. Many sources are in reach of MIDI which still has not reached its final sensitivity limit. Five additional sources which were already dropped from the GTO list and a number of further mid-infrared bright galaxies are within the sensitivity range of MIDI.

6. Comparison to simulations:

Many of the above questions can only be answered by full physical modelling, using hydrodynamic and radiative transfer simulations. To fully understand the assembly of AGN and the processes involved in their functioning, such modelling has to be used in conjunction with the observations. Such models are especially important for the interpretation of the interferometric data, as long as high quality image reconstruction is not possible. Inversely, the interferometric data, together with information on the SED, are powerful constraints on the models. The comparison of the new interferometric data to the models has only just begun (see section 4.5; Hönig *et al.*, 2006; Schartmann, 2007) and must be continued vigorously.

7. Other interferometric instruments:

Finally, MIDI should not remain the only instrument capable of studying AGN interferometrically. Studies in the near-infrared would perfectly complement the MIDI data. Unfortunately, all current attempts to observe NGC 1068 with AMBER have failed. It would be a great breakthrough, if the sensitivity of AMBER in conjunction with the VLTI could be so improved, that these observations succeed (see also Petrov *et al.*, 2007). Due to the shorter wavelengths, the near-infrared data will have a significantly higher resolution and at the same time probe the hot dust at the inner rim of the torus. Entirely new possibilities (especially for imaging) will open up by MATISSE, the planned successor of MIDI. MATISSE, the *Multi AperTure mid-Infrared SpectroScopic Experiment*, is planned as a mid-infrared spectro-interferometer combining the beams of up to four telescopes of the VLTI in the L, M and N bands (Lagarde *et al.*, 2006; Lopez *et al.*, 2006). With these characteristics, MATISSE will be efficient instrument for image reconstruction.

Of further interest is the development of a large new optical/infrared interferometer at the Magdalena Ridge Observatory (MRO) in New Mexico, USA. This optical aperture synthesis array, consisting of ten 1.4 m telescopes with baseline lengths of up to 400 m, is also intended to allow the study AGN by interferometric means (Buscher *et al.*, 2006).

All in all, the study of AGN using optical/infrared interferometry has a very promising future!

7.1.2 The nuclear SED of AGN

Our interferometric observations have shown that the nuclear dust distribution, which is directly heated by the accretion disk, is very small and hence remains unresolved by current single dish telescopes. Most of the mid- and far-infrared spectra have been obtained with infrared space observatories such as IRAS, ISO and Spitzer. Due to the low spatial resolution of these instruments compared to earth-bound instruments, their mid- and far-infrared spectra of AGN are significantly contaminated by emission from large distances from the proper nucleus, that is, from their host galaxies. The effect becomes increasingly important for longer wavelengths, because the resolution drops and cooler dust ($T \lesssim 100$ K) is probed. Such cool dust is also found in circum-nuclear starbursts. For this reason, high resolution photometry or spectra at longer wavelengths have to be obtained and then to be used to distinguish the true nuclear flux from the contaminating contribution. These fluxes will provide new constraints on radiative transfer models of dusty tori, as the models are still mainly tailored to correctly reproduce the spectral energy distributions.

In this context, near-infrared photometry of several nearby AGN was obtained with NACO. NACO provides adaptive optics assisted imaging, imaging polarimetry, coronagraphy and spectroscopy in the near-infrared, that is, from 1 to 5 μm . The NACO system is composed of two parts, the NAOS (*Nasmyth Adaptive Optics System*) adaptive optics system and the CONICA (*COudé Near Infrared CAmera*) near-infrared camera and spectrometer (Lenzen *et al.*, 2003; Lagrange *et al.*, 2003).

Together with our interferometric data in the mid-infrared, genuine spectral energy distributions (SEDs) of the central few parsec of the nearest and brightest active galaxies were compiled. A preliminary analysis has shown that the SED shape largely departs from that derived from large aperture data (Prieto *et al.*, 2007). At $\lambda < 2 \mu\text{m}$, the flux drops strongly and, in the mid- and far-infrared, the fluxes are significantly lower than in the large aperture data from satellite observations. Accordingly, the true bolometric luminosity of the AGN cores turn out to be approximately an order of magnitude lower than previously estimated on the basis of IRAS/ISO data. These findings indicate that large aperture infrared data are significantly dominated by the contribution of the host galaxy. The new derived infrared bolometric luminosities still exceed the output energy measured in the high energies by factors of 3 to 60. As it is expected that both luminosities should be comparable within an order of magnitude, the reduced factors between both suggest that the new infrared luminosities are getting closer to the genuine power output of the core.

To also establish the SED at longer wavelengths, Q band photometry at 20 μm for a similar sample of nearby AGN has been obtained with VISIR. These data awaits further analysis.

7.1.3 VISIR spectroscopy

A programme was initiated to observe the Circinus nucleus using high resolution spectroscopy of emission lines in the mid-infrared. The programme has the goal to map the nuclear gas dynamics, in order to set the detection of the dusty torus described in chapter 4 in relation to the surrounding gas. It is meant to shed light on how the inner dust structure seen by MIDI is linked to the extended ionised gas in the ionisation cone and to the gas located at the outer edge of the torus. Similar programmes have also been initiated for NGC 1068 and Centaurus A.

Although no emission lines were detected in the low resolution ($R \sim 30$) spectrum of Circinus with MIDI, both the [Ne II] 12.8 μm line and the [S IV] 10.5 μm line are clearly

visible in the spectra ($R \sim 100$) by Roche *et al.* (2006) down to radii of 0.3 arcsec from the very centre of the galaxy (see figure 4.3). At smaller distances, the spectrum is dominated by the nuclear emission. As the spectral resolution by Roche *et al.* is insufficient to derive any information on the dynamics of the gas, high resolution spectra ($R \sim 3200$) were obtained with VISIR, the VLT spectrometer and imager for the mid-infrared (see Lagage *et al.*, 2004). VISIR essentially is diffraction limited in the N band, as the resolution of a single 8-meter telescope at $12 \mu\text{m}$ is about 300 mas. These observations were obtained on 2007 Mar 01 – the same night the photometry of 3C 273 was obtained.

Five spectra of the [Ne II] line with the slit in direction of the torus were recorded. The five slit positions were displaced by 400 mas perpendicular to the slit direction resulting in a 4×2 arcsec map. Similarly, three [S IV] spectra with the slit perpendicular to the dusty torus were recorded. From the maps, it will be possible to distinguish between rotation, outflow or turbulent motion stirred up by star formation processes. An outflow will show a clear blue- or redshift, while turbulence will result in a simple broadening of the line.

Although this data has not yet been reduced, a rotational pattern perpendicular to the torus axis can be clearly seen in the raw data. Along the direction of the ionisation cones, indeed, two velocity components, one receding and one approaching, appear to be present. The data hence looks very promising.

7.2 Conclusions

For the description of active galactic nuclei, an elegant approach consists in the unification of the various manifestations of these objects in a single axisymmetric model with only a few free parameters. It reflects our desire to simplify our view of nature as much as possible. Many of the details of such unified models remain unclear, reflecting that many processes, such as the accretion mechanism and the formation of jets and outflows, are not yet well understood. Obscuring dust and gas are fundamental components in the concept of unified schemes. The distribution and the properties of this material have a significant impact on the appearance of AGN. The dust furthermore plays an important role in the energy budget of AGN, as it converts the high energy radiation from the accretion disk into thermal emission in the mid-infrared.

The aim of this thesis has been to reveal the nature of the nuclear mid-infrared source in a selected number of nearby AGN and by this means to probe their nuclear dust distribution. The small angular scales of the emission at these wavelengths necessitate interferometric observations: with the present technology interferometry remains the only method to resolve the MIR emission. More precisely, the only instrument currently capable of performing such measurements is MIDI at the VLTI.

The emphasis in the present thesis has been put on the Circinus galaxy, a prototype Seyfert 2 galaxy and the second brightest AGN in the mid-infrared. Our extensive interferometric measurements have allowed us to study the nuclear MIR source of this galaxy in detail. The direct analysis of the data has already led us to a first understanding of the properties of the source. The low correlated fluxes (low visibilities) indicated a highly resolved source. The variations of the correlated fluxes with position angle provided first indications for an elongation of the emission region. The further analysis of the data was not straightforward, considering the complexity of the source morphology and of the interferometric data. This was the first time that such a detailed analysis of an AGN using data from optical/infrared interferometry has been performed. A three step approach was pursued to analyse the data in greater detail. This analysis revealed two components in the nucleus of Circinus. Using the

latest results from hydrodynamical models of AGN tori, these components are interpreted as a disk-torus configuration: a disk-like component with a radius of 0.2 pc is located inside a larger geometrically thick component extending out to 1 pc. The disk is oriented perpendicular to the ionisation cone and it coincides with a rotating disk of masers. There is strong evidence for a non-smooth morphology of the disk-torus configuration. Together with the slow temperature fall-off in radial direction, this can be seen as an indication for a clumpiness of the dust distribution.

In summary, this means that the AGN in the Circinus galaxy indeed possesses the obscuring torus long sought for. Circinus hence goes in line with NGC 1068, the brightest AGN in the MIR and the best studied Seyfert 2 galaxy. NGC 1068 was the first object where interferometric observations confirmed the presence of an extended dust distribution consistent with a torus. By consequence, these two objects are, strongly in support of the unified picture.

The MIR emission in Centaurus A, a giant elliptical radio galaxy and the nearest recent merger, is of a totally different nature. Although at the same distance as Circinus, its emission is only resolved to a minor fraction. Only a small portion of the mid-infrared flux of this source comes from an extended distribution, which is interpreted as the signature of a geometrically thin disk of warm dust. The orientation of the disk is roughly perpendicular to the jet axis. The main part of the mid-infrared emission in this source comes from an unresolved synchrotron core, most probably the foot of the jet.

It should be noted that all three objects contain an extended disk- or torus-like distribution of dust surrounding the nucleus perpendicular to the symmetry axis of the respective system. The contribution of this component to the mid-infrared flux varies significantly between the classical Seyfert galaxies, NGC 1068 and Circinus, and the radio galaxy, Centaurus A. The question, whether this implies that there is truly less dust present in the nuclei of radio galaxies, remains unanswered. Radio galaxies might have the same dust content as Seyfert galaxies, but the heating power might be insufficient to heat large amounts of dust and thus make it observable.

When taking a more detailed view, there are, however, also significant differences between the two Seyfert 2 sources. While the temperature of the dust in Circinus rises only insignificantly from the outside to the inside, namely from $T_2 = 300$ K to $T_1 = 330$ K, the temperature increase in NGC 1068 is much larger, namely from $T_2 = 320$ K to $T_1 > 800$ K according to Jaffe *et al.* (2004) or from $T_2 = 230$ K to $T_1 = 360$ K according to Poncelet *et al.* (2006). A second striking difference concerns the depth of the silicate feature. While the feature depth increases when zooming into the nucleus of NGC 1068, the inverse effect appears in the nucleus of the Circinus galaxy: its feature depth diminishes. These two (most obvious) differences indicate that there must be a significant difference in the distribution of the nuclear dust in these two galaxies.

The difference in the temperatures of the two analyses of the same data of NGC 1068 by Jaffe *et al.* (2004) and by Poncelet *et al.* (2006) highlights the large ambiguity in the models used to describe the MIDI measurements. The same problem becomes apparent when analysing the data of the Circinus galaxy: different models can describe the data similarly well. By consequence, one has to take care not to overestimate the number of properties that can be derived from the interferometric data. Currently, only first order properties, such as size and elongation of the source, presence of the silicate feature, etc., can be derived with a high certitude.

For the remaining targets, essentially only the feasibility of observations with MIDI has been tested. With the current baselines, the targets remain basically unresolved, mostly due

to their large distance. The upper size limits on the Seyfert 1 and Seyfert 2 sources do not rule out parsec-sized dusty tori. As in Centaurus A, the mid-infrared emission of 3C 273 is most likely also dominated by synchrotron emission.

It can be concluded that, although the new observations presented in this thesis in general confirm the concept of unification, there are significant differences in the details that necessitate further (interferometric) observations on the one hand and more complex unified models on the other.

Bibliography

- Antonucci, R., 1993, *ARA&A*, **31**, 473.
- Antonucci, R. R. J., and J. S. Miller, 1985, *ApJ*, **297**, 621.
- Arnaud, K. A., G. Branduardi-Raymont, J. L. Culhane, A. C. Fabian, C. Hazard, T. A. McGlynn, R. A. Shafer, A. F. Tennant, and M. J. Ward, 1985, *MNRAS*, **217**, 105.
- Arsenault, R., J. Alonso, H. Bonnet, J. Brynnel, B. Delabre, R. Donaldson, C. Dupuy, E. Fedrigo, J. Farinato, N. N. Hubin, L. Ivanescu, M. E. Kasper, *et al.*, 2003, in *Adaptive Optical System Technologies II. Edited by Wizinowich, Peter L.; Bonaccini, Domenico. Proceedings of the SPIE, Volume 4839, pp. 174-185 (2003).*, edited by P. L. Wizinowich and D. Bonaccini, pp. 174–185.
- Baade, W., and R. Minkowski, 1954, *ApJ*, **119**, 215.
- Babcock, H. W., 1953, *PASP*, **65**, 229.
- Bailey, J., W. B. Sparks, J. H. Hough, and D. J. Axon, 1986, *Nature*, **322**, 150.
- Balestra, I., S. Bianchi, and G. Matt, 2004, *A&A*, **415**, 437.
- Ballester, P., and C. Sabet, 2002, *VLT Data Interface Control Document*, Technical Report, European Southern Observatory, VLT-SPE-ESO-15000-2764, Issue 1.0.
- Balmaverde, B., A. Capetti, and P. Grandi, 2006, *A&A*, **451**, 35.
- Barvainis, R., 1987, *ApJ*, **320**, 537.
- Barvainis, R., 1993, *ApJ*, **412**, 513.
- Beletic, J. W., 2005, in *NATO ASIB Proc. 198: Optics in astrophysics*, edited by R. Foy and F. C. Foy, p. 123.
- Bolton, J. G., G. J. Stanley, and O. B. Slee, 1949, *Nature*, **164**, 101.
- Bonaccini, D., J. Farinato, M. Comin, A. Silber, C. DuPuy, R. Biasi, and M. Andrighettoni, 2000, in *Proc. SPIE Vol. 4007, p. 431-443, Adaptive Optical Systems Technology, Peter L. Wizinowich; Ed.*, edited by P. L. Wizinowich, pp. 431–443.
- Buscher, D. F., E. J. Bakker, T. A. Coleman, M. J. Creech-Eakman, C. A. Haniff, C. A. Jurgenson, D. A. Klinglesmith, III, C. B. Parameswariah, and J. S. Young, 2006, in *Unconventional Imaging II. Edited by Gamiz, Victor L.; Idell, Paul S.; Strojnik, Marija S.*, volume 6307 of *Proceedings of the SPIE*, p. 63070B.
- Chiaberge, M., A. Capetti, and A. Celotti, 2001, *MNRAS*, **324**, L33.

- Clarke, D. A., J. O. Burns, and M. L. Norman, 1992, *ApJ*, **395**, 444.
- Cohen, M., R. G. Walker, B. Carter, P. Hammersley, M. Kidger, and K. Noguchi, 1999, *AJ*, **117**, 1864.
- Colavita, M. M., and P. L. Wizinowich, 2003, in *Interferometry for Optical Astronomy II.*, edited by W. A. Traub, volume 4838 of *Proceedings of the SPIE*, pp. 79–88.
- Combes, F., 2001, in *Advanced Lectures on the Starburst-AGN*, edited by I. Aretxaga, D. Kunth, and R. Mújica, p. 223.
- Condon, J. J., G. Helou, D. B. Sanders, and B. T. Soifer, 1996, *ApJS*, **103**, 81.
- Courvoisier, T. J.-L., 1998, *A&A Rev.*, **9**, 1.
- Curran, S. J., L. E. B. Johansson, G. Rydbeck, and R. S. Booth, 1998, *A&A*, **338**, 863.
- Curran, S. J., G. Rydbeck, L. E. B. Johansson, and R. S. Booth, 1999, *A&A*, **344**, 767.
- Döbereiner, S., N. Junkes, S. J. Wagner, H. Zinnecker, R. Fosbury, G. Fabbiano, and E. J. Schreier, 1996, *ApJ*, **470**, L15.
- Draine, B. T., and H. M. Lee, 1984, *ApJ*, **285**, 89.
- Dullemond, C. P., and I. M. van Bemmell, 2005, *A&A*, **436**, 47.
- Eddington, A. S., 1925, *MNRAS*, **85**, 408.
- Elmouttie, M., R. F. Haynes, K. L. Jones, E. M. Sadler, and M. Ehle, 1998, *MNRAS*, **297**, 1202.
- Elvis, M., B. J. Wilkes, J. C. McDowell, R. F. Green, J. Bechtold, S. P. Willner, M. S. Oey, E. Polomski, and R. Cutri, 1994, *ApJS*, **95**, 1.
- European Southern Observatory, 1998, *The VLT White Book* (Garching near Munich: European Southern Observatory (ESO)).
- Evans, D. A., D. M. Worrall, M. J. Hardcastle, R. P. Kraft, and M. Birkinshaw, 2006, *ApJ*, **642**, 96.
- Fanaroff, B. L., and J. M. Riley, 1974, *MNRAS*, **167**, 31P.
- Fath, E. A., 1908, *Lick Observatory Bulletin*, **5**, 71.
- Ferrari, M., G. R. Lemaitre, S. P. Mazzanti, F. Derie, A. Huxley, J. Lemerrer, P. Lanzoni, P. Dargent, and A. Wallander, 2003, in *Interferometry for Optical Astronomy II.*, edited by W. A. Traub, volume 4838 of *Proceedings of the SPIE*, pp. 1155–1162.
- Freeman, K. C., B. Karlsson, G. Lynga, J. F. Burrell, H. van Woerden, W. M. Goss, and U. Mebold, 1977, *A&A*, **55**, 445.
- Fritz, J., A. Franceschini, and E. Hatziminaoglou, 2006, *MNRAS*, **366**, 767.
- Frogel, J. F., J. H. Elias, and M. M. Phillips, 1982, *ApJ*, **260**, 70.

- Gai, M., L. Corcione, L. Delatge, D. Gardiol, A. Gennai, M. G. Lattanzi, D. Loreggia, G. Massone, S. Menardi, and F. Reynaud, 2002, in *Beyond conventional adaptive optics: a conference devoted to the development of adaptive optics for extremely large telescopes. Proceedings of the Topical Meeting held May 7-10, 2001, Venice, Italy. Edited by E. Vernet, R. Ragazzoni, S. Esposito, and N. Hubin. Garching, Germany: European Southern Observatory, ESO Conference and Workshop Proceedings, Vol. 58, ISBN 3923524617*, edited by E. Vernet, R. Ragazzoni, S. Esposito, and N. Hubin, p. 329.
- Gai, M., S. Menardi, S. Cesare, B. Bauvir, D. Bonino, L. Corcione, M. Dimmler, G. Massone, F. Reynaud, and A. Wallander, 2004, in *New Frontiers in Stellar Interferometry, Proceedings of SPIE Volume 5491. Bellingham, WA: The International Society for Optical Engineering*, edited by W. A. Traub, p. 528.
- Gardner, F. F., and J. B. Whiteoak, 1982, *MNRAS*, **201**, 13P.
- George, I. M., and A. C. Fabian, 1991, *MNRAS*, **249**, 352.
- Gitton, P. B., S. A. Leveque, G. Avila, and T. Phan Duc, 2004, in *New Frontiers in Stellar Interferometry, Proceedings of SPIE Volume 5491. Bellingham, WA: The International Society for Optical Engineering*, edited by W. A. Traub, p. 944.
- Glindemann, A., R. Abuter, F. Carbognani, F. Delplancke, F. Derie, A. Gennai, P. B. Gitton, P. Kervella, B. Koehler, S. A. Leveque, S. Menardi, A. Michel, *et al.*, 2000, in *Proc. SPIE Vol. 4006, p. 2-12, Interferometry in Optical Astronomy*, edited by P. J. Lena and A. Quirrenbach, pp. 2–12.
- Glindemann, A., J. Algomedo, R. Amestica, P. Ballester, B. Bauvir, E. Bugueno, S. Correia, F. Delgado, F. Delplancke, F. Derie, P. Duhoux, E. di Folco, *et al.*, 2003, in *Interferometry for Optical Astronomy II.*, edited by W. A. Traub, volume 4838 of *Proceedings of the SPIE*, pp. 89–100.
- Gorjian, V., M. W. Werner, T. H. Jarrett, D. M. Cole, and M. E. Ressler, 2004, *ApJ*, **605**, 156.
- Granato, G. L., and L. Danese, 1994, *MNRAS*, **268**, 235.
- Greenhill, L. J., R. S. Booth, S. P. Ellingsen, J. R. Herrnstein, D. L. Jauncey, P. M. McCulloch, J. M. Moran, R. P. Norris, J. E. Reynolds, and A. K. Tzioumis, 2003, *ApJ*, **590**, 162.
- Hanisch, R. J., A. Farris, E. W. Greisen, W. D. Pence, B. M. Schlesinger, P. J. Teuben, R. W. Thompson, and A. Warnock, III, 2001, *A&A*, **376**, 359.
- Hao, L., H. W. W. Spoon, G. C. Sloan, J. A. Marshall, L. Armus, A. G. G. M. Tielens, B. Sargent, I. M. van Bemmell, V. Charmandaris, D. W. Weedman, and J. R. Houck, 2005, *ApJ*, **625**, L75.
- Hao, L., D. W. Weedman, H. W. W. Spoon, J. A. Marshall, N. A. Levenson, M. Elitzur, and J. R. Houck, 2007, *ApJ*, **655**, L77.
- Hardcastle, M. J., D. M. Worrall, R. P. Kraft, W. R. Forman, C. Jones, and S. S. Murray, 2003, *ApJ*, **593**, 169.

- Häring-Neumayer, N., M. Cappellari, H.-W. Rix, M. Hartung, M. A. Prieto, K. Meisenheimer, and R. Lenzen, 2006, *ApJ*, **643**, 226.
- Hawarden, T. G., G. Sandell, H. E. Matthews, P. Friberg, G. D. Watt, and P. A. Smith, 1993, *MNRAS*, **260**, 844.
- Heckman, T. M., 1980, *A&A*, **87**, 152.
- Ho, L. C., A. V. Filippenko, and W. L. W. Sargent, 1997, *ApJ*, **487**, 568.
- Hönig, S. F., T. Beckert, K. Ohnaka, and G. Weigelt, 2006, *A&A*, **452**, 459.
- Hopkins, A. M., and J. F. Beacom, 2006, *ApJ*, **651**, 142.
- Hopkins, P. F., G. T. Richards, and L. Hernquist, 2007, *ApJ*, **654**, 731.
- Horan, D., and T. C. Weekes, 2004, *New Astronomy Review*, **48**, 527.
- Hoyle, F., and W. A. Fowler, 1963, *Nature*, **197**, 533.
- Israel, F. P., 1998, *A&A Rev.*, **8**, 237.
- Jaffe, W., K. Meisenheimer, H. J. A. Röttgering, C. Leinert, A. Richichi, O. Chesneau, D. Fraix-Burnet, A. Glazeborg-Kluttig, G.-L. Granato, U. Graser, B. Heijligers, R. Köhler, *et al.*, 2004, *Nature*, **429**, 47.
- Jaffe, W. J., 2004, in *New Frontiers in Stellar Interferometry, Proceedings of SPIE Volume 5491. Bellingham, WA: The International Society for Optical Engineering*, edited by W. A. Traub, p. 715.
- Junkes, N., R. F. Haynes, J. I. Harnett, and D. L. Jauncey, 1993, *A&A*, **269**, 29.
- Karovska, M., G. Fabbiano, F. Nicastro, M. Elvis, R. P. Kraft, and S. S. Murray, 2002, *ApJ*, **577**, 114.
- Kellermann, K. I., R. Sramek, M. Schmidt, D. B. Shaffer, and R. Green, 1989, *AJ*, **98**, 1195.
- Kellermann, K. I., J. A. Zensus, and M. H. Cohen, 1997, *ApJ*, **475**, L93.
- Kemper, F., W. J. Vriend, and A. G. G. M. Tielens, 2004, *ApJ*, **609**, 826.
- Kervella, P., V. Coude du Foresto, A. Glindemann, and R. Hofmann, 2000, in *Proc. SPIE Vol. 4006, p. 31-42, Interferometry in Optical Astronomy*, edited by P. J. Lena and A. Quirrenbach, pp. 31–42.
- Kervella, P., P. B. Gitton, D. Segransan, E. di Folco, P. Y. Kern, M. Kiekebusch, T. P. Duc, A. Longinotti, V. Coude du Foresto, P. Ballester, C. Sabet, W. D. Cotton, *et al.*, 2003, in *Interferometry for Optical Astronomy II.*, edited by W. A. Traub, volume 4838 of *Proceedings of the SPIE*, pp. 858–869.
- Kessler, M. F., J. A. Steinz, M. E. Anderegg, J. Clavel, G. Drechsel, P. Estaria, J. Faelker, J. R. Riedinger, A. Robson, B. G. Taylor, and S. Ximenez de Ferran, 1996, *A&A*, **315**, L27.
- Khachikian, E. Y., and D. W. Weedman, 1974, *ApJ*, **192**, 581.

- Koehler, B., and P. Gitton, 2002, *Interface Control Document between VLTI and its Instruments*, Technical Report, VLT-ICD-ESO-15000-1826, Issue 3.0.
- Köhler, R., 2005, *Astronomische Nachrichten*, **326**, 563.
- Krolik, J. H., 1999, *Active Galactic Nuclei: From the Central Black Hole to the Galactic Environment* (Princeton: Princeton University Press).
- Krolik, J. H., and M. C. Begelman, 1988, *ApJ*, **329**, 702.
- Lagage, P. O., J. W. Pel, M. Authier, J. Belorgey, A. Claret, C. Doucet, D. Dubreuil, G. Durand, E. Elswijk, P. Girardot, H. U. Käufl, G. Kroes, *et al.*, 2004, *The Messenger*, **117**, 12.
- Lagarde, S., B. Lopez, P. Antonelli, U. Beckman, J. Behrend, Y. Bresson, O. Chesneau, M. Dugué, A. Glazenberg, U. Graser, K. H. Hofmann, W. Jaffe, *et al.*, 2006, in *Advances in Stellar Interferometry. Edited by Monnier, John D.; Schöller, Markus; Danchi, William C.*, volume 6268 of *Proceedings of the SPIE*, p. 62683M.
- Lagrange, A., G. Chauvin, T. Fusco, E. Gendron, D. Rouan, M. Hartung, F. Lacombe, D. Mouillet, G. Rousset, P. Drossart, R. Lenzen, C. Moutou, *et al.*, 2003, in *Instrument Design and Performance for Optical/Infrared Ground-based Telescopes. Edited by Iye, Masanori; Moorwood, Alan F. M., Proceedings of the SPIE, Volume 4841 (2003)*, pp. 860–868.
- Lawson, P. R., 2000a, in *Principles of Long Baseline Stellar Interferometry*, edited by P. R. Lawson, p. 113.
- Lawson, P. R. (ed.), 2000b, *Principles of Long Baseline Stellar Interferometry*.
- Lebofsky, M. J., and G. H. Rieke, 1980, *Nature*, **284**, 410.
- Leinert, C., U. Graser, F. Przygodda, L. B. F. M. Waters, G. Perrin, W. Jaffe, B. Lopez, E. J. Bakker, A. Böhm, O. Chesneau, W. D. Cotton, S. Damstra, *et al.*, 2003, *Ap&SS*, **286**, 73.
- Lena, P. J., and A. Quirrenbach (eds.), 2000, *Interferometry in Optical Astronomy*, volume 4006 of *Presented at the Society of Photo-Optical Instrumentation Engineers (SPIE) Conference*.
- Lenzen, R., M. Hartung, W. Brandner, G. Finger, N. N. Hubin, F. Lacombe, A. Lagrange, M. D. Lehnert, A. F. M. Moorwood, and D. Mouillet, 2003, in *Instrument Design and Performance for Optical/Infrared Ground-based Telescopes. Edited by Iye, Masanori; Moorwood, Alan F. M., Proceedings of the SPIE, Volume 4841 (2003)*, pp. 944–952.
- Lenzen, R., R. Hofmann, P. Bizenberger, and A. Tusche, 1998, in *Adaptive Optical System Technologies*, edited by A. M. Fowler, volume 3354 of *Proceedings of the SPIE*, pp. 606–614.
- Liang, E. P. T., 1979, *ApJ*, **231**, L111.
- Lopez, B., S. Wolf, S. Lagarde, P. Abraham, P. Antonelli, J. C. Augereau, U. Beckman, J. Behrend, N. Berruyer, Y. Bresson, O. Chesneau, J. M. Clausse, *et al.*, 2006, in *Advances in Stellar Interferometry. Edited by Monnier, John D.; Schöller, Markus; Danchi, William C.*, volume 6268 of *Proceedings of the SPIE*, p. 62680Z.

- Lord, S. D., 1992, *A New Software Tool for Computing Earth's Atmospheric Transmission of Near- and Far-Infrared Radiation*, Technical Report, NASA Technical Memorandum 103957.
- Maia, M. A. G., R. S. Machado, and C. N. A. Willmer, 2003, *AJ*, **126**, 1750.
- Maiolino, R., A. Alonso-Herrero, S. Anders, A. Quillen, M. J. Rieke, G. H. Rieke, and L. E. Tacconi-Garman, 2000, *ApJ*, **531**, 219.
- Maiolino, R., A. Krabbe, N. Thatte, and R. Genzel, 1998, *ApJ*, **493**, 650.
- Maiolino, R., A. Marconi, and E. Oliva, 2001a, *A&A*, **365**, 37.
- Maiolino, R., A. Marconi, M. Salvati, G. Risaliti, P. Severgnini, E. Oliva, F. La Franca, and L. Vanzì, 2001b, *A&A*, **365**, 28.
- Maiolino, R., and G. H. Rieke, 1995, *ApJ*, **454**, 95.
- Malkan, M. A., and W. L. W. Sargent, 1982, *ApJ*, **254**, 22.
- Marconi, A., E. J. Schreier, A. Koekemoer, A. Capetti, D. Axon, D. Macchetto, and N. Caon, 2000, *ApJ*, **528**, 276.
- Matt, G., F. Fiore, G. C. Perola, L. Piro, H. H. Fink, P. Grandi, M. Matsuoka, E. Oliva, and M. Salvati, 1996, *MNRAS*, **281**, L69.
- Mattson, B. J., and K. A. Weaver, 2004, *ApJ*, **601**, 771.
- Meier, D. L., 2002, *New Astronomy Review*, **46**, 247.
- Meier, D. L., 2004, in *AIP Conf. Proc. 714: X-ray Timing 2003: Rossi and Beyond*, edited by P. Kaaret, F. K. Lamb, and J. H. Swank, pp. 135–142.
- Meisenheimer, K., K. R. W. Tristram, W. Jaffe, D. Raban, H. Röttgering, W. D. Cotton, U. Graser, T. Henning, C. Leinert, B. Lopez, F. Israel, N. Neumayer, *et al.*, 2007, accepted for publication in *A&A*.
- Meisner, J., 2001, in *Liege International Astrophysical Colloquia*, pp. 225–231.
- Michelson, A. A., and E. W. Morley, 1887, *Philos. Mag.*, **24**, 449.
- Moorwood, A. F. M., D. Lutz, E. Oliva, A. Marconi, H. Netzer, R. Genzel, E. Sturm, and T. de Graauw, 1996, *A&A*, **315**, L109.
- Morel, S., 2007, *MIDI User Manual*, Technical Report, VLT-MAN-ESO-15820-3519, Issue 80.
- Mueller Sánchez, F., R. I. Davies, F. Eisenhauer, L. J. Tacconi, R. Genzel, and A. Sternberg, 2006, *A&A*, **454**, 481.
- Nandra, K., and K. A. Pounds, 1994, *MNRAS*, **268**, 405.
- Nenkova, M., Ž. Ivezić, and M. Elitzur, 2002, *ApJ*, **570**, L9.
- Neugebauer, G., H. J. Habing, R. van Duinen, H. H. Aumann, B. Baud, C. A. Beichman, D. A. Beintema, N. Boggess, P. E. Clegg, T. de Jong, J. P. Emerson, T. N. Gautier, *et al.*, 1984, *ApJ*, **278**, L1.

- Neugebauer, G., and K. Matthews, 1999, *AJ*, **118**, 35.
- Noethe, L., 2002, in *Progress in Optics, Volume 43*, E. Wolf, ed. (Elsevier-North-Holland, Amsterdam, 2002), pp. 1–69, ArXiv Astrophysics e-prints: astro-ph/0111136.
- Ogle, P., D. Whysong, and R. Antonucci, 2006, *ApJ*, **647**, 161.
- Oliva, E., A. Marconi, A. Cimatti, and S. D. S. Alighieri, 1998, *A&A*, **329**, L21.
- Oliva, E., A. Marconi, and A. F. M. Moorwood, 1999, *A&A*, **342**, 87.
- Oliva, E., M. Salvati, A. F. M. Moorwood, and A. Marconi, 1994, *A&A*, **288**, 457.
- Osterbrock, D. E., 1981, *ApJ*, **249**, 462.
- Osterbrock, D. E., and G. J. Ferland, 2006, *Astrophysics of gaseous nebulae and active galactic nuclei* (2nd. ed. Sausalito, CA: University Science Books, 2006).
- Packham, C., J. T. Radomski, P. F. Roche, D. K. Aitken, E. Perlman, A. Alonso-Herrero, L. Colina, and C. M. Telesco, 2005, *ApJ*, **618**, L17.
- Pauls, T. A., J. S. Young, W. D. Cotton, and J. D. Monnier, 2004, in *New Frontiers in Stellar Interferometry, Proceedings of SPIE Volume 5491*. Bellingham, WA: The International Society for Optical Engineering, edited by W. A. Traub, p. 1231.
- Pauls, T. A., J. S. Young, W. D. Cotton, and J. D. Monnier, 2005, *PASP*, **117**, 1255.
- Peterson, B. M., 1997, *An Introduction to Active Galactic Nuclei* (Cambridge University Press, Physical description: xvi, 238 p. ISBN 0521473489).
- Petrov, R. G., F. Malbet, G. Weigelt, P. Antonelli, U. Beckmann, Y. Bresson, A. Chelli, M. Dugué, G. Duvert, S. Gennari, L. Glück, P. Kern, *et al.*, 2007, *A&A*, **464**, 1.
- Pier, E. A., and J. H. Krolik, 1992, *ApJ*, **401**, 99.
- Poncellet, A., G. Perrin, and H. Sol, 2006, *A&A*, **450**, 483.
- Prieto, M. A., K. Meisenheimer, O. Marco, J. Reunanen, M. Contini, Y. Clenet, R. I. Davies, D. Gratadour, T. Henning, U. Klaas, J. Kotilainen, C. Leinert, *et al.*, 2004, *ApJ*, **614**, 135.
- Prieto, M. A., J. Reunanen, T. Beckert, K. R. W. Tristram, N. Neumayer, J. A. Fernandez-Ontiveros, and J. Acosta, 2007, ArXiv Astrophysics e-prints: astro-ph/0702160.
- Puech, F., and P. Gitton, 2006, *Interface Control Document between VLTI and its Instruments*, Technical Report, VLT-ICD-ESO-15000-1826, Issue 5.0.
- Raban, D., B. Heijligers, H. Röttgering, K. Meisenheimer, W. Jaffe, H. U. Käufel, and T. Henning, 2007, to be published in *A&A*.
- Radomski, J. T., R. K. Piña, C. Packham, C. M. Telesco, J. M. De Buizer, R. S. Fisher, and A. Robinson, 2003, *ApJ*, **587**, 117.
- Ratzka, T., 2005, *High Spatial Resolution Observations of Young Stellar Binaries*, Ph.D. thesis, Max-Planck-Institute for Astronomy, Königstuhl 17, 69117 Heidelberg, Germany.

- Ratzka, T., O. Chesneau, K. Meisenheimer, and K. Tristram, 2006, in *Advances in Stellar Interferometry*. Edited by Monnier, John D.; Schöller, Markus; Danchi, William C., volume 6268 of *Proceedings of the SPIE*, p. 62680M.
- Rees, M. J., 1984, *ARA&A*, **22**, 471.
- Rees, M. J., J. Silk, M. W. Warner, and N. C. Wickramasinghe, 1969, *Nature*, **223**, 788.
- Rejkuba, M., 2004, *A&A*, **413**, 903.
- Richards, G. T., M. A. Strauss, X. Fan, P. B. Hall, S. Jester, D. P. Schneider, D. E. Vanden Berk, C. Stoughton, S. F. Anderson, R. J. Brunner, J. Gray, J. E. Gunn, *et al.*, 2006, *AJ*, **131**, 2766.
- Rieke, G. H., 2007, *ARA&A*, **45**.
- Robson, I., 1996, *Active galactic nuclei* (Wiley-Praxis Series in Astronomy and Astrophysics, New York, NY: Wiley, Chichester: Praxis Publishing).
- Roche, P. F., D. K. Aitken, C. H. Smith, and M. J. Ward, 1991, *MNRAS*, **248**, 606.
- Roche, P. F., C. Packham, C. M. Telesco, J. T. Radomski, A. Alonso-Hererro, D. K. Aitken, L. Colina, and E. Perlman, 2006, *MNRAS*, **367**, 1689.
- Rodríguez-Ardila, A., and X. Mazzalay, 2006, *MNRAS*, **367**, L57.
- Rousset, G., F. Lacombe, P. Puget, N. N. Hubin, E. Gendron, J.-M. Conan, P. Y. Kern, P.-Y. Madec, D. Rabaud, D. Mouillet, A.-M. Lagrange, and F. J. Rigaut, 1998, in *Adaptive Optical System Technologies*, edited by D. Bonaccini and R. K. Tyson, volume 3353 of *Proceedings of the SPIE*, pp. 508–516.
- Ruiz, M., A. Efstathiou, D. M. Alexander, and J. Hough, 2001, *MNRAS*, **325**, 995.
- Salpeter, E. E., 1964, *ApJ*, **140**, 796.
- Schartmann, M., 2007, *Models of Dust and Gas Tori in Active Galactic Nuclei*, Ph.D. thesis, Max-Planck-Institute for Astronomy, Königstuhl 17, 69117 Heidelberg, Germany.
- Schartmann, M., K. Meisenheimer, M. Camenzind, S. Wolf, and T. Henning, 2005, *A&A*, **437**, 861.
- Schartmann, M., K. Meisenheimer, M. Camenzind, S. Wolf, K. R. W. Tristram, and T. Henning, 2007, to be published in *A&A*.
- Schiminovich, D., J. H. van Gorkom, J. M. van der Hulst, and S. Kasow, 1994, *ApJ*, **423**, L101.
- Schmidt, M., 1963, *Nature*, **197**, 1040.
- Schreier, E. J., A. Marconi, D. J. Axon, N. Caon, D. Macchetto, A. Capetti, J. H. Hough, S. Young, and C. Packham, 1998, *ApJ*, **499**, L143+.
- Seyfert, C. K., 1943, *ApJ*, **97**, 28.

- Shang, Z., M. S. Brotherton, R. F. Green, G. A. Kriss, J. Scott, J. K. Quijano, O. Blaes, I. Hubeny, J. Hutchings, M. E. Kaiser, A. Koratkar, W. Oegerle, *et al.*, 2005, *ApJ*, **619**, 41.
- Shankar, F., P. Salucci, G. L. Granato, G. De Zotti, and L. Danese, 2004, *MNRAS*, **354**, 1020.
- Shi, Y., G. H. Rieke, D. C. Hines, V. Gorjian, M. W. Werner, K. Cleary, F. J. Low, P. S. Smith, and J. Bouwman, 2006, *ApJ*, **653**, 127.
- Shields, G. A., 1978, *Nature*, **272**, 706.
- Siebenmorgen, R., M. Haas, E. Krügel, and B. Schulz, 2005, *A&A*, **436**, L5.
- Siebenmorgen, R., A. Moorwood, W. Freudling, and H. U. Kaeufl, 1997, *A&A*, **325**, 450.
- Sikora, M., L. Stawarz, and J.-P. Lasota, 2007, *ApJ*, **658**, 815.
- Smette, A., and L. Vanzi, 2007, *VISIR User Manual*, Technical Report, VLT-MAN-ESO-14300-3514, Issue 80.
- Smith, D. A., and A. S. Wilson, 2001, *ApJ*, **557**, 180.
- Sturm, E., M. Schweitzer, D. Lutz, A. Contursi, R. Genzel, M. D. Lehnert, L. J. Tacconi, S. Veilleux, D. S. Rupke, D.-C. Kim, A. Sternberg, D. Maoz, *et al.*, 2005, *ApJ*, **629**, L21.
- Swain, M., G. Vasisht, R. Akeson, J. Monnier, R. Millan-Gabet, E. Serabyn, M. Creech-Eakman, G. van Belle, J. Beletic, C. Beichman, A. Boden, A. Booth, *et al.*, 2003, *ApJ*, **596**, L163.
- Tingay, S. J., D. L. Jauncey, J. E. Reynolds, A. K. Tzioumis, E. A. King, R. A. Preston, D. L. Jones, D. W. Murphy, D. L. Meier, T. D. van Ommen, P. M. McCulloch, S. P. Ellingsen, *et al.*, 1998, *AJ*, **115**, 960.
- Torricelli-Ciamponi, G., P. Pietrini, and A. Orr, 2005, *A&A*, **438**, 55.
- Tozzi, P., R. Gilli, V. Mainieri, C. Norman, G. Risaliti, P. Rosati, J. Bergeron, S. Borgani, R. Giacconi, G. Hasinger, M. Nonino, A. Streblyanska, *et al.*, 2006, *A&A*, **451**, 457.
- Tran, H. D., 2001, *ApJ*, **554**, L19.
- Traub, W. A., 2000, in *Principles of Long Baseline Stellar Interferometry*, edited by P. R. Lawson, p. 31.
- Tristram, K. R. W., K. Meisenheimer, W. Jaffe, M. Schartmann, H.-W. Rix, C. Leinert, S. Morel, M. Wittkowski, H. Röttgering, G. Perrin, B. Lopez, D. Raban, *et al.*, 2007, to be published in *A&A*.
- Türler, M., M. Chernyakova, T. J.-L. Courvoisier, C. Foellmi, M. F. Aller, H. D. Aller, A. Kraus, T. P. Krichbaum, A. Lähteenmäki, A. Marscher, I. M. McHardy, P. T. O'Brien, *et al.*, 2006, *A&A*, **451**, L1.
- Turner, P. C., W. J. Forrest, J. L. Pipher, and M. A. Shure, 1992, *ApJ*, **393**, 648.
- Ueda, Y., M. Akiyama, K. Ohta, and T. Miyaji, 2003, *ApJ*, **598**, 886.

- Urry, C. M., and P. Padovani, 1995, *PASP*, **107**, 803.
- van Bemmell, I. M., and C. P. Dullemond, 2003, *A&A*, **404**, 1.
- Veilleux, S., and J. Bland-Hawthorn, 1997, *ApJ*, **479**, L105.
- Wells, D. C., E. W. Greisen, and R. H. Harten, 1981, *A&AS*, **44**, 363.
- Werner, M. W., T. L. Roellig, F. J. Low, G. H. Rieke, M. Rieke, W. F. Hoffmann, E. Young, J. R. Houck, B. Brandl, G. G. Fazio, J. L. Hora, R. D. Gehrz, *et al.*, 2004, *ApJS*, **154**, 1.
- White, R. L., D. J. Helfand, R. H. Becker, E. Glikman, and W. de Vries, 2007, *ApJ*, **654**, 99.
- Wilson, A. S., P. L. Shopbell, C. Simpson, T. Storchi-Bergmann, F. K. B. Barbosa, and M. J. Ward, 2000, *AJ*, **120**, 1325.
- Wittkowski, M., P. Kervella, R. Arsenault, F. Paresce, T. Beckert, and G. Weigelt, 2004, *A&A*, **418**, L39.
- Wizinowich, P., R. Akeson, M. Colavita, J. Gathright, E. Appleby, J. Bell, B. Berkey, A. Booth, H. Brandenburg, J. Chin, W. Dahl, C. Felizardo, *et al.*, 2006, in *Advances in Stellar Interferometry. Edited by Monnier, John D.; Schöller, Markus; Danchi, William C.*, volume 6268 of *Proceedings of the SPIE*, p. 62680N.
- Young, T., 1804, *Philos. Trans. R. Soc. London*, **94**, 1, URL: <http://links.jstor.org/sici?sici=0261-0523%281804%2994%3C1%3ATBLEAC%3E2.0.CO%3B2-G>.

Acknowledgements

I am very grateful to all the people who helped me to successfully realise this thesis. Their time, effort and support are greatly appreciated.

In particular I want to thank the following people:

Prof. Dr. Klaus Meisenheimer, for giving me the opportunity of conducting this fascinating research under his supervision, for supplying me with new impulses when necessary and for giving me advice on how to improve this thesis.

Dr. Walter Jaffe, for being so patient with me when having problems with the data reduction or when trying to understand MIDI and its data as well as for being a supportive collaborator in this project.

Prof. Dr. Immo Appenzeller for agreeing to be my co-referee.

David Raban and **Dr. Bill Cotton** for the excellent collaboration in this work on interferometric observations of nearby AGN.

Marc Schartmann, **Ingrid Rosenfelder** and my parents for reading this thesis and providing me with their suggestions for improvement.

Jeroen Bouwman, **Sebastian Hönig**, **Hendrik Linz**, **Nadine Neumayer**, **Almudena Prieto**, **Sascha Quanz**, **Thorsten Ratzka**, **Marc Schartmann** and **Roy van Boekel**, with whom I had fruitful discussions in the context of this thesis or who provided me with additional data.

Lei Hao and **James Beletic** to very quickly provide me with information, which I was hence able to include in this thesis.

Erklärung

Ich versichere, daß ich diese Arbeit selbständig verfaßt und keine anderen als die angegebenen Quellen und Hilfsmittel benutzt habe.

Declaration

I confirm, that I produced this work by my own hand and that I did not use any other resources and help except for those mentioned.

Heidelberg, 10. Juni 2007

.....
Unterschrift / Signature